A Diffraction Integral Based Turbomachinery Noise Shielding Method

ARCHIVES

MASSACHUSETTS INSTITUTE OF TECHNOLOGY

JUL 07 2011

LIBRARIES

by

Dorian Frederic Marie Colas

Diplôme de l'Ecole Centrale Paris (2011)

Submitted to the Department of Aeronautics and Astronautics
in partial fulfillment of the requirements for the degree of

Master of Science in Aeronautics and Astronautics

at the

MASSACHUSETTS INSTITUTE OF TECHNOLOGY

June 2011

© Massachusetts Institute of Technology 2011. All rights reserved.

Author .....
Department of Aeronautics and Astronautics
May 19, 2011

Certified by .....
Zoltán S. Spakovszky
H. N. Slater Associate Professor
Thesis Supervisor

Accepted by .....
Eytan H. Modiano
Associate Professor of Aeronautics and Astronautics
Chair, Graduate Program Committee

A Diffraction Integral Based Turbomachinery Noise Shielding Method

by

Dorian Frederic Marie Colas

Submitted to the Department of Aeronautics and Astronautics
on May 19, 2011, in partial fulfillment of the requirements for the degree of
Master of Science in Aeronautics and Astronautics

Abstract

A current research focus in subsonic aeronautics is the reduction of noise, emissions and fuel burn. The Silent Aircraft Initiative, NASA N+2 and N+3 projects are examples of recent efforts investigating innovative aircraft configurations to meet the future goals of air transportation. This requires novel methodologies to assess unconventional aircraft designs. This thesis is part of the N+2 program and focuses on the development of a method for the assessment of turbomachinery noise shielding in hybrid wing body aircraft.

The preliminary design and assessment of novel aircraft configurations require both low computational cost and versatility of the shielding method. High fidelity methods, such as for example boundary element methods, are computationally expensive and not amenable for optimization framework integration. On the other hand, low fidelity methods, such as the barrier shielding method, are limited in their source and geometry definitions. The diffraction integral method is a simplified ray tracing method capturing edge diffracted rays. Creeping rays and reflected rays are not accounted for making the method suitable for flat geometries with sharp edges. It is based on the Maggi-Rubinowicz formulation of the Kirchoff diffraction theory for monopole source descriptions and is inherently a high frequency method. The diffraction line integral requires numerical integration and does not account for flight effects.

A new method described in this thesis was developed to address these shortcomings. It is based on the Miyamoto and Wolf formulation of the boundary diffraction theory to allow the definition of source directivity inherent to turbomachinery noise. It is amenable to multipole and directional point source descriptions. Bulk flight effects are modelled with a generalized Prandtl-Glauert approach. Computational cost is dramatically decreased using uniform asymptotic theory to reduce the diffraction integral into a simple Fresnel integral. The Fresnel integral is solved via an analytical approximation such that the resulting shielding method does not require numerical integration. The method is applicable to three-dimensional aircraft configurations and comparison with an equivalent source method for sphere and disk shielding test cases show good agreement at high frequencies. Its analytical formulation offers compatibility with optimization frameworks facilitating new perspectives in aircraft design for noise reduction.

Thesis Supervisor: Zoltán S. Spakovszky
Title: H. N. Slater Associate Professor

Acknowledgments

First, I would like to thank my thesis supervisor Professor Spakovszky for his guidance and advice and for challenging me during my two years at MIT. Being part of the MIT N+2 team under his supervision was an honor and a privilege.

I would also like to thank everyone from the GTL. The Professors radically changed my approach to Fluid Mechanics, Engine Design and, more generally, engineering. Also, I could not have completed the project without the students and the open dialog in the lab. Special thanks to my labmate and friend Jeff Defoe for sharing his CFD expertise and Canadianness with me.

MIT would not have been the same without the French crowd and my roommates. You surely contributed to recreating a family far from home.

Thank you to my parents Stephane and Veronique Colas, my sisters Fleur and Laetitia, my brother in law Sebastien for their encouragements, support, and love. I would not have made it here without them and the strong foundation they give to my life. Thank you to my godson Mathis for his smiles and forgiving me for being away most of his first year. I promise that it will pay someday to have a godfather in the US.

Finally, a very special thank you to my love, Lizzy Atkin, for the priceless support she gave me during these years.

Contents

List of Figures

List of Tables

Nomenclature

Abbreviations

ANOPP	Aircraft NOise Prediction Program
BEM	Boundary Element Method
BDWT	Boundary-Diffracted Wave Theory
BWB	Blended-Wing-Body
CMI	Cambridge-MIT Institute
DIM	Diffraction Integral Method
ESM	Equivalent Source Method
GO	Geometrical Optics
GTD	Geometrical Theory of Diffraction
HELS	Helmholtz Equation Least Square
FAR	Federal Aviation Regulations
FSC	NASA's Fast Scattering Code for noise shielding prediction
HWB	Hybrid-Wing-Body
N2A	Hybrid-wing-body aircraft with conventional podded engines
N2B	Hybrid-wing-body aircraft with embedded propulsion system
OASPL	Overall Noise Attenuation Sound Pressure Level
PG	Prandtl-Glauert
RTM	Ray Tracing Method
SAI	Silent Aircraft Initiative
SAX	Silent Aircraft eXperimental design
SPL	Sound Pressure Level
UCI	University of California at Irvine

Roman Symbols

A	area of integration (m^2)
a	shielding sphere radius (m)
c_0	speed of sound ($m.s^{-1}$)
C_j	j-th coefficient in HELS noise description (Pa)
f	amplitude of harmonic integrand ($Pa.m^{-1}$)
g	phase function (m)
H	monopole source strength ($Pa.m$)
I_Γ	integral of acoustic pressure potential along a linear edge (Pa)
k	wavenumber (m^{-1})
L	length of contour of integration (m)
M_0	flight Mach number
p	acoustic pressure (Pa)
p_d	boundary-diffracted acoustic pressure (Pa)
p_i	incident acoustic pressure without diffraction (Pa)
p_0	amplitude of incident monochromatic acoustic pressure (Pa)
p_S	scattered acoustic pressure (Pa)
Q	directional point source strength ($Pa.m$)
$\vec{r}$	vector from observer to outline location (m)
r	magnitude of $\vec{r}$ (m)
$\vec{R}$	vector from source to obsever (m)
R	magnitude of $\vec{R}$ (m)
s	curvilinear abscissa (m)
t	detour parameter for end-points (m)
$\vec{v}$	fluid velocity ($m.s^{-1}$)
$\vec{X}$	transformed location relative to aircraft (m)
$\vec{W}$	acoustic pressure potential ($Pa.m^{-1}$)
$\vec{y_0}$	initial point of linear edge
x, y, z	coordinate system relative to aircraft: x = aft, y = starboard, z = up
x_1, y_1, z_1	transformed coordinate system relative to aircraft

Greek Symbols

θ polar angle (rad)

δ distance between point and line defined by a linear edge (m)

θ polar angle (rad)

κ transformed wavenumber (m^{-1})

$\vec{\xi}$ coordinate in transformed domain (m)

ξ detour parameter for stationary phase point (m)

λ wavelength (m)

$\vec{\rho}$ vector from source to outline location (m)

ρ magnitude of $\vec{\rho}$ (m)

ρ density $(kg.m^{-3})$

ϕ azimuthal angle (rad)

ϕ acoustic velocity potential $(m^2.s^{-1})$

ϕ_0 amplitude of acoustic velocity potential $(m^2.s^{-1})$

Φ velocity potential divided by the uniform mean flow speed (m)

ω frequency $(rad.s^{-1})$

Chapter 1

Introduction

Reducing noise around airports while decreasing fuel burn is one of the challenging goals of current research in aeronautics. In response to the growth of air transportation, NASA and other government agencies are funding research to address these challenges.

Funded by the Cambridge MIT Institute (CMI), the Silent Aircraft Initiative (SAI) investigated unconventional aircraft designs which could potentially be both fuel efficient and of low noise signature. The effort resulted in a promising Hybrid-Wing Body (HWB) aircraft configuration dubbed the SAX-40 (shown in Figure 1-2 [2]). Utilizing a large lifting planform area to shield the noise generated by the turbomachinery along with advanced operational procedures, the SAX-40 was calculated to achieve 61 dBA with a 25% reduction in fuel burn [2].

NASA's N+2 program focuses on reducing both noise and fuel burn. In this case, the NASA goals are set for the second generation of aircraft beyond the one currently in service. To address the challenges related to the growth of air transportation, they goals shown in Figure 1-1 need to be met by further aircraft design.

The N+2 project requires medium fidelity methodologies with the ability to assess the potential of innovative designs. These methods also need to be fast, in order to allow the investigation of a broad design space (see for example [2]).

CORNERS OF THE TRADE SPACE	N+1 = 2015*** Technology Benefits Relative To a Single Aisle Reference Configuration	N+2 = 2020*** Technology Benefits Relative To a Large Twin Aisle Reference Configuration	N+3 = 2025*** Technology Benefits
Noise (cum below Stage 4)	-32 dB	-42 dB	-71 dB
LTO NO_x Emissions (below CAEP 6)	-60%	-75%	better than -75%
Performance: Aircraft Fuel Burn	-33%**	-50%**	better than -70%
Performance: Field Length	-33%	-50%	exploit metro-plex* concepts

Figure 1-1: NASA goals for the next generations of aircraft [1].

Figure 1-2: SAX-40 Conceptual Aircraft Design [2].

1.1 NASA's N+2 Subsonic Fixed-Wing Project

One of the main objectives of the N+2 project is to develop methodologies for the design of quiet, fuel-efficient aircraft. These methods must be compatible with advanced and unconventional configurations.

The N+2 project is divided into two phases and the high-level tasks of the program lead by the Boeing-MIT-UCI team are briefly summarized.

Phase I

- Definition of a non-proprietary HWB aircraft configuration based on a cargo conversion of the SAX-40 to be used as a platform for assessment of methods and technologies developed during the project.
- Expension of the design for two different propulsion systems (see N2A and N2B configurations in Figure 1-3).
- Initial noise and fuel burn assessment of the aircraft.
- Planning of the aero-acoustic and aerodynamic wind tunnel test.

Phase II

- Improvement of existing prediction methods for the design and analysis of unconventional HWB aircraft that meet the N+2 goals at no computational cost increase.
- Refinement of the candidate HWB aircraft to meet the N+2 goals.
- Fabrication of the HWB aircraft model for the wind tunnel test.
- Validation of the prediction methods with aero-acoustic and aerodynamic test data.

The goal of MIT's phase II effort was to develop prediction methods to be implemented into NASA's Aircraft NOise Prediction Program (ANOPP). ANOPP assesses

Figure 1-3: Boeing N2A (top) and N2B (bottom) configurations based on the cargo version of the SAX- 40 and using podded and embedded engines respectively [picture courtesy of D. Odle, Boeing].

the different aircraft noise contributions and executes a Federal Aviation Regulation (FAR) Part 36 certification estimate (see [6]). The current methods implemented in ANOPP (see Heidmann Fan module [7] for example) are based on correlations of experimental data and are of low computational cost. A key limitation is that they are based mostly on conventional aircraft configurations. The challenge for the new methods is to be of applicable to alternative configurations at no computational cost increase.

MIT's task was to develop an alternative to ANOPP's method for turbomachinery noise shielding assessment. ANOPP currently employs the barrier shielding method derived from the work of Beranek [8] and Maekawa [9] (see description in next section).

The effort led by the University of California Irvine aimed at the development of a jet noise shielding methodology [10]. The objective was to improve on the barrier shielding by a higher fidelity method that does not require a dramatic increase in computational ressources.

1.2 Current Shielding Methods

There are four main classes of shielding assessment methods which can be used for noise shielding prediction. For integration into ANOPP, the new method should be of higher fidelity and flexibility than the Barrier Shielding Method but at no computational cost increase. These requirements and the following comparison between current methods summarized in the next sub-sections motivated the development of the Diffraction Integral Method. As seen in Table 1.1, higher fidelity methods require a dramatic increase in computational ressources.

Table 1.1: Capabilities and drawbacks of current noise shielding methods.

	Fidelity	Computation -al cost	Source directivity	Geometry	Flight effects
Ray tracing method	High	++	No	3D	Yes
BEM	High	+++	Monopoles, Dipoles	3D	Yes
ESM	High	+++	Multipoles	3D	Yes
Barrier shielding method	Low	-	No	2D	No
DIM	Medium	-	Any	3D	Yes

1.2.1 Barrier Shielding Method

Beranek [8] and Maekawa [9] developed a barrier shielding method based on empirical correlations of noise attenuation to Fresnel's number for a semi-infinite rectangular screen. The method therefore considers only straight edge diffraction from planar shielding geometries. Furthermore, it does not account for source directivity and flight effects. Although it is computationally inexpensive, the above-mentioned limitations are prohibitive for its use in turbomachinery noise shielding prediction of complex 3D configurations. Figure 1-4 illustrates the application of the barrier shielding method to a hybrid wing body aircraft.

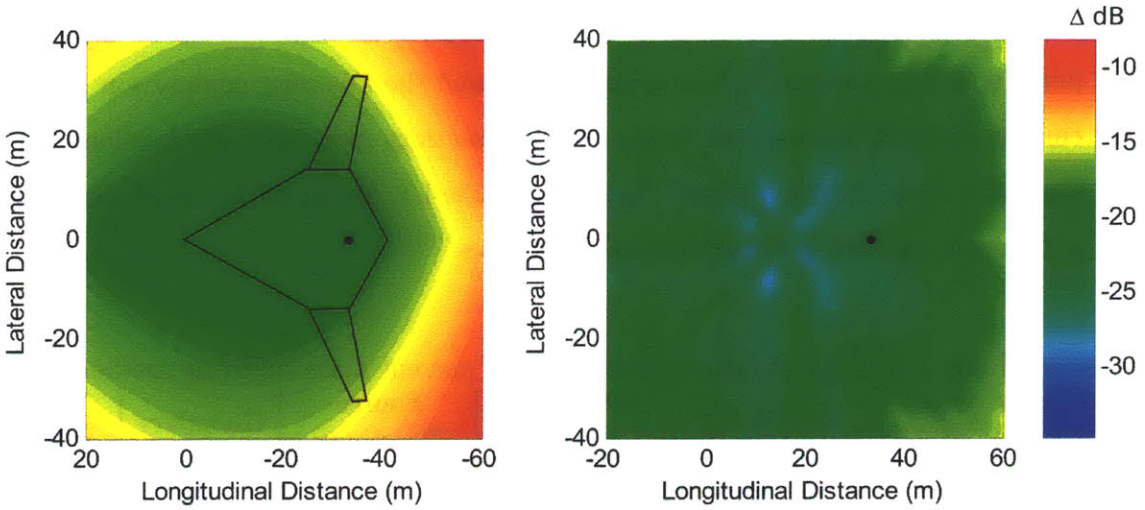

a) Barrier shielding method

b) Diffraction integral method

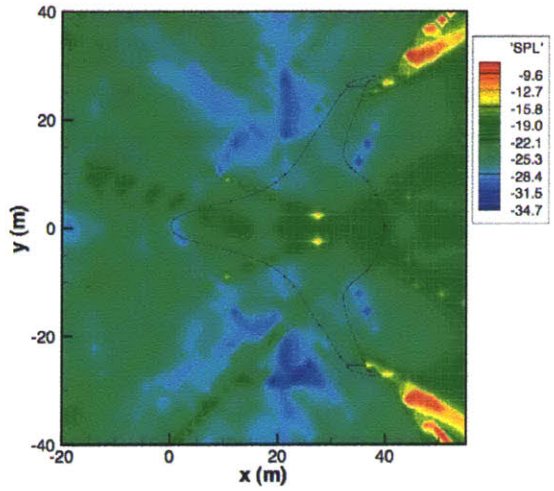

c) Ray tracing method

Figure 1-4: HWB aircraft acoustic shielding comparison between: a) barrier shielding method [3], b) diffraction integral method [3], and c) ray tracing method [4].

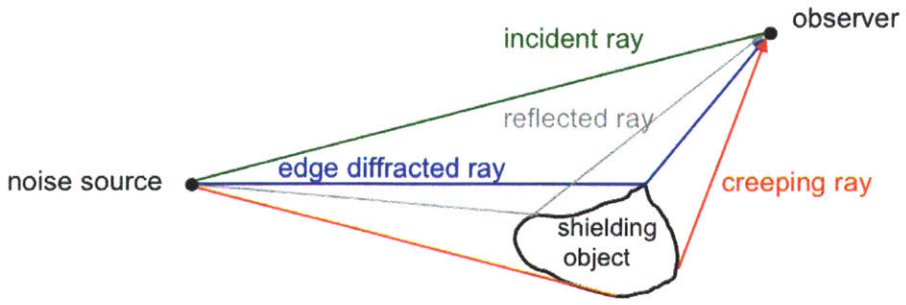

Figure 1-5: Schematic of the different rays involved in Ray Tracing Methods: Incident, reflected, edge diffracted and creeping rays.

1.2.2 Ray Tracing Methods

These methods are based on a high frequency approach. Geometrical optics is applied to compute the field due to incident and reflected rays on the shielding object. The Geometrical Theory of Diffraction provides the necessary extension to evaluate the acoustic field in the shadow regions. It introduces diffracted rays in addition to reflected and refracted rays encountered in the classical geometrical optics. There are two types of diffracted rays: edge-diffracted rays and creeping rays, as illustrated in Figure 1-5.\Ray Tracing methods are generally setup for monopole noise sources and are computationally expensive since the path of each ray needs to be evaluated with an iterative scheme. These considerations limit their use for noise shielding prediction and integration into ANOPP. But the accurate modeling of noise scattering by ray tracing methods and their compatibility with flight effects at low Mach numbers (as a first order approximation such as described in [4]) makes them amenable for noise shielding assessment in the more advanced design stages. Van Rens [11] demonstrated applicability of the ray tracing method to complicated shielding geometries such as Blended Wing Body aircraft configurations. During the Silent Aircraft Initiative, Agarwald and Dowling [4] quantified acoustic shielding effects of a Hybrid Wing Body aircraft by a ray-tracing method (see [4]) and found that the frequencies from the noise spectrum of the propulsion system were sufficiently high for ray theory to yield results that compared well with experiments.

1.2.3 Boundary Element Methods

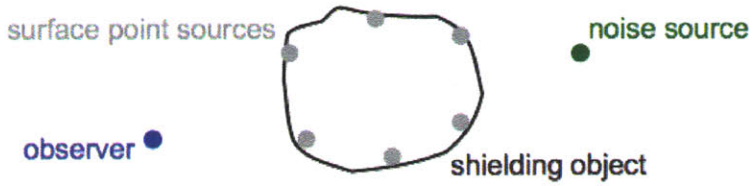

Figure 1-6: Schematic of the equivalent sources defined on the surface of the shielding object in a boundary element method [3].

In the case of noise scattering computations, boundary element method (BEM) codes are solving for an integral version of the Helmholtz equation. The solution at any point in the computational domain is represented by an integral over the outer-boundary. By representing the boundary edges as a set of panels or 'equivalent sources', as illustrated in Figure 1-6, the boundary integral equation is reduced to a linear system of equations making a numerical solution possible. Solving the linear system can become computationally expensive as the matrix size depends on the size of the shielding object and the mesh which should be fine enough to resolve the relevant source frequencies. Also, the problem reduction into a panel method is valid for monopoles or dipoles only. Because of the mentioned computational requirements, boundary element methods are likely not preferred for integration into ANOPP. Assuming the mesh size to be smaller than the wavelength, the BEM methods are more accurate than the barrier shielding and ray tracing methods, applicable to complex shielding geometries at any source frequency. As such, they have been used for acoustic shielding prediction of Blended Wing Body aircraft configurations. During the previously mentioned SAI program, Agarwald and Dowling [12] developed a BEM code accounting for flight effects using the transformation suggested by Taylor [13] and applied it for noise shielding assessment of the SAX-03 airframe. As computational cost became impractical at high frequency, the analysis was carried at a reduced frequency ka of 50, where k is the wavenumber and a is the center body chord equivalent to a full

scale frequency of 50 Hz. This low frequency noise attenuation assessment revealed a potential shielding of up to 18 dB by the considered airframe.

1.2.4 Equivalent Source Methods

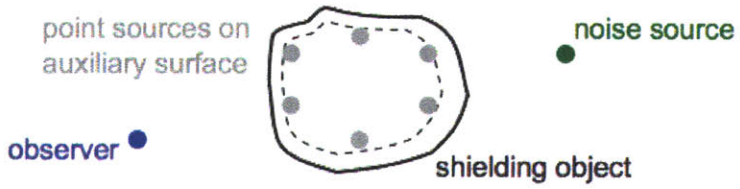

Figure 1-7: Schematic of the equivalent sources defined on the surface of the shielding object in a Equivalent Source Method [3].

Equivalent source methods are based on the same approach as boundary element methods. Both methods express the acoustic field in terms of equivalent source contributions. While in the boundary element method case the equivalent sources are located on the boundary of the shielding object and are either monopoles or dipoles, the equivalent sources are located inside the structure as illustrated in Figure 1-7. This enables the sources to be of multipole nature (monopoles, dipoles, quadrupoles, etc.). Similar to boundary element methods, solving the linear system of equations can rapidely make equivalent source methods impractical at high frequencies.

An example of the equivalent source method is NASA's Fast Scattering Code (FSC) that computes the scattered acoustic field produced by the interaction of an incident sound from a known noise source with a body of arbitrary geometry. Reimann et al. [14] validated the Fast Scattering Code on realistic shielding object shapes by carrying out numerical studies on the scattered noise field surrounding a blended wing body center nacelle and comparing the results with experimental data. Good agreement between experimental results and simulations indicated that the FSC is able to predict the acoustic behavior of the source plus center nacelle combination. Dunn and Tinetti [15][16] derived and implemented a generalized Prandtl-Glauert

transformation for NASA's Fast Scattering Code to account for flight effects. They demonstrated the code's ability by applying it to cases involving model nacelle, wing, and airframe components.

1.3 Previous Work

Most turbomachinery noise shielding assessments of advanced aicraft configurations such as HWB-type configurations have been studied using either ray tracing, boundary element method or equivalent source method codes. As shown in Table 1.1, none of these methods offers the required combination of medium fidelity, flexibility and low computational cost to be an improved alternative to the barrier shielding method. Furthermore, these methods cannot be integrated into optimization frameworks where a large number of aircraft configurations is explored.

This consideration motivated the development of a simplified ray tracing method, called the Diffraction Integral Method, to meet the objectives and goals of the N+2 program [3][17]. The original version was based on the Kirchoff theory of diffraction which is derived assuming the incident acoustic field to be unchanged on the surface of the shielding object. This approximation holds when the wavelength is much smaller than the shielding object and is therefore limited to high frequencies. Since turbomachinery noise frequencies are high, the diffraction integral method is deemed adequate to assess FAR 36 noise. In comparison to ray tracing methods, an inherent shortcoming of this approach is that its underlying theory captures only edge-diffracted rays. Also, flight effects are not accounted for.

This original version of the diffraction integral method makes use of the Maggi-Rubinowicz potential [18] to reduce the Kirchoff diffraction surface integral into a line integral along the outline of the shielding object. The outline is determined based on the source line-of-sight. Although this transformation reduces the computational cost, it also inherently constrains the source to a monopole description. The resulting line integral is then expressed in a form that can be integrated numerically using an adaptative Gauss-Kronrod quadrature method as suggested by Lummer [19]. The

method was partially validated against NASA's Fast Scattering Code for two canonical shielding geometries: a sphere and a circular disk. It was shown to perform better at high frequencies and for disk-like geometries.

To summarize, the original version of the diffraction integral method is simpler than higher fidelity methods with the inherent limitations given the involved concepts that (1) the diffraction pattern is characterized by edge-diffracted rays only, (2) the reduced frequency is assumed high, (3) the acoustic source is a monopole, (4) flight effects are not accounted for, (5) a numerical integration scheme is required.

1.4 Thesis Objectives and Goals

The underlying idea of this thesis is to use concepts from the field of optics with the goal to model noise scattering for arbitrary source descriptions at low computational cost.

More specifically, the thesis objectives are to: (1) reformulate the approach of the original version of the Diffraction Integral Method to be amenable to various source descriptions and to account for flight effects, (2) demonstrate applicability to wide range of geometries and validate the method against a high fidelity method and, (3) decrease computational cost of the diffraction integral method to be compatible with ANOPP and optimization frameworks.

1.5 Thesis overview

The next chapter reviews the theory of boundary diffracted waves and explains the key ideas and concepts behind the derivation of the diffraction integral method. Chapter 3 assesses the error due to the use of a directivity function to include directivity in the noise source description. It can be concluded that this approach should be avoided in the case of turbomachinery noise shielding assessment. Chapter 4 explains the implementation strategy of the method. The last chapter describes the validation of the diffraction integral method through comparisons with NASA's FSC and delineates

its limitations. It also illustrates the application of the method to the N2A aircraft configuration and investigates the impact of source directivity and flight effects on the noise attenuation patterns.

1.6 Contributions

A new high frequency approach for the diffraction integral method has been formulated to remedy to limitations of the original method. The enabling concepts borrowed from the geometrical theory of diffraction allow the use of source descriptions such as monopole, dipole and directional point sources. The obtained expression for the diffracted pressure field is reduced to a simple expression involving Fresnel integrals, which can be approximated analytically. Therefore, and unlike higher fidelity methods such as the boundary element method and the equivalent source method, the diffraction integral method does not require the use of a numerical integration scheme. This reduces the computational cost dramatically. The diffraction integral method accounts for flight effects using a generalized Prandtl-Glauert transformation. It is compatible with alternative aircraft configurations similar to the original method. The new method is therefore of higher flexibility and fidelity than the currently used barrier shielding method at no computational cost increase. The new method is in the process of being implemented in ANOPP.

Turbomachinery noise shielding assessment of the N2A airframe using the diffraction integral method revealed a difference in attenuation pattern of up to 12 dB between a directional point source and a monopole point source. The forward motion of the source and the N2A airframe was also shown to modify the insertion loss pattern of up to 2.5 dB compared to a static case.

Chapter 2

Theoretical Derivation of the Diffraction Integral Method

This chapter outlines the derivation of the expression for the scattered-noise around an arbitrary object at a given forward flight condition as implemented in the Diffraction Integral Method. The diffraction integral method is based on the Kirchoff diffraction theory [18] that expresses the diffracted field at any point as the superposition of waves emitted from the aperture through which the incident field is diffracted. Formally, the scattered field can be written as a surface integral on the aperture area.

Evaluating the diffraction surface integral numerically can become computationally expensive for high frequencies and large objects as the number of points required by the numerical scheme scales with the area of the object and square of the source frequency to resolve the wavelength of the sound. To reduce computational cost, the Kirchoff diffraction surface integral is transformed into a line integral, discretized and evaluated analytically under the assumptions outlined in the next-subsections.

2.1 Conceptual Summary

Turbomachinery noise frequencies are sufficiently high such that concepts from the field of optics can be applied for turbomachinery noise shielding assessment. The high frequency assumption will be tested and validated in Chapter 5 for the frequencies of

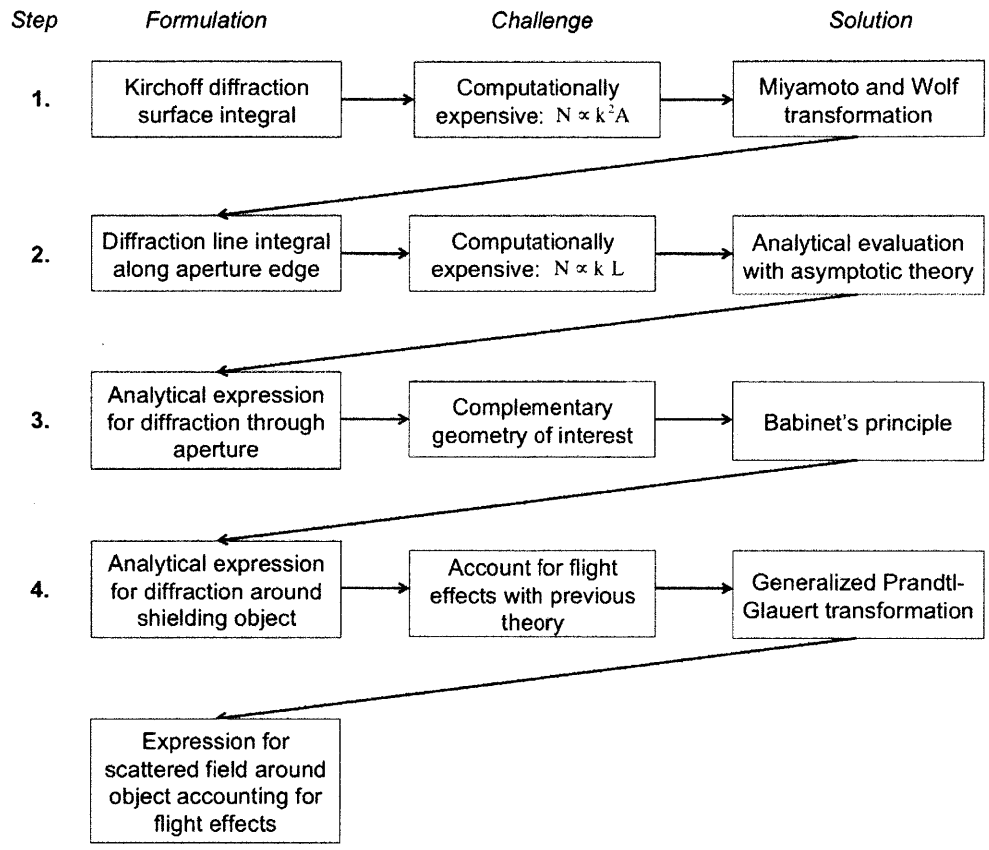

Figure 2-1: Formulations, challenges and solutions in the DIM derivation.

interest.

Key enabling concepts from the Geometrical Theory of Diffraction [20] are therefore used in the following sections to derive the desired formulation for the scattered pressure. The required steps, challenges and solutions are illustrated in Figure 2-1, where k is the wavenumber, A is the area of the shielding object are and L is the length of the edge of the object.

The noise attenuation due to shielding can then be calculated as the ratio of the total acoustic pressure to the incident acoustic pressure:

$$\Delta SPL = 20log_{10}\left|\frac{p_S}{p_i}\right| = 20log_{10}\left|\frac{p_i + p_d}{p_i}\right|, \tag{2.1}$$

where ΔSPL is the insertion loss due to shielding in ΔdB, p_S the scattered field around the object, p_i the incident field and p_d the boundary diffracted field.

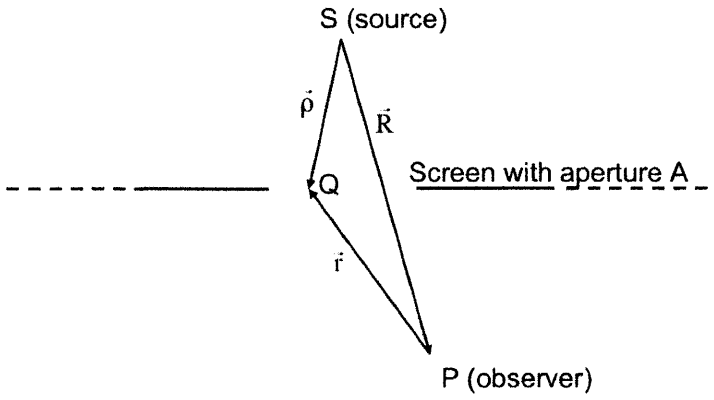

Figure 2-2: Relation between shielding geometry, source and observer locations

The overall noise attenuation can be summed over all frequency bands according to

$$OASPL = 10log_{10}\left(\frac{1}{24}\sum 10^{\frac{\Delta SPL}{10}}\right). \tag{2.2}$$

The next sections outline each of the previous steps illustrated in Figure 2-1.

2.2 Diffraction Theory

As mentionned above, the diffraction integral method is based on the Kirchoff diffraction theory and its corresponding surface integral. A possible strategy to evaluate this surface integral is to use a numerical integration scheme. However, the mesh used in the integration scheme must be fine enough to resolve the sound wavelength at their respective frequencies. Therefore the number of required points, N, scales as $N \propto k^2 A$ where k is source wavenumber and A is the area of integration. At high frequencies and for large objects, the computational cost associated with numerical integration is limiting. A transformation of the diffraction surface integral into a line integral along the outline of the shielding object is therefore used. This section outlines the first step in the conceptual summary of Fig. 2-1.

2.2.1 Kirchoff Diffraction Theory

Consider the shielding geometry illustrated in Figure 2-2: an acoustic point source S and an observer P are separated by a solid screen with an aperture A. The scalar field emitted by the source in the abscence of the screen, p_i, is known a priori.

Both the scalar fields p_S and p_i follow the Helmholtz equation outside of the surface of the screen and the source location:

$$\begin{cases} \Delta p_S + k^2 p_S = 0 \\ \Delta p_i + k^2 p_i = 0, \end{cases} \tag{2.3}$$

where k is the wavenumber.

Applying the Gauss and Green theorems on the control volume C_1 drawn in Figure 2-3, Eq.(2.3) can be re-written as

$$p_S(P) = \frac{1}{4\pi} \int\int_{\partial C_1} \left[p_S(Q)\vec{n}.\nabla \frac{e^{ikr}}{r} - \frac{e^{ikr}}{r}\vec{n}.\nabla p_S(Q) \right] dS. \tag{2.4}$$

To simplify the previous expression and to obtain an explicit expression for p_S, Kirchoff introduced the following boundary conditions on the control volume:

- $p_S = 0$ on the screen (hard boundary condition)
- $p_S = 0$ on the spherical surface enclosing the volume (far enough from the source)
- $p_S = p_i$ on the aperture.

The first condition states that the shielding object is at rest and non-oscillatory i.e will not emit noise. This is valid for solid objects with resonance frequencies different than the source frequency. The second condition states that far from the source the energy is spread out and the pressure field is zero.

The last condition is an idealization to the real field distribution by assuming that the incident field is unchanged by the screen. It is valid at high frequencies

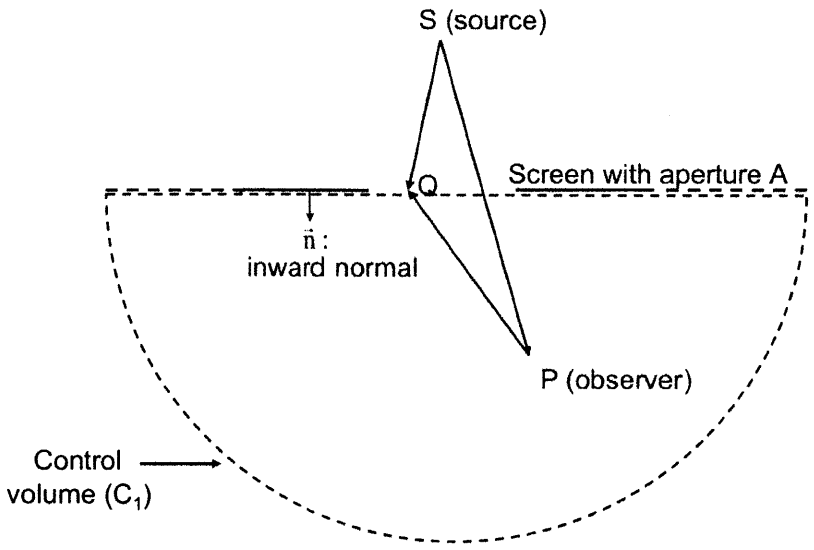

Figure 2-3: Control volume definition

for wavelengths small compared to the aperture size. These boundary conditions are summarized in Figure 2-4.

Substituting the previous boundary conditions into Eq.(2.4), only the part of the integral on the aperture remains and the Kirchoff surface integral can be deduced:

$$p_S(P) = \frac{1}{4\pi} \int\int_A \left[p_i(Q)\vec{n} \cdot \nabla \frac{e^{ikr}}{r} - \frac{e^{ikr}}{r} \vec{n} \cdot \nabla p_i(Q) \right] dS. \tag{2.5}$$

2.2.2 Theory of Boundary Diffracted Waves

To simplify the Kirchoff surface integral, the contributions of the incident geometrical optics field and that of the boundary-diffracted field are identified by the theory of boundary diffracted waves. The geometrical optics field, denoted as p_{GO}, is the undisturbed incident wave in the illuminated region, which passes through the aperture without interacting with the edge discontinuity. The remainer of the surface integral is the boundary-diffracted wave, denoted p_d, which is formed by the interaction of

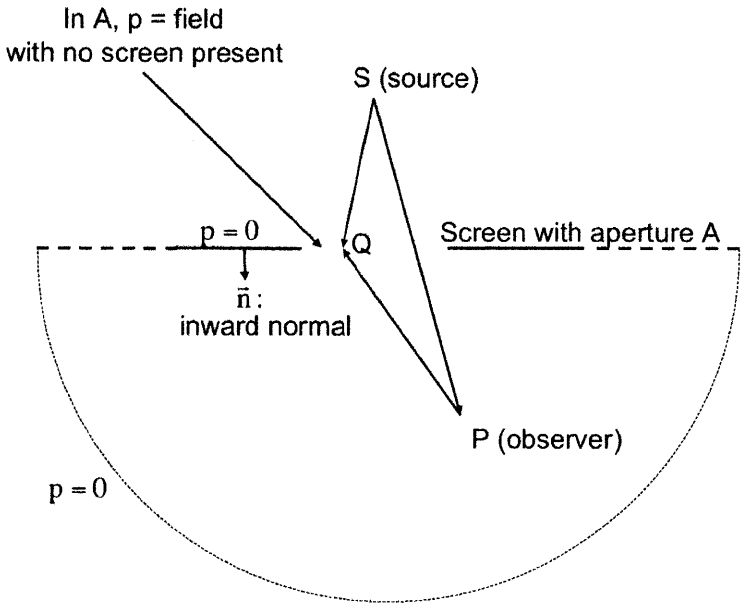

Figure 2-4: Boundary conditions corresponding to the Kirchoff diffraction theory.

the incident field with the edge. Formally, this can be written as

$$p_S(P) = p_{GO}(P) + p_d(P) \tag{2.6}$$

where $p_{GO}(P) = p_i(P)\chi(P)$ and $\chi(P)$ is the unit step function equal to one when P is inside V_1 and zero when P is inside V_2 (see Figure 2-5).

Since the BDW depends only on the outline of the shielding object, it can be expressed as a line integral as discussed in the next sub-sections.

2.2.2.1 The Maggi and Rubinowicz Potential

In the case of monopole source descriptions, Maggi and Rubinowicz [21][22] expressed the boundary diffracted wave field as follows.

Consider the control volume C_2, drawn in Figure 2-5 which is composed of the aperture A and the lateral surface of the truncated cone B, defined by rays originating from the souce and directed towards points on the edge contour of the aperture. Using

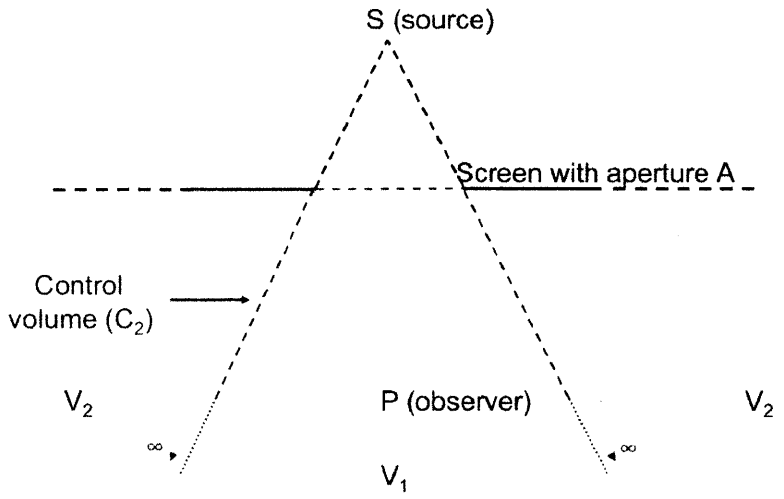

Figure 2-5: Control volume description for the Maggi and Rubinowicz formulation.

the Gauss and Green theorems on C_2 results in

$$-\frac{1}{4\pi}\int\int_{\partial C2=A+B}\left[p_i\vec{n}\cdot\nabla\frac{e^{ikr}}{r}-\frac{e^{ikr}}{r}\vec{n}\cdot\nabla p_i\right]dS=p_{GO}(P). \qquad (2.7)$$

Substituting the scattered field expression given by the Kirchoff surface integral in Eq.(2.5) in the previous expression, and using Eq.(2.6), the boundary diffracted wave is given as

$$p_d(P)=-\frac{1}{4\pi}\int\int_{B}\left[p_i\vec{n}\cdot\nabla\frac{e^{ikr}}{r}-\frac{e^{ikr}}{r}\vec{n}\cdot\nabla p_i\right]dS.$$

Assuming a monopole source description i.e $p_i(Q)=H\frac{e^{ik\rho}}{\rho}$, where H is the source strength, Maggi and Rubinowicz derived an analytical expression for the above equation. This can be written in terms of a line integral along the contour $\mathbb{C}$ of the aperture:

$$p_d(P)=\frac{H}{4\pi}\oint_{\mathbb{C}}\frac{e^{ik\rho}}{\rho}\frac{e^{ikr}}{r}\frac{(\vec{\rho}\times\vec{r})\cdot d\vec{s}}{\rho r+\vec{\rho}\cdot\vec{r}}. \qquad (2.8)$$

2.2.2.2 The Miyamoto and Wolf Potential

Extending the work of Maggi and Rubinowicz by making use of vector algebra, Miyamoto and Wolf [23][24] showed that the expression in Eq.(2.8) is also exact

for oblique plane waves. Further, they showed that if the incident wave is neither plane nor spherical, the same potential holds as the leading term of an asymptotic expansion involving inverse powers in k and becomes

$$p_d(P) \simeq \frac{1}{4\pi} \oint_{\mathbb{C}} p_i(\rho) \frac{e^{ikr}}{r} \frac{(\vec{\rho} \times \vec{r}) \cdot d\vec{s}}{\rho r + \vec{\rho} \cdot \vec{r}}. \tag{2.9}$$

In the following developments, the diffraction potential will be denoted $\vec{W}$ and the previous expression can be written simply as

$$p_d(P) = \oint_{\mathbb{C}} \vec{W} \cdot d\vec{s}. \tag{2.10}$$

2.2.2.3 Singularity in the Diffraction Potential

The line integral is an exact form as derived by a rigorous integration of the surface integral along the shadow boundary. It is non-uniform since the integrand approaches infinity in the so-called transition region where $\rho r + \vec{\rho} \cdot \vec{r} = 0$. This region, where the potential diverges, corresponds to observer locations where χ transitions from 1 to 0. As a consequence of the discontinuity of the geometrical optic field in this region, the integrand becomes singular to compensate for this discontinuity and to ensure continuity of the overall scattered field.

This non-physical singularity is a limitation of the boundary diffracted wave theory [25][22]. Lummer [19] introduced a means to subtract it from the computational domain and gave an explicit form for its contribution to the scattered field. However, the expression he developed holds only for the Maggi and Rubinowicz formulation, i.e. in the case of a monopole source description. It will be avoided using the Uniform Theory of Diffraction as illustrated in the next sections.

2.3 Discretization of the Integration Contour

To obtain an explicit expression for the diffraction line integral (Eq.(2.9)), the contour of integration is discretized into linear edges $\{\Gamma_i\}_i$. Thus the problem is reduced to

finding an exact expression for the same line integral, but on a linear edge. The next sections outline the derivation of such an expression. Knowing this expression, the diffracted field can then be computed by superimposing the contribution of each linear edge according to

$$p_d(P) = \oint_{\mathbb{C}} \vec{W} \cdot d\vec{s} \simeq \sum_i \int_{\Gamma_i} \vec{W} \cdot d\vec{s}. \tag{2.11}$$

In practice, the level of discretization is decreased until no differences are observed in the obtained noise attenuation patterns.

2.4 Uniform Asymptotic Expansion of the Line Integral

Although computational cost has been decreased by reducing the Kirchoff diffraction surface integral (Eq.(2.5)) into a line integral as in Eq.(2.9), the number of points required to evaluate the scattered pressure scales with kL with L the length of the contour of integration. Again, computational cost associated with numerical integration can become prohibitive for high frequencies and large objects. In the case of monochromatic waves, asymptotic theory offers a simple way to express Eq.(2.9) analytically on a linear edge and to avoid the use of a numerical integration scheme. However, it introduces spurious singularities as a result of the loss of information. The Uniform Theory of Diffraction [26] is used to avoid these singularities by re-expressing the expansions in terms of Fresnel integrals, which are continuous distributions.

2.4.1 Monochromatic Source Description

The case of a compact, monochromatic wave is considered throughout the following derivations. It can be written as

$$p_i(\vec{\rho}) = p_0(\vec{\rho}) e^{ik|\vec{\rho}|} \tag{2.12}$$

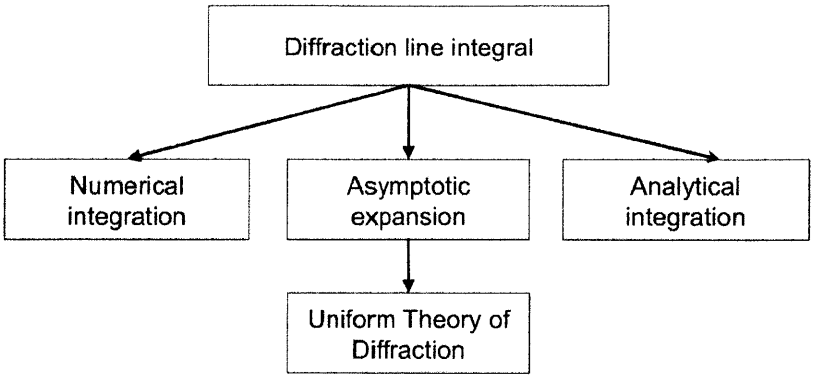

Figure 2-6: Strategies to evaluate the diffraction line integral.

where $p_0(\vec{\rho})$ is the wave amplitude.

$p_0(\vec{\rho})$ can describe any arbitrary compact and monochromatic wave such that $p_i(\vec{\rho})$ satisfies the Helmholtz equation (see Eq.(2.3)).

2.4.2 Line Integral Formulation for the Application of Asymptotic Theory

Consider an arbitrary linear segment Γ characterized by a unit vector $\vec{e}$, an initial point $\vec{y_0}$ and start and end points denoted by their curvilinear abscissae s_a and s_b. Making use of the compact source description (Eq.(2.12)), the diffraction line integral along Γ, I_Γ, can be re-written as a Fourier integral

$$I_\Gamma = \int_\Gamma \vec{W} \cdot d\vec{s} = \frac{1}{4\pi} \int_\Gamma p_0(\vec{\rho}) \frac{1}{r} \frac{(\vec{\rho} \times \vec{r}) \cdot d\vec{s}}{\rho r + \vec{\rho} \cdot \vec{r}} e^{ik(r+\rho)} = \int_\Gamma f(s) e^{ikg(s)} ds, \qquad (2.13)$$

where f and g are the amplitude and phase functions of the integral respectively.

The harmonic nature of I_Γ and its singularity in the transition region renders numerical integration inaccurate and computationaly expensive since it requires adaptive integration schemes. In simple cases analytical solutions can be derived (see for example [27]). An alternative way of evaluating I_Γ is offered by the asymptotic expansions theory and the method of stationary phase [28]. These strategies are investigated here. Figure 2-6 illustrates the possible solution paths.

2.4.3 Asymptotic Expansions and Method of Stationary Phase

If the phase function g does not have any stationary phase points inside Γ (i.e $\forall s \in \Gamma$, $g'(s) \neq 0$), the asymptotic expansion of integral in Eq.(2.13) can be obtained via integration by parts:

$$I_\Gamma = \int_{s_a}^{s_b} f(s) e^{ikg(s)} ds = \frac{1}{ik} \left[\frac{f(s_b)}{g'(s_b)} e^{ikg(s_b)} - \frac{f(s_a)}{g'(s_a)} e^{ikg(s_a)} \right] + \mathcal{O}(k^{-1}). \tag{2.14}$$

In this case, the integral is governed by its end points contributions. For a monochromatic wave, the phase function is $g(s) = r(s) + \rho(s)$ and the linear segment has a stationary phase point if there exists a point where the total distance $r + \rho$ is minimal.

On the contrary, if g has one stationary phase point of order 2 lying on Γ at the abscissa s^* such that $g'(s^*) = 0$ and $g''(s^*) \neq 0$ then the evaluation of the integral is governed by its stationary phase point contribution. The method of stationary phase [28] gives an explicit expression according to

$$I_\Gamma = \frac{e^{i\frac{\pi}{4}}}{2} f(s^*) \sqrt{\frac{\pi}{k g''(s^*)}} e^{ikg(s^*)} + \mathcal{O}(k^{-1/2}). \tag{2.15}$$

Depending on the stationary phase point location, either Eq.(2.14) or Eq.(2.15) is taken into account. A drawback of this approach is the introduction of a singularity in the contribution of the end-points. When the stationary phase point coincides with one of the end-points, the inverse of the phase function diverges to infinity. Therefore, the Uniform Theory of Diffraction is considered in the next section to change the topology of the integral and avoid these spurious singularities.

2.4.4 Uniform Theory of Diffraction

In addition to the singularity due to the asymptotic expansion, the amplitude function f still contains the original singularity of the potential $\vec{W}$. This reflects the loss of information between the asymptotic expansion and the original line integral as the singularity should be integrated and replaced by a discontinuity. This discontinuity would then compensate for the discontinuity of the geometrical optic field and the

total scattered field would be continuous everywhere.

The Uniform Theory of Diffraction [26] postulates that the scattered field behaves like a Fresnel integral in the transition region. The uniform theory of diffraction is motivated by the exact solution derived by Sommerfeld to the canonical problem of plane wave diffraction by a half plane [29]. After introducing the so-called 'detour' parameter as a change of variable, Sommerfeld uses the fundamental property of the Fresnel integral to describe the diffracted field that is given by

$$F[x] = U(-x) + sign(x)F[|x|], \tag{2.16}$$

where $U(x)$ is the unit step function and

$$F[x] = \frac{e^{-i\frac{\pi}{4}}}{\sqrt{\pi}} \int_x^\infty e^{it^2} dt. \tag{2.17}$$

In the Sommerfeld solution, the first term of the right-hand side of Eq.(2.16) represents the geometrical optics field and the second term represents the singularity-free boundary diffracted waves.

2.4.5 Uniform Asymptotic Expansion of the Diffraction Line Integral

2.4.5.1 Uniform Contribution of the End-Points

To avoid the spurious singularity introduced in the end-points contributions, Umul [30] introduced a change of variable similar to the one used in the Sommerfeld solution. A variation of this singularity-free expression for the end-point contributions is derived in Appendix A [30]. It involves Fresnel integrals accordingly to the uniform theory of diffraction and is given as

$$\int_{s_a}^\infty f(s)e^{ikg(s)}ds = \sqrt{\pi}e^{i\frac{\pi}{4}}e^{ikg(s^*)}\left\{G(s^*)U(-t(s_a)) + G(s_a)sign(t(s_a))F[|t(s_a)|]\right\} \tag{2.18}$$

where the detour parameter is defined as $t(s) = \epsilon_t(s)\sqrt{k\,|g(s^*) - g(s)|}$ with the shadow indicator $\epsilon_t(s) = \pm 1$ if $(s^* - s) \gtrless 0$ and the phase function $g(s) = r(s) + \rho(s)$. Furthermore, $G(s) = \frac{f(s)}{h(s)}$ and $h(s) = \begin{cases} k\frac{g'(s)}{2t(s)} & if\ s \neq s^* \\ \sqrt{\frac{kg''(s^*)}{2}} & if\ s = s^* \end{cases}$. $U(x)$ is the unit step function.

Making use of Eq.(2.18), the line integral along Γ can be re-written as

$$\begin{aligned} I_\Gamma &= \int_{s_a}^{s_b} f(s)e^{ikg(s)}ds \\ &= \int_{s_a}^{\infty} f(s)e^{ikg(s)}ds - \int_{s_b}^{\infty} f(s)e^{ikg(s)}ds \\ &= \sqrt{\pi}e^{i\frac{\pi}{4}}e^{ikg(s^*)}\left\{G(s^*)\left(U(-t(s_a)) - U(-t(s_b))\right) + \right. \\ &\quad \left. G(s_a)sign(t(s_a))F[|t(s_a)|] - G(s_b)sign(t(s_b))F[|t(s_b)|]\right\}. \end{aligned} \tag{2.19}$$

The first group of terms is the stationary phase point contribution and the last two terms are the end point contributions. The term $U(-t(s_a)) - U(-t(s_b))$ is unity when the stationary phase point is in Γ and otherwise it is zero.

An important case is when s^* is equal to an end-point abscissa. The first group of terms in Eq.(2.19) is then zero as well as the detour parameter. $G(s^*)$ is a finite number and the value of the Fresnel integral becomes

$$F[0] = 1/2. \tag{2.20}$$

This illustrates that the stationary phase point contributes to the integral by half of its maximal contribution since in that case the integration is carried out only on either the right or the left-hand side. Also, this corroborates the continuous distribution of the expression in Eq.(2.19) for all values of s^*.

2.4.5.2 Uniform Contribution of Boundary Diffracted Waves

At this stage I_Γ still contains the singularity of the potential in the transition region. The strategy here is to apply the Uniform Theory of Diffraction to change the

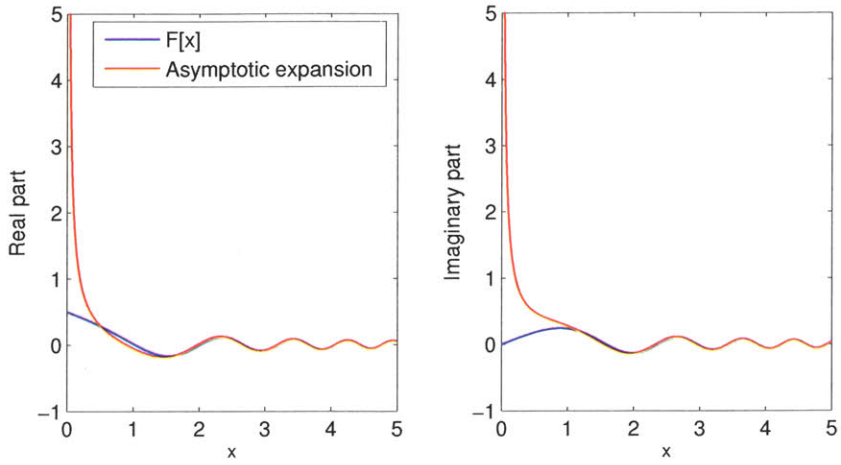

Figure 2-7: Evaluation of the Fresnel integral $F[x]$ and its asymptotic expansion.

topology of the integrand to avoid this non-physical singularity. In order to do so, the asymptotic development of a Fresnel integral in the function f is isolated and replaced by the actual integral defined in Eq.(2.17).

This expansion is given as

$$sign(x)F[|x|] \simeq \frac{e^{i\frac{\pi}{4}}}{2\sqrt{\pi}}\frac{e^{ix^2}}{x}. \tag{2.21}$$

The difference between the function and its asymptotic expansion is that the expansion has a singularity at $x = 0$, but the function is continuous everywhere. This behavior is illustrated in Figure 2-7.

Another detour parameter as a change of variable is introduced as

$$\xi(s, P) = \epsilon_\xi(P)\sqrt{k\,[g(s) - R]}. \tag{2.22}$$

It is similar to the one introduced by Sommerfeld in his exact solution of the canonical problem of plane waves diffraction by a half plane.

The uniform theory of diffraction is applied to Eq.(2.19) by substituting its oscillatory part successively by the above detour parameter. The asymptotic expansion

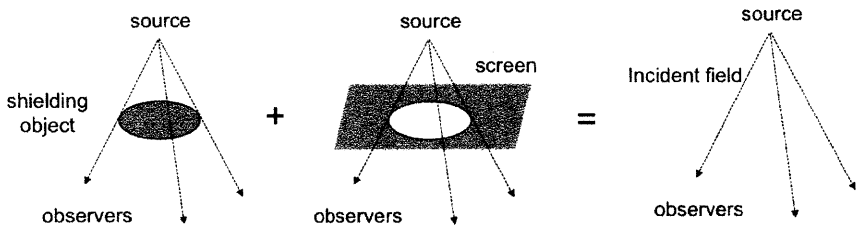

Figure 2-8: Illustration of Babinet's principle.

of a Fresnel integral is then recognized as follows:

$$\begin{aligned} e^{ikg(s^*)} &= e^{i\xi^2} e^{jkR} \\ &\simeq 2\sqrt{\pi}\xi e^{-i\frac{\pi}{4}} e^{ikR} sign(\xi) F[|\xi|], \end{aligned} \tag{2.23}$$

where $\epsilon_\xi(P)$ is a shadow indicator and is equal to 1 if P is located in the illuminated region and -1 otherwise. The uniform asymptotic expansion of the diffraction line integral becomes

$$\begin{aligned} I_\Gamma &= 2\pi e^{ikR} \xi sign(\xi) F[|\xi|] \{G(s_s)[U(-\xi_a) - U(-\xi_b)] \\ &\quad + G(s_a) sign(\xi_a) F[|\xi_a|] - G(s_b) sign(\xi_b) F[|\xi_b|]\} . \end{aligned} \tag{2.24}$$

The expression given in Eq.(2.24) is singularity-free because the pole of the amplitude function is compensated by the zero of the detour parameter ξ when $\vec{\rho} - \vec{r} = \vec{R}$.

At this step of the derivation, the diffracted field through an arbitrary aperture can be evaluated by discretizing the edge of the aperture edge into linear edges and by superimposing their exact and analytical contributions according to Eq.(2.24).

2.5 Babinet's Principle

The previous expressions correspond to the the diffraction through a screen with an arbitrary aperture. However, the geometry of interest is the scattering around the complementary arbitrary object. This section outlines step 3 of the conceptual summary in Figure 2-1.

Babinet's principle states that the boundary diffracted wave due to an aperture is the same in amplitude but opposite in phase relative to the complementary object. As a result, when adding the diffraction patterns associated with these two configurations, the sum of the respective geometrical optics fields will be equal to p_i and the boundary diffracted waves cancel each other.

This principle can be used to yield a simple relationship between the scattered fields corresponding to the two shielding geometries that is illustrated in Figure 2-8 and is given as

$$p_S^{shielding\ object} = p_i - p_S^{complementary\ screen}. \tag{2.25}$$

2.6 Flight Effects

2.6.1 Introduction

The previous derivation of the expression of the scattered field assumed no external flow. However, the interaction between a flow and the sound field produced by acoustic sources and sound-scattering bodies is of great interest to predict aircraft noise. The main challenge is to capture this interaction using noise shielding prediction methods that have been derived assuming no flow. The idea is to modify the time and space variables to account for the translation of the source and the shielding body.

Transformations such as suggested by Taylor [13] and by Tinetti and Dunn [15][16] have been derived to capture the above-mentionned interaction. The two transformations are valid under the assumptions of isentropic, inviscid and irrotational low Mach number flows.

A quantitative assessment of the two transformations is given in this section to delineate their limitations and applicability.

Even though non-uniform potential flow fields could be treated with the two approaches (see [16] and [31] for a numerical comparison of the results obtained with the two formulations), only the case of a uniform background velocity field directed

along $\vec{e_x}$ is considered to capture the bulk effects of the motion of the noise source and shielding object.

2.6.2 Taylor Transformation

The first transformation has been suggested by Taylor [13] . The key idea is to convect both the source and the diffracting object at the external flow velocity. This linear transformation is given as

$$(X, Y, Z, T) = (x, y, z, t + M_0 \frac{\hat{\Phi}}{c_0}). \tag{2.26}$$

where capital letters are used for transformed variables, $\hat{\Phi}$ and M_0 are respectively the background flow velocity potential divided by the speed of the uniform stream far from the aircraft and its corresponding Mach number. Since this transformation is linear, it does not modify the source frequency. This is of great interest when the source description is based on measurements and not known at all frequencies.

Neglecting higher-order Mach number terms, the equation which governs the acoustics is the convected wave equation written for the acoustic potential as

$$\frac{1}{c_0^2}\frac{\partial^2 \phi}{\partial t^2} + \frac{2M}{c_0}\nabla\hat{\Phi}.\nabla\frac{\partial \phi}{\partial t} - \nabla^2\phi = 0, \tag{2.27}$$

where ϕ is the acoustic velocity potential and c_0 is the speed of sound. Here, $\hat{\Phi} = x$ and $\vec{\nabla}\hat{\Phi} = \vec{e_x}$.

The suggested transformation reduces Eq.(2.27) to the original case without background flow [13].

The case of a monochromatic acoustic wave of wavelength k is considered. It can be shown that the acoustic pressure in the case with background flow can be related to the acoustic pressure in the satic case by

$$p_{M_0>0} = \left[p_{M_0=0} + i\frac{M_0 c_0}{\omega}\frac{\partial p_{M_0=0}}{\partial x}\right] e^{-i\frac{M_0\omega}{c_0}x} + \mathcal{O}_0(M_0). \tag{2.28}$$

The detailed derivation of Eq.(2.28) is given in Appendix B. $p_{M_0=0}$ is obtained after

solving the classical Helmholtz equation with the original wavelength k.

It can be noted that the expression in Eq.(2.28) requires the evaluation of the first derivative of the acoustic pressure. Its implementation is outlined in Chapter 4.

2.6.3 Generalized Prandtl-Glauert Approach

The second transformation has been suggested by Tinetti and Dunn [15][16]. It is based on a non-linear transformation similar to the Prandtl-Glauert approach. Due to its non-linearity, this transformation requires the scattering computation to be carried out at the Doppler shifted frequencies. This limitation can become limiting in the case where the source description is based on measurements that were not performed at the shifted frequencies of interest.

It is valid under the assumption of small perturbations of the flow variables and for harmonic waves of frequency ω. The acoustic perturbations can be introduced as follows

$$\begin{cases} \rho = & \rho_0 + \rho' e^{i\omega t} \\ p = & p_0 + p' e^{i\omega t} \\ \vec{v} = & \vec{v_0} + \vec{v'} e^{i\omega t} \end{cases} . \tag{2.29}$$

Introducing the above acoustic perturbations into the governing equation conservating mass, momentum and energy, it can be shown ([15][16]) that the acoustic pressure and velocity fields satisfy

$$\begin{cases} ikp' + \rho_0 c_0 \nabla \cdot (\frac{p'}{\rho_0 c_0} \vec{M_0} + \vec{v'}) & = 0 \\ ik\vec{v'} + \frac{1}{\rho_0 c_0} \nabla (p' + \rho_0 c_0 \vec{M_0} \cdot \vec{v'}) & = 0 \end{cases} . \tag{2.30}$$

To decouple the acoustic propagation from the convection due to mean flow, Tinetti and Dunn [15][16] introduced a Lorentzian tranformation and defined new indepen-

dent variables $\vec{\xi}$

$$\vec{\xi} = \begin{pmatrix} x_1 \\ y_1 \\ z_1 \end{pmatrix} = B_0^{-1}\vec{x}, \tag{2.31}$$

which leads to a new set of dependent variables

$$\begin{cases} p_1' &= \frac{1}{\beta_0}\left(p' + \rho_0 c_0 \vec{M}_0 \cdot \vec{v'}\right) e^{-i\kappa \vec{M}_0 \cdot \vec{\xi}} \\ \vec{v_1'} &= B_0^{-1}\left(\vec{v'} + \frac{p'}{\rho_0 c_0}\vec{M}_0 \vec{M}_0{}^{\top}\right) \end{cases}. \tag{2.32}$$

The matrix of the Lorrentzian transformation is defined as $B_0 = I - \frac{1-\beta_0}{M_0^2}\vec{M}_0\vec{M}_0{}^{\top}$ with its inverse $B_0^{-1} = I + \frac{1-\beta_0}{\beta_0 M_0^2}\vec{M}_0\vec{M}_0{}^{\top}$ where $\beta_0 = \sqrt{1-M_0^2}$ is the the forward velocity correction and the wavenumber is $\kappa = \frac{k}{\beta_0}$.

After manipulations (for details see [15][16]), the modified acoustic pressure p_1' can be shown to satisfy the classical Helmholtz equation without background flow

$$\nabla^2 p_1' + \kappa^2 p_1' = 0.$$

Transforming the equations back to the domain with background flow, the pressure p_1' and p' are related to one another by

$$p'(\vec{\xi}) = \frac{1}{\beta_0}(p_1'(\vec{\xi}) + i\frac{M_0}{\kappa}\frac{\partial}{\partial x_1}p_1'(\vec{\xi}))e^{-i\kappa \vec{M}_0 \cdot \vec{\xi}}. \tag{2.33}$$

The knowledge of the first derivative along the axial coordinate of the acoustic pressure is required. The implementation of this derivative is outlined in Chapter 4.

2.6.4 Comparison Between the Taylor Transformation and the Generalized Prandtl-Glauert Approach

To assess the applicability and limitations of the two different approaches, the case of an acoustic omni-directional point source is considered. In this case the scattered fields using both transformations can be expressed explicitly.

For a wavelength λ of 0.1 unit length, a source strength of unity and a mean flow Mach number of 0.3, the results obtained with the two approaches are illustrated in Figure 2-9 where contours of the real part of the pressure are plotted. A 6 dB difference is observed between the results at the same upstream distance of the source of 0.5 unit length. This discrepancy can be explained as follows.

The Taylor method can be shown to be equivalent to the first order term of the Taylor expansion of the Prandtl-Glauert approach. The details are given in Appendix B.

More specifically for an observer located at a distance r upstream of the source in the direction of the mean flow, the discrepancy scales with

$$\frac{p^{PG}_{M_0>0} - p^{Taylor}_{M_0>0}}{p^{Taylor}_{M_0>0}} \sim ikrM_0^2 \tag{2.34}$$

for $M_0 \to 0$.

Figure 2-10 illustrates the relation in Eq.(2.34). This relation shows that the Taylor method is the leading term of the asymptotic expansion relative to the free stream Mach number of the generalized Prandtl-Glauert approach. For a given reduced frequency kr (for example $kr = 500$ with a typical turbomachinery noise frequency $f = 1000$ Hz and $r = 30$ m for an observer on the shielding planform), both transformations will yield the same result at low Mach numbers ($M_0 < 0.01$) since the extra terms in the expansion are small compared to the leading term. But the error of the Taylor transformation increases with the Mach number since these higher order terms become dominant. This behavior is amplified as the reduced frequency kr is increased since the relative difference in Eq.(2.34) also scales linearly with kr.

In the case of turbomachinery shielding during approach condition, the flight Mach number is approximately 0.2 (see [32]). The relative error of the Taylor transformation at this speed and for a reduced frequency of 500 is higher than 100% i.e the pressures are of opposite phases. This last consideration reveals that the Taylor transformation is limited to lower Mach numbers ($M_0 < 0.01$) than the approach condition value. The generalized Prandtl-Glauert transformation was therefore selected and implemented

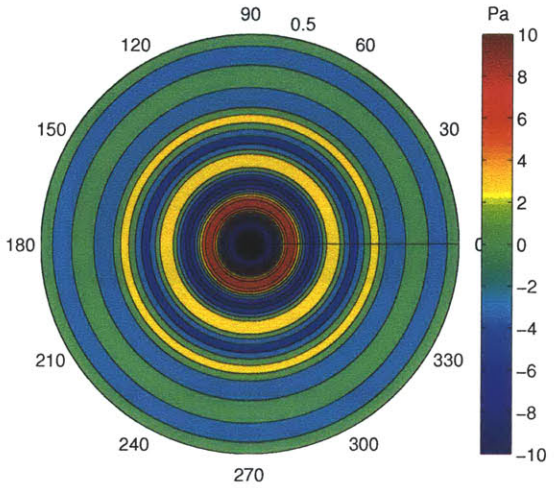

a) Without background flow

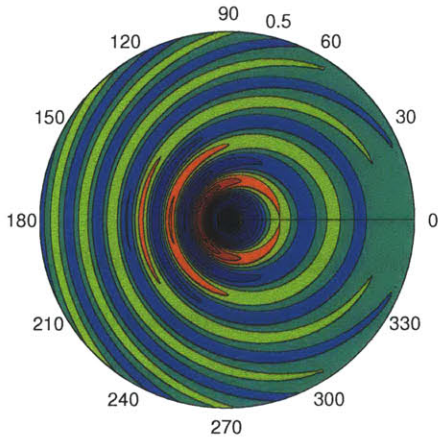

b) Taylor Transformation

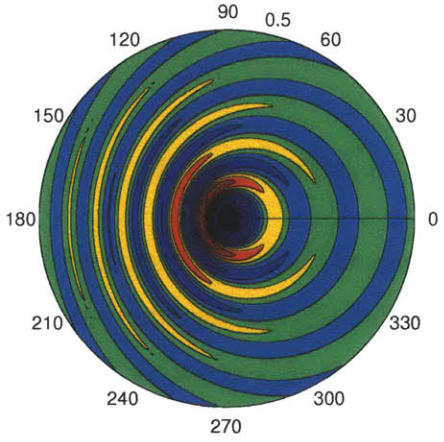

c) Generalized Prandtl-Glauert approach

Figure 2-9: Illustration of the two transformations: real part of the pressure radiated by a monopole acoustic source in a uniform background flow (M = 0 and M =0.3). a) without flight effects, b) Taylor transformation and c) Generalized Prandtl-Glauert approach.

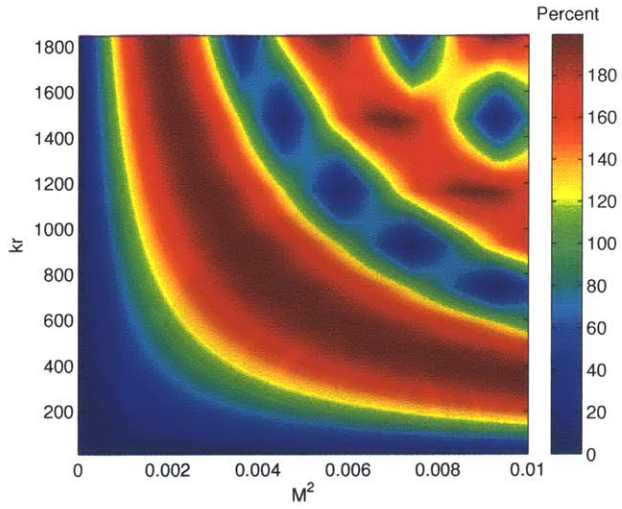

Figure 2-10: Relative difference between the Taylor transformation and the generalized Prandtl-Glauer approach in the case of a monopole source in a uniform background flow for various Mach numbers square M_0^2 and reduced frequencies kr.

in the Diffraction Integral Method since approach conditions are part of a FAR 36 assessment [6].

2.7 Conclusion

To summarize, a high frequency methodology based on the Geometrical Theory of Diffraction [20] has been derived. The range of admissible frequencies will be assessed in Chapter 5 by comparing the diffraction integral method with NASA's Fast Scattering Code. The new method assumes that the shielding object is flat with sharp edges and the reduced frequency high enough such that the incident acoustic field can be approximated to be unchanged on the surface of the shielding object. These limitations will also be assessed in Chapter 5.

The evaluation of the scattered field around an arbitrary object is given by a sum of analytical terms instead of the initial Kirchoff diffraction surface integral. The diffraction integral method accounts for bulk flight effects using the generalized Prandtl-Glauert transformation which has been shown to be compatible with Mach numbers corresponding to approach conditions. It only requires the incident acoustic

source, the source line-of-sight of the shielding object and the flight conditions to estimate the diffracted field at any observer location.

Chapter 3

Turbomachinery Noise Description

Current methods to predict shielding of aircraft configuration assume monopole source descriptions. However, turbomachinery noise is directional thus requiring a different approach for the noise scattering method and a different noise description to account for directivity. The reformulated approach of the Diffraction Integral Method from the previous chapter allows source directivity definition. The present chapter outlines the possible mathematical descriptions of directional point sources.

Two different source descriptions are investigated and compared here: a directional point source using a polar directivity function and a directional point source using spheroidal functions. The main requirement for the descriptions is that they should be yielding minimal errors in both the near field where the diffraction occurs and the far field where the observers are located.

3.1 Directional Point Source

Commonly used to capture a specific turbomachinery directivity pattern in empirical estimation tools such as ANOPP, polar directivity functions D are introduced in combination with a point source according to

$$p_i^{directional} = \frac{QD(\theta)}{2\pi r} e^{ikr}, \tag{3.1}$$

where θ is the polar angle.

The directivity function D comes from experimental measures and can either be tabulated or described as a polynomial function. For example, the fan noise module in ANOPP is based on the Heidmann [7] fan noise directivity function.

It is important to note that this directional point source does not satisfy the Helmholtz equation and therefore yields errors in the near field. In the far field, the acoustic pressure follows the Sommerfeld radiation condition

$$\lim_{r\to\infty} \sqrt{r}\left(\frac{\partial}{\partial r} - ik\right) p_i = 0. \tag{3.2}$$

This condition is equivalent to stating that the incident acoustic pressure follows

$$\frac{\partial p_i}{\partial r} - ikp_i = 0$$

in the far field. In other words, the description suggested in Eq.(3.1) is an acceptable description in the far field.

3.2 HELS Directional Point Source

To avoid the errors mentioned above in the near field and to ensure that the Helmholtz equation is satisfied, spheroidal functions can be introduced [33][34] and the directional point source can be written as

$$p_i^{HELS}(\vec{x},\omega) = \sum_{j=0}^{\infty} C_j \Psi_j(\vec{x},\omega) \simeq \sum_{j=0}^{J} C_j \Psi_j(\vec{x},\omega), \tag{3.3}$$

where

$$\Psi_j = \psi_{n,l}(r,\theta,\phi) = h_n(kr) P_{n.,l}(\cos\theta) e^{il\phi}, \tag{3.4}$$

and ω is the source frequency, J is the number of terms in the expansion ($J \leq M$) and M is the number of measurement points. Furthermore, h_n is the n-th spherical Hankel function and $P_{n,l}$ is the associated Legendre polynomial. The indices j, n and

l are related by $j = n^2 + n + l + 1$ with $-n \leq l \leq n$.

Since this description follows the Helmholtz equation and reconstructs the acoustic field using a Least Square fit, it is commonly referred to as a Helmholtz Equation Least Square reconstruction, or short HELS.

The incident acoustic field at each frequency of interest is represented with a different HELS description. For each frequency, the coefficients can be determined via a least square fit on data available in the far field. Matching the assumed form for the incident field and the measured acoustic pressures $p_i^{HELS}(\vec{x_m}, \omega)$ at $\vec{x_m}$, $m = 1..M$, the coefficients $\{C\}_{J\times 1}$ can be obtained using a pseudo-inverse:

$$\left\{p_i^{HELS}(\vec{x_m}, \omega)\right\}_{M\times 1} = [\Psi]_{M\times J}\{C\}_{J\times 1} \tag{3.5}$$

$$\{C\}_{J\times 1} = \left([\Psi]_{M\times J}^T[\Psi]_{M\times J}\right)^{-1}[\Psi_j]_{M\times J}^T\left\{p_i^{HELS}(\vec{x_m}, \omega)\right\}_{M\times 1}. \tag{3.6}$$

3.2.1 Error Assessment of Directional Point Source Description

3.2.1.1 Free Field Comparison

To assess the near field error of the simple directional point source description in Eq.(3.1), the HELS reconstruction in Eq.(3.3) is used for comparison. For both descriptions, the Heidmann fan noise directivity [7] was implemented for a range of reduced frequencies kr. The least square process and directivity function fitting is illustrated in Figure 3-1. A polynomial is used to analytically evaluate the directivity function D. The order of the polynomial was set to 11 to minimize the discrepancies between the directivity function and the experimental data in the far field.

The results of the error analysis are shown in Figure 3-2. The white dashed lines mark the range of kr corresponding to the outline of the HWB airframe investigated here. As expected, significant discrepancies occur in the near field, which can amount to more than 18 dB. The outline of the shielding object appears to be in regions of high discrepancies for half of the frequencies of interest. Therefore, errors in the diffracted field obtained with a directional point source are expected and illustrated

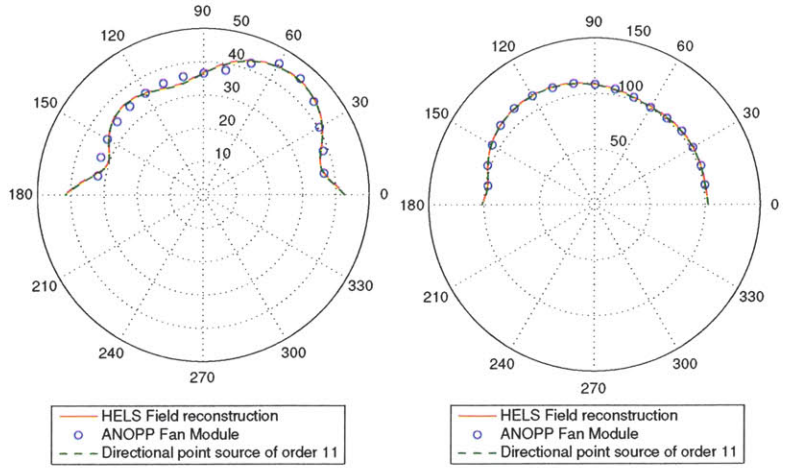

Figure 3-1: Comparison of the polar directivity patterns (in dB) in the far field ($kr = 1000$) obtained with the ANOPP fan module, the corresponding HELS field reconstruction and directional point source. Left: 50 Hz. Right: 10000 Hz.

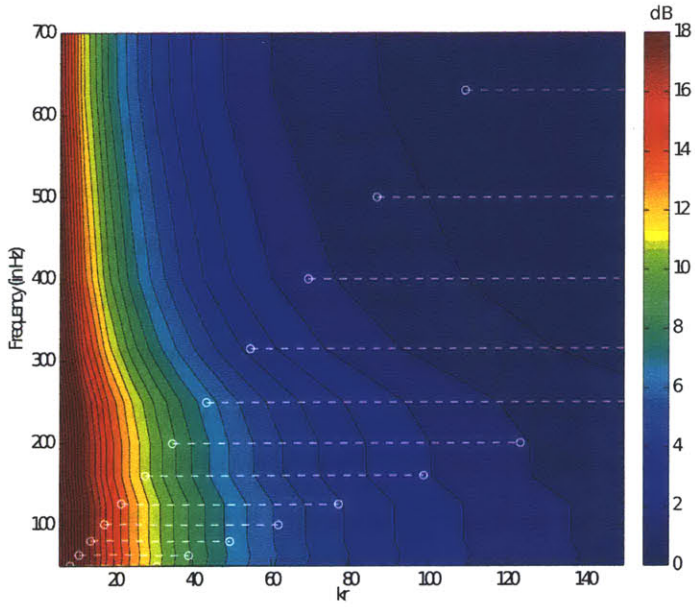

Figure 3-2: Maximum deviation (in dB) in free field between a directional point source description and the corresponding HELS reconstruction.

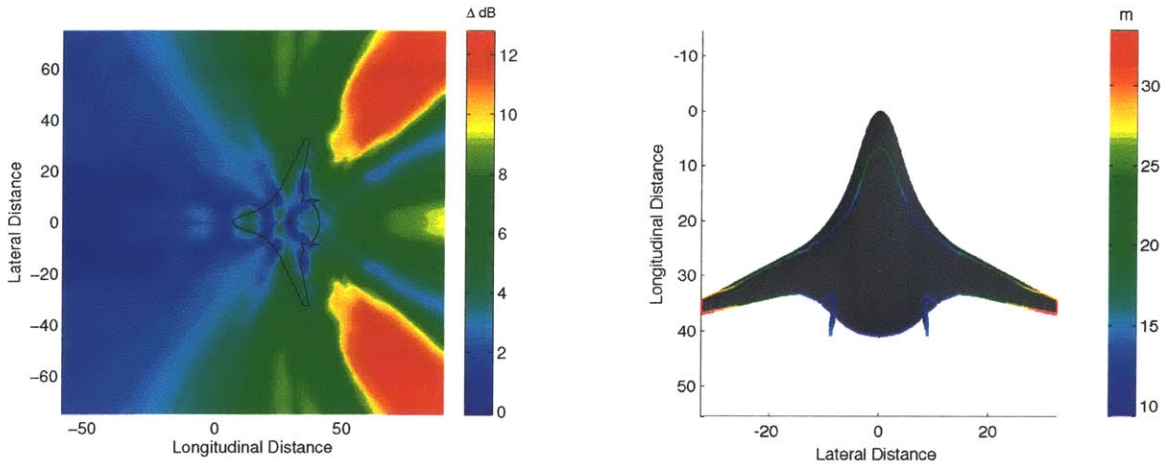

Figure 3-3: Left: noise attenuation pattern comparison: directional point source vs HELS description for a HWB aircraft configuration.
Right: distance between outline points and the source location.

in the next sub-section.

3.2.1.2 Diffracted Field Comparison

Turbomachinery noise shielding by the same HWB airframe is considered. For observers located in the far field, errors in the near field can impact the diffracted far field. To assess the far field error the directional point source is compared with the associated HELS as shown in Figure 3-3.

For locations on the diffracting outline and close to the source, for example in front of the vertical tails, the associated error in the far field is higher than for other locations on the outline, 12 dB in that case. This is due to the above mentionned discrepancies in the near field at the considered frequencies.

3.3 Summary

In summary the use of a simple directivity function for turbomachinery noise directivity description should be avoided as yielding errors up to 18 dB in the near field where the diffraction occurs. Although HELS representations are of higher complexity and computationally more expensive to evaluate than directional point sources, they

are a rigorous representations of directional point sources following the Helmholtz equation. Therefore, HELS representations have been implemented in the Diffraction Integral Method.

Chapter 4

Implementation

This chapter illustrates the integration strategy of the diffraction integral method into ANOPP as well as the implementation of the solver and the source descriptions.

The main challenge for the solver and source description implementation is to formulate the obtained expression for the diffracted field in Eq.(2.24) in terms of geometric parameters. To do so, explicit expressions are derived using the framework introduced by Lummer [19].

4.1 Integration with ANOPP

The implementation of the diffraction integral method for integration with ANOPP is divided into two parts: the "offline part" and the "online part". A flowchart is shown in Figure 4-1.

The offline part is devoted to specifying the source description, flight conditions and shielding object geometry and computing the outline of the object. The outline is defined as the line separating the illuminated and shadow regions of the shielding objects as seen from the source. See Ng [3] for details on the outline searching algorithm. This part is run only once for each aircraft geometry, source type and forward flight conditions.

The online part evaluates the diffraction integral to obtain the noise attenuation due to shielding for each observer location and each frequency. This would take the

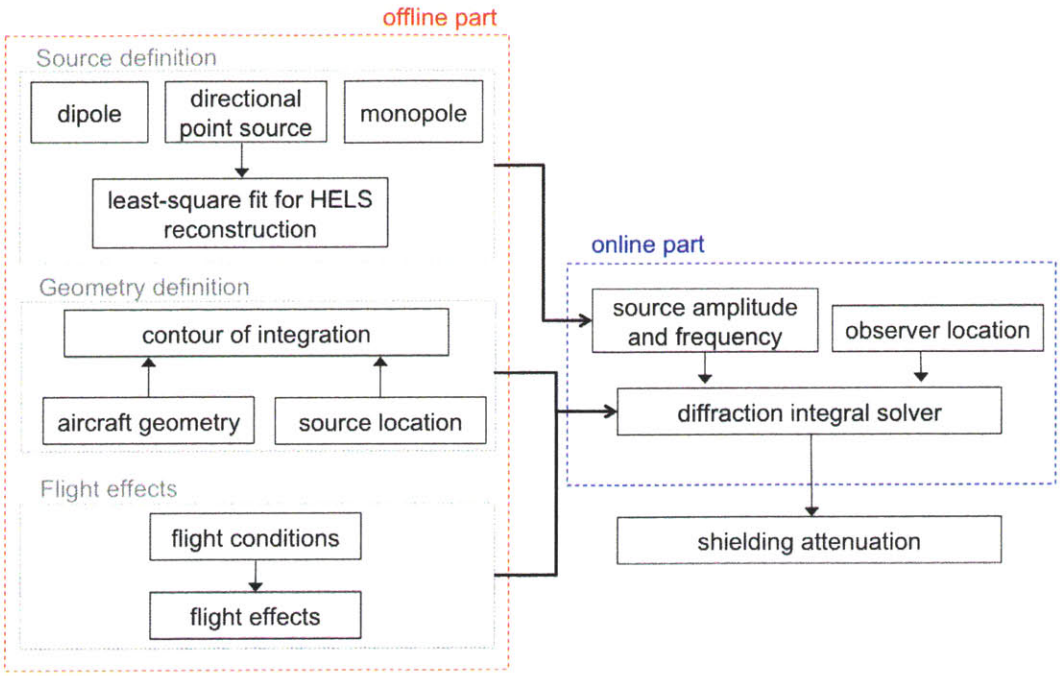

Figure 4-1: DIM structure for integration with ANOPP.

place of ANOPP's Wing module, which employs the barrier shielding method, and is run as part of ANOPP's noise estimation.

4.2 Solver Implementation

The obective is to express the final expression for the uniform asymptotic expansion corresponding to the integration of the diffraction line integral along a linear edge Γ in Eq.(2.24) in terms of geometric parameters.

The functions G and h introduced in the asymptotic expressions need to be expressed in a useful form. Since they involve the stationary phase point location and the first and second derivatives of the phase function, theses quantities need to be derived in explicitly. Further, the strategy followed to evaluate the Fresnel integral and the derivative of the diffraction pattern is outlined.

The final version of the DIM and the expressions detailed here have been implemented in Matlab® to demonstrate and validate the method.

The first step in obtaining explicit expressions is to parametrize the geometry

of the diffraction problem. To do so, the framework and notations introduced by Lummer [19] are considered:

$$\begin{aligned} \vec{a} &= \vec{y_0}, & \vec{b} &= \vec{y_0} - \vec{R} \\ \vec{u} &= \vec{a} \times \vec{b}, & \vec{v} &= \vec{e} \times (\vec{a} - \vec{b}) \\ \vec{w} &= \vec{a} \times \vec{e}, & \vec{z} &= \vec{v} + \vec{w} = \vec{e} \times \vec{b} \\ \alpha &= \vec{a} \cdot \vec{e}, & \beta &= \vec{b} \cdot \vec{e} \\ \gamma &= \vec{a} \cdot \vec{e}, \end{aligned} \tag{4.1}$$

for a source located at the coordinate system's origin, an observer located at $\vec{R}$, $\vec{e}$ and $\vec{y_0}$ the unit vector and arbitrary starting point of Γ respectively. $\vec{\rho}$ and $\vec{r}$ can be expressed in terms of the quantities in Eq.(4.1):

$$\begin{aligned} \vec{\rho} &= \vec{a} + \vec{e}s, & \vec{r} &= \vec{b} + \vec{e}s \\ \rho^2 &= a^2 + 2\alpha s + s^2, & r^2 &= b^2 + 2\beta s + s^2 \\ \vec{\rho} \cdot \vec{r} &= \gamma + (\alpha + \beta)s + s^2, & (\vec{\rho} \times \vec{r}) \cdot d\vec{s} &= (\vec{a} \times \vec{b}) \cdot \vec{e} ds. \end{aligned} \tag{4.2}$$

These notations and expressions will be used throughout the next subsections and corresponding appendices.

4.2.1 Stationary Phase Point Location

The objective is to derive an explicit form for the curvlinear abscissa of the stationary phase point s^* given the same arbitrary linear edge Γ defined in the third section of the first chapter.

Starting from the stationary phase point definition ($g'(s^*) = 0$) and making use of geometrical relations and quantities illustrated in Figure 4-2, it is shown in Appendix C that for the phase function $g(s) = r(s) + \rho(s)$,

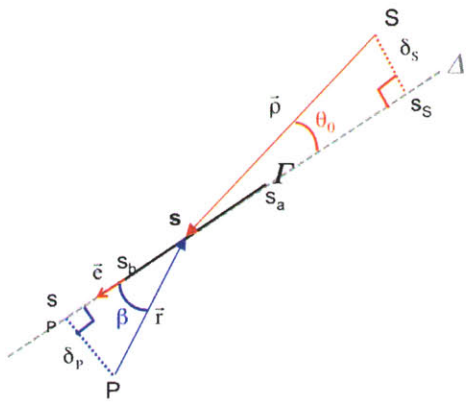

Figure 4-2: Parametrization of geometry for implementation of the diffraction integral method.

$$s^* = \frac{\delta_S s_P + \delta_P s_S}{\delta_P + \delta_S}, \tag{4.3}$$

where δ_S and δ_P are the distances between the source and the line Δ on which the edge is lying and the observer and Δ respecively. Furthermore, s_s and s_P the are abscissae of the projections of P and S on Δ respectively.

4.2.2 Derivatives of the Phase Function

Following the same logic, the first and second derivatives of the phase function can be expressed simply in terms of the quantities defined in Eq.(4.1):

$$\begin{aligned} g'(s) &= \frac{dg}{ds} = \frac{d}{ds}(r(s) + \rho(s)) = \frac{1}{2r}\frac{d}{ds}r^2 + \frac{1}{2\rho}\frac{d}{ds}\rho^2 \\ &= \frac{\alpha + s}{\rho} + \frac{\beta + s}{r} \\ g''(s) &= \frac{d}{ds}(\frac{\alpha + s}{\rho} + \frac{\beta + s}{r}) = \frac{\rho - \frac{(\alpha+s)^2}{\rho}}{\rho^2} + \frac{r - \frac{(\beta+s)^2}{r}}{r^2} \\ &= \frac{1}{r} + \frac{1}{\rho} - \frac{(\alpha + s)^2}{\rho^3} - \frac{(\beta + s)^2}{r^3}. \end{aligned} \tag{4.4}$$

4.2.3 Solution to the Fresnel Integral

Fresnel integrals are used in Eq.(2.24) to describe the behavior of the diffracted field in the transition region. They are evaluated at the values of the detour parameters.

There are two main approaches to evaluating Fresnel integrals. The first approach is to make use of common routines that have been developed in the literature and are known to yield errors less than 10^{-8}. One challenge with these numerical integrators is that extensive calling of such an external script from the main routine can significantly increase the computational cost. An alternative approach is to use an analytical approximation derived in [35] and given by

$$F[x] \simeq \frac{1}{1 - e^{e^{-i\frac{\pi}{4}} 2\sqrt{\pi} x}} + \frac{e^{i\frac{\pi}{4}}}{2\sqrt{\pi}} \frac{e^{ix^2}}{x}. \tag{4.5}$$

The second term is the high frequency asymptotic development (see Eq.(2.21)) and the first term ensures a errors smaller than 10^{-2} near the origin ($x < .1$).

A maximum error of 10^{-2} was deemed acceptable and this last method was therefore implemented in the diffraction integral method.

4.2.4 Derivative of the Diffraction Pattern

To integrate flight effects using the generalized Prandtl-Glauert transformation with a uniform background flow, the first derivative of the pressure field in the modified domain is required (see Eq.(2.33)). A forward-explicit first order accurate finite difference scheme was chosen to evaluate this derivative. This derivative is given as

$$\frac{\partial p_1'}{\partial x_1}(\vec{\xi}) \simeq \frac{p_1'(x_1 + \Delta x_1) - p_1'(x_1)}{\Delta x_1}, \tag{4.6}$$

with Δx_1 the distance between two observers in the modified domain that have the same y_1 and z_1 coordinates.

The error due to neglecting higher order terms is proportional to Δx_1. This quantity can be set arbitrarily small.

For each original observer located at (x, y, z) in the original domain and at (x_1, y_1, z_1)

in the modified domain, an additional observer needs to be defined at $(x_1+\Delta x_1, y_1, z_1)$ to compute the expression in Eq.(4.6). This last consideration multiplies the computational cost by a factor of 2.

4.3 Source Description Implementation

In the source definition part either a monopole, or dipole, or a directional point source can be specified. Four different source noise models were investigated and implemented in the diffraction integral method: (i) monopole, (ii) dipole, (iii) directional point source, and (iv) HELS directional point source (see previous chapter). In the current implementation of the code, any of the above descriptions can be chosen by the user. More details can be found in the User Guide in Appendix C.

The HELS description requires the implementation of associated Legendre functions and spherical hankel functions. The challenge is to evaluate these in a computational cost effective manner since they will be evaluated numerous times during a diffraction computation. Although they can be evaluated using numerical schemes, analytical expressions for these functions have been derived (see for example [5]).

Chapter 5

Validation and Acoustic Shielding Results

This chapter first illustrates the validation of the diffraction integral method with NASA's Fast Scattering Code. The objective is to delineate the applicability and limitations of the method.

A study of the impact of source directivity and flight effects on the N2A aircraft configuration noise shielding pattern using the diffraction integral method is then presented.

5.1 Comparison with NASA's FSC

The diffraction integral method was validated against NASA's Fast Scattering Code on two canonical shielding geometries: a sphere and a circular disk (see Figure 5-1).

It has previously been shown that NASA's FSC yields errors less than 1 dB in comparison with the analytical solution (see [3]) in the case of monopole field diffraction by a sphere. This was expected as the FSC is a high fidelity method (see Chapter 1 for a description of the equivalent source method). The present comparison uses a monopole source description similar to the validation case of the FSC.

The diffraction integral method is expected to perform best at high frequencies and for flat-shaped shielding objects since it is based on the Kirchoff theory of diffraction

which assumes sharp edges and the incident field to be undisturbed by the presence of the object. It inherently does not capture creeping rays [36] and should therefore yield errors in the case of rounded shielding objects. Comparing the diffraction integral method to the FSC for a sphere and a disk that share the same circular outline at several reduced frequencies is used to quantity these limitations.

The attenuation patterns obtained with the diffraction integral method between the sphere and the disk case are identical since the outline of the object is the only geometrical parameter relative to the shielding object that is input.

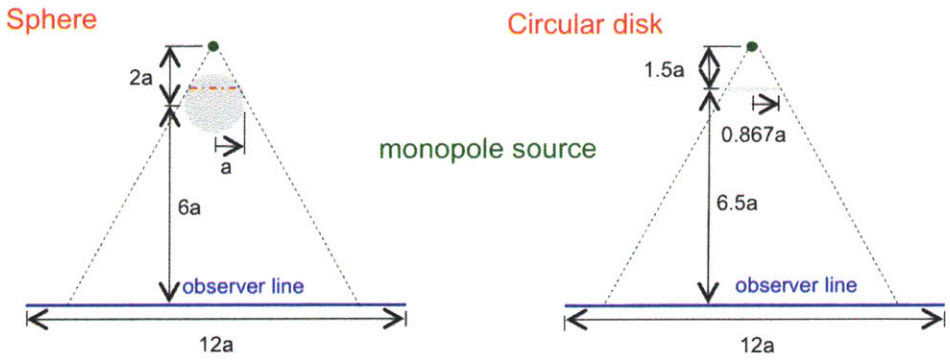

Figure 5-1: Shielding sphere and disk configurations for the validation of the Diffraction Integral Method.

The present comparison is at high reduced frequencies as assumed in the derivation of the method. FSC data at $ka = 92$, 194 and 400 was available for the comparison. Two additional disk shielding cases at $ka = 1$ and 50 are also shown to investigate possible errors at low frequencies. The results are shown in Figures 5-2 and 5-3.

The cases plotted in Figure 5-2 reveal that diffraction integral method is agreeing within a 2 dB margin with the FSC in the disk case. The Sphere shielding cases show a larger discrepancy between the methods that can reach up to 7 dB. This demonstrates that at high frequencies ($ka > 92$), as expected, the method yields small errors for flat-shapped geometries but shows discrepancies in the case of the rounded shielding objects. These discrepancies are due to creeping-ray diffraction [36] which is not captured by the diffraction integral method.

Investigating the errors obtained for disk shielding cases at lower frequencies allows to test both the Kirchoff assumption of an unchanged incident field on the shielding

object and the errors yielded by the asymptotic expansions involved in the derivation (see Chapter 2 for more details). However, the assumption of a flat-shaped shielding object has already been validated above. The cases plotted in Figure 5-3 reveal that at $ka = 50$ the results still agree with a 0.5 dB margin but as the frequency is lowered ($ka = 1$), the discrepancies between the results can reach up to 4 dB.

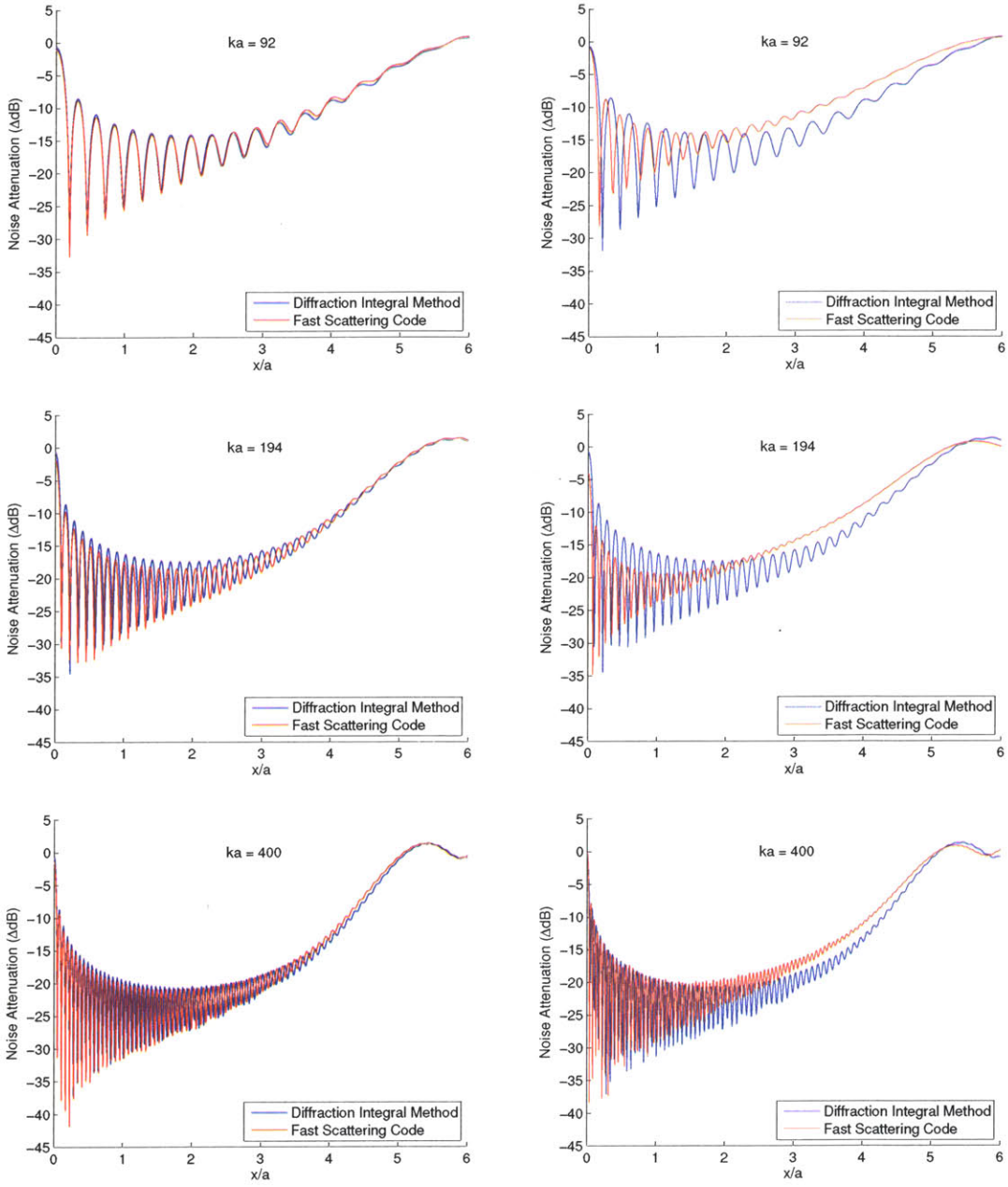

Figure 5-2: Disk (Left) and Sphere (Right) shielding comparisons between DIM and FSC at $ka = 92$, 194 and 400.

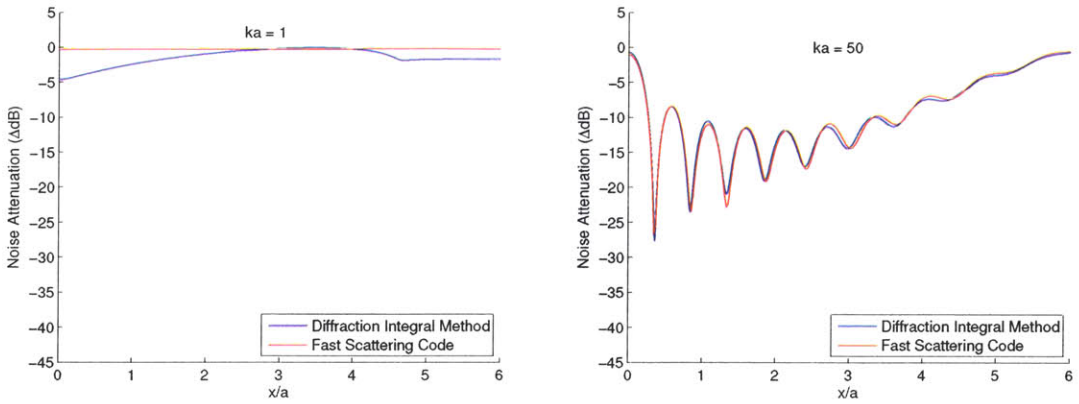

Figure 5-3: Disk shielding comparisons between DIM and FSC at $ka = 1$ (left) and $ka = 50$ (right).

To conclude, the method is validated at high frequencies and for flat-shapped objects for which diffraction is characterized by edge-diffracted rays. It can be applied to rounded objects and at lower frequencies ($ka < 50$) if errors of 4 dB are deemed acceptable by the user.

5.2 Acoustic Shielding Results

The diffraction integral method was applied to the N2A planform [3] described in Chapter 1 to demonstrate its compatibility with alternative aircraft configurations and to investigate the impact of source directivity and flight effects on noise attenuation patterns.

The noise source is placed at the mean location of the two podded engines defined by Boeing and illustrated in Figure 1-3. The shielding aircraft, the source location and the associated diffracting outline are shown in Figure 5-4. The observer plane was placed 30 m below the airframe and the source emitted noise at 24 center frequencies of the 1/3-octave bands accordingly to FAR36 assessments requirements [6].

The reduced frequencies kr corresponding to this source location and frequencies and aircraft outline were computed to be higher than 5 as shown in Figure 3-2. Therefore, the diffraction integral method is expected to yield errors less than 4 dB.

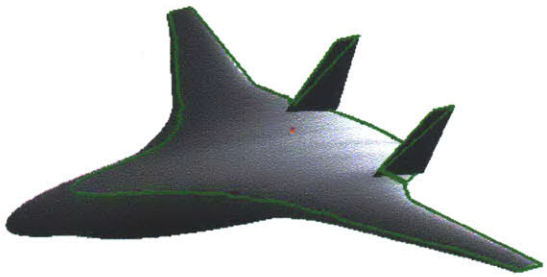

Figure 5-4: Shielding geometry, source location (red) and outline (green).

The overall attenuation is computed using Eq.(2.2).

First, the attenuation patterns using three different noise descriptions of different directivities are compared. Second, the impact of flight effects on noise shielding is presented using the generalized Prandtl-Glauert approach.

5.2.1 Directivity Effects

Three noise descriptions were investigated to investigate the impact of source directivity on noise shielding: a monopole, a dipole and a HELS directional point source. The dipole axis is aligned with the flow.

Although the directivities of the monopole and dipole descriptions do not resemble the directivity of turbomachinery noise, they were used as baselines for comparison with the HELS directional point source. This last description reconstructs turbomachinery noise after a far field least-square fit of experimental data obtained with the Heidmann directivity (see Chapter 3 for more details). The different results are illustrated in Figure 5-6 and the difference in attenuation patterns between the monopole and HELS directional point source descriptions is shown in Figure 5-5.

To interrogate the relation between the incident pressure field and its associated shielding pattern, one should bear in mind that the diffracted field is the sum of the

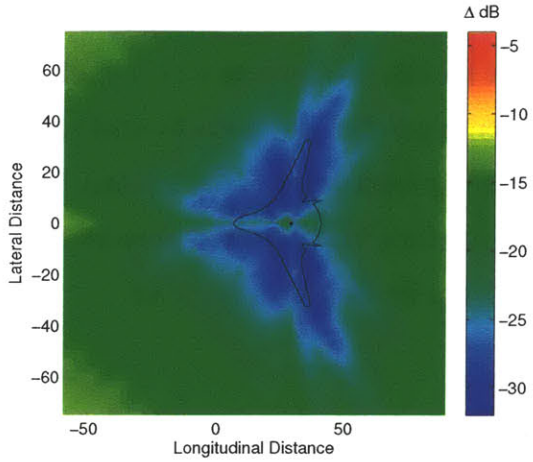

a) Monopole description

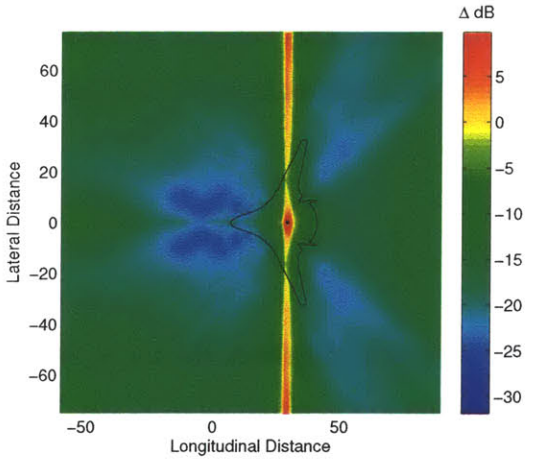

b) Dipole description

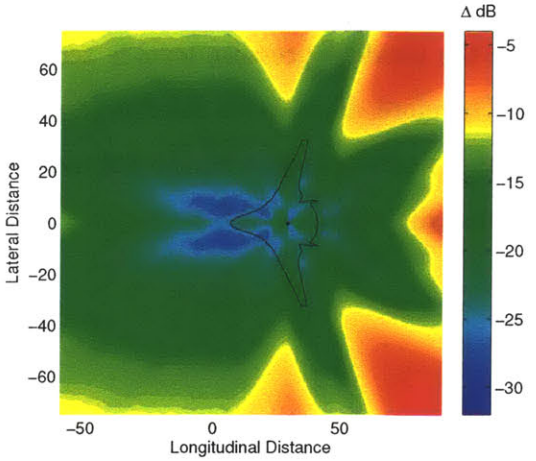

c) HELS directional point source description

Figure 5-5: N2A aircraft configuration attenuation patterns (in dB) for a) monopole, b) dipole description, and c) HELS directional point source description.

incident field and the field diffracted by the outline (see theory of boundary diffracted waves in Chapter 2). The outline is similar to a superposition of monopoles located at each outline point according to the Huyghens-Fresnel principle [18]. The strength of these monopoles sources is proportional to the incident field at this location and of phase opposite in sign. Therefore, the diffracted pressure field level and the amount of shielding increases with the incident pressure level.

All three descriptions based computations predict high levels of shielding up to 30 dB in the forward and aft directions. This behavior is due to similar noise directivities in these directions: all three directivities have local maxima in the aft and forward directions.

On the other hand in the lateral direction, the monopole based shielding calculation over-estimates the insertion loss of up to 10 to 12 dB. This can also be explained by a higher sound pressure level in this direction in the case of a monopole description than in the case of a HELS directional point source. This behavior is exacerbated for a dipole description since the incident pressure level is zero in the direction orthogonal to the dipole axis. Therefore, there is no shielding in that direction. Also, the omnidirectional diffraction of noise by points on the outline contributes to producing a non zero noise level in that direction.

The impact of shielding decrease due to directivity in the lateral direction was found not to affect the final FAR 36 assessment since jet noise is the dominant noise source and is of higher level (see [37] for the noise assessment of the N2A aircraft configuration).

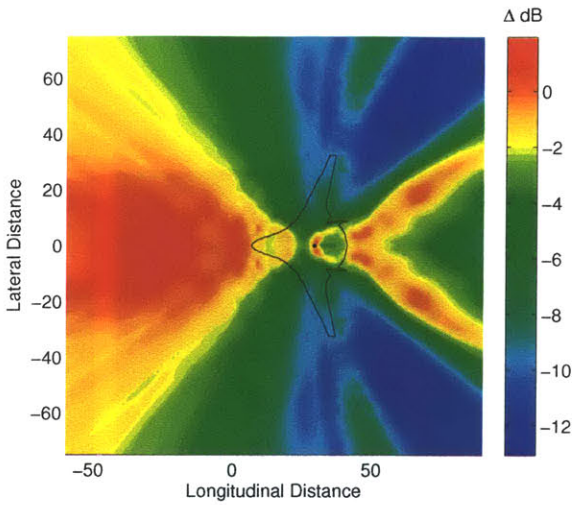

Figure 5-6: Difference in insertion loss (in dB) – monopole vs HELS directional point source.

5.2.2 Flight Effects

Flight effects on insertion loss levels were also investigated. A monopole source description is used to avoid directivity effects on the present study. Two shielding computations were carried out for comparison: a baseline case at static conditions ($M_0 = 0$) and a case at approach conditions ($M_0 = 0.2$, see [32]) as required in a FAR 36 assessment. The difference between the two calculations is shown in Figure 5-7.

The generalized Prandtl-Glauert approach was applied to account for flight effects. To do so, its approach is to distort the shielding geometry in the flow direction by a factor of $1/\sqrt{1 - M_0^2}$ and Dopler shift the incident source frequencies (see Chapter 2 for more details). Differences in noise attenuation between the two investigated cases are therefore explained by the diffracted field phase and amplitude modification induced by the applied transformation.

Differences are mainly localised in the aft and forward directions because of the anisotropy of the applied transformation. The difference reaches up to 2.5 dB in the forward direction.

The observed oscillations in front of the aircraft are due to the difference in noise

frequencies because of Doppler shifting. This results in regions of higher (+ 1.5 dB) and lower shielding (- 2.5 dB).

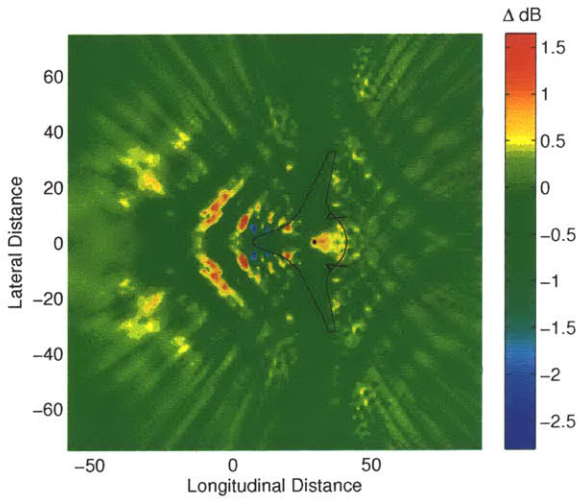

Figure 5-7: Difference in shielding (in dB) relative to static conditions for a forward flight Mach number of $M_0 = 0.2$ using a monopole source.

Chapter 6

Conclusions

6.1 Summary of Results

A high frequency noise shielding methodology based on the Geometrical Theory of Diffraction has been derived, implemented and validated against the Fast Scattering Code. It offers a potential replacement for the barrier shielding method currently implemented in ANOPP. Unlike the barrier shielding method, the new method is applicable to arbitrary shielding geometries, compatible with multipole and directional point sources and can account for flight effects. The diffraction integral method is dramatically faster than higher fidelity methods such as the boundary element method and the equivalent source method since it only involves analytical expressions and does not rely on numerical integration schemes.

The analytical expression of the diffracted field has been obtained using the Miyamoto and Wolf line integral formulation of the Kirchoff surface integral. The shielding object is therefore inherently assumed to have sharp edges and a diffraction pattern characterized by edge-diffracted rays. The line integral was then expressed in terms of Fresnel integrals according to the uniform theory of diffraction by assuming high reduced frequencies. The diffraction integral method also accounts for the effect of forward translation of the noise source and the shielding object using the generalized Prandtl-Glauert transformation. This transformation has been shown to be applicable at Mach numbers corresponding to approach conditions ($M_0 = 0.2$).

The use of a simple directivity function for turbomachinery noise directivity description has been shown to yield errors up to 18 dB in the near field where the diffraction occurs. A directional point source description expressed in terms of spheroidal functions was then implemented in the diffraction integral method as an alternative rigorous description.

The method was validated against the Fast Scattering Code. At high frequencies ($kr > 50$) and for flat shapped objects, the error was found to be less than 1 dB. At lower frequencies ($kr \in [1, 50]$) and for rounded objects, the error was found to reach up to 4 dB.

6.2 Key Contributions

The main contribution of this thesis is the demonstration that concepts from the geometrical theory of diffraction can be used to predict directional point source shielding from arbitrary objects. An approach based on these concepts was formulated and dubbed diffraction integral method. High frequency approximations were also shown to be capable of reducing the diffraction integral into a Fresnel integral, which can be approximated analytically. This yields an analytical and explicit expression for the diffracted field characterized by edge-diffracted rays only. The diffraction integral method is therefore amenable for optimization framework because it is simpler than higher fidelity methods while being of dramatically lower computational cost. It is currently being implemented in NASA's ANOPP and will help in future aircraft design investigations.

Acoustic shielding calculations on the N2A aircraft configuration using a directional point source and a monopole description as a baseline reveal the impact of noise directivity of up to 12 dB in the lateral direction. Flight effects were also shown to impact the shielding level in the forward and aft direction by up to 2.5 dB compared to the static case. These considerations did not affect the final FAR 36 assessment as jet noise is the dominant noise source.

6.3 Recommendations for Future Work

Possible future work includes noise source description enhancement. For example, spinning dipoles to model fan and open rotor noise could be used to capture directivity without requiring a far field least-square fitting of measurement data . Another possible enhancement of the diffraction integral method is the replacement of the Miyamoto and Wolf potential by the diffraction potential developed by Umul [38]. This formulation requires not only the shielding outline but also the distribution of unit normal vectors on the shielding object to compute the diffracted field. Even though this would increase the complexity of the method, shielding results for the disk and sphere shielding cases would be different because of the difference in unit normal vectors. It was shown to be an exact alternative formulation of the Kirchoff surface integral.

Bibliography

[1] F. Collier, "NASA Environmentally Responsible Aviation Project N+2 Advanced Vehicle Concepts NASA Research Announcement (NRA) Draft Solicitation," 2010.

[2] J. I. Hileman, Z. S. Spakovszky and M. Drela, "Airframe Design for Silent Fuel-Efficient Aircraft," *Journal of Aircraft*, vol. 47, no. 3, pp. 956–969, May-June 2010.

[3] L. W. T. Ng, "Design and Acoustic Shielding Prediction of Design and Acoustic Shielding Prediction of Hybrid Wing-Body Aircraft," Master's Thesis, MASSACHUSETTS INSTITUTE OF TECHNOLOGY, June 2009.

[4] A. Agarwal, A. P. Dowling, H. C. Shin and W. Graham, "A Ray Tracing Approach to Calculate Acoustic Shielding by the Silent Aircraft Airframe," in *12th AIAA/CEAS Aeroacoustics Conference (27th AIAA Aeroacoustics Conference).* AIAA 2006-2618, May 2006.

[5] M. Abramowitz and I. A. Stegun, *Handbook of Mathematical Functions with Formulas, Graphs, and Mathematical Tables, 9th printing.* Dover Publications, 1972.

[6] Federal Aviation Administration, "Federal Aviation Regulations Part 36 Sec. B36.7 - Maximum Noise Levels," August 2005.

[7] D. M. Nark, E. Envia and C. L. Burley, "Fan Noise Prediction with Applications to Aircraft System Noise Assessment," in *15th AIAA/CEAS Aeroacoustics Conference (30th AIAA Aeroacoustics Conference).* AIAA 2009-3291, May 2009.

[8] L. L. Beranek, *Noise and Vibration Control.* NY: McGraw-Hill Book Company, 1971, pp. 174-180.

[9] Z. Maekawa, "Noise reduction by screens," *Journal of Applied Acoustics*, pp. 157–173, 1968.

[10] D. Papamoschou, "Prediction of Jet Noise Shielding," in *48th AIAA Aerospace Sciences Meeting Including the New Horizons Forum and Aerospace Exposition.* AIAA 2010-653, Jan 2010.

[11] J. R. P. van Rens, B. J. E. van Rens, T. van Holten, and G. J. J. Ruijgrok, "Sound level prediction using a ray tracing algorithm for a blended wing body," in *6th AIAA/CEAS Aeroacoutics Conference.* AIAA 2000-2069, June 2000.

[12] A. Agarwal and A. P. Dowling, "The Calculation of Acoustic Shielding of Engine Noise by the Silent Aircraft Airframe," in *11th AIAA/CEAS Aeroacoustics Conference (26th AIAA Aeroacoustics Conference).* AIAA 2005-2996, May 2005.

[13] K. Taylor, "A transformationof the acoustic equation with implications for windtunneland low-speedflight tests," vol. 363, no. 1713, The Royal Society of London. Series A, Mathematical and Physical Sciences. The Royal Society, November 1978, pp. 271–281.

[14] C. A. Reimann, A. F. Tinetti and M. H. Dunn, "Noise prediction studies for the blended wing body using the fast scattering code," in *11th AIAA/CEAS Aeroacoustics Conference.* AIAA 2005-2980, May 2005.

[15] M. H. Dunn and A. F. Tinetti, "Aeroacoustic Scattering Via The Equivalent Source Method," in *10th AIAA/CEAS Aeroacoustics Conference.* AIAA 2004-2937, May 2004.

[16] A. F. Tinetti and M. H. Dunn, "Aeroacoustic Noise Prediction Using the Fast Scattering Code," in *11th AIAA/CEAS Aeroacoustics Conference (26th AIAA Aeroacoustics Conference).* AIAA 2005-3061, May 2005.

[17] L. W. T. Ng and Z. S. Spakovszky, "Turbomachinery Noise Shielding Assessment of Advanced Aircraft Configurations," in *16th AIAA/CEAS Aeroacoustics Conference.* AIAA 2010-3914, June 2010.

[18] A. Sommerfeld, "Lectures on Theoretical Physics," in *Optics*, vol. IV. New York, San Francisco, London: Academic Press, 1954.

[19] M. Lummer, "Maggi-Rubinowicz Diffraction Correction for Ray-Tracing Calculations of Engine Noise Shielding," in *14th AIAA/CEAS Aeroacoustics Conference (29th AIAA Aeroacoustics Conference).* AIAA 2008-3050, May 2008.

[20] J. B. Keller, "Geometrical Theory of Diffraction," *Journal of the Optical Society of America*, vol. 52, no. 2, pp. 116–130, 1962.

[21] G. A. Maggi, "Sulla propagazione libra e perturbata delle onde limunose in un mezzo isotropo," *Ann. Mat.*, no. 16, pp. 21–48, 1888.

[22] A. Rubinowicz, "Die Beugungswelle in der Kirchhoffschen Theorie der Beugungserscheinungen," *Ann. Phys.*, no. 53, pp. 257–278, 1917.

[23] K. Miyamoto and E. Wolf, "Generalization of the Maggi-Rubinowicz Theory of the Boundary Diffraction Wave - Part I," *J. Opt. Soc. Am.*, vol. 52, no. 6, pp. 615–625, June 1962.

[24] K. Miyamoto and E. Wolf, "Generalization of the Maggi-Rubinowicz Theory of the Boundary Diffraction Wave - Part II," *J. Opt. Soc. Am.*, vol. 52, no. 6, pp. 626–637, June 1962.

[25] Y. Z. Umul, "Rubinowicz transform of the MTPO surface integrals," *Opt. Commun.*, vol. 281, pp. 5641–5646, 2008.

[26] R. M. Lewist and J. Boersma, "Uniform Asymptotic Theory of Edge Diffraction," *Math. Phys.*, vol. 10, no. 12, pp. 2291–2305, 1969.

[27] S. Ganci, "A General Scalar Solution for the Half-plane Problem," *J. Mod. Opt.*, vol. 42, no. 8, pp. 1707–711, August 1995.

[28] S. Olver, "Numerical Approximation of Highly Oscillatory Integrals," Ph.D. dissertation, Trinity Hall, University of Cambridge, June 2008.

[29] Y. Z. Umul, "Young–Kirchhoff–Rubinowicz theory of diffraction in the light of Sommerfeld's solution," *J. Opt. Soc. Am.*, vol. 25, no. 11, pp. 2734–2742, November 2008.

[30] Y. Z. Umul, "Diffraction of evanescent plane waves by a resistive half-plane," *J. Opt. Soc. Am.*, vol. 24, no. 10, pp. 3226–3232, October 2007.

[31] W. R. Wolf and S. K. Lele, "Fast Acoustic Scattering Simulations with Non-Uniform Potential Flow Effects," in *16th AIAA/CEAS Aeroacoustics Conference.* AIAA 2010-3712, June 2010.

[32] M. A. Sargeant, "Boundary Layer Ingestion for Advanced Airframes," Ph.D. dissertation, Trinity College, Cambridge University, December 2007.

[33] S. F. Wu and X. Zhao, "Combined Helmholtz equation–least squares method for reconstructing acoustic radiation from arbitrarily shaped objects," *J. Acoust. Soc. Am.*, vol. 112, no. 1, pp. 179–188, July 2002.

[34] Z. Wang and S. F. Wu, "Helmholtz equation–least-squares method for reconstructing the acoustic pressure field," *J. Acoust. Soc. Am.*, vol. 192, no. 4, pp. 2020–2032, October 1997.

[35] Y. Z. Umul, "Equivalent functions for the Fresnel integral," *Opt. Express*, vol. 13, no. 21, pp. 8469–8482, October 2005.

[36] B. R. Levy and J. B. Keller, "Diffraction by a smooth object," *Communications on Pure and Applied Mathematics*, vol. 12, no. 1, pp. 159–209, February 1959.

[37] P. A. Weed, "Hybrid Wing-Body Aircraft Noise and Hybrid Wing-Body Aircraft Noise and Performance Assessment," Master's thesis, MASSACHUSETTS INSTITUTE OF TECHNOLOGY, June 2010.

[38] Y. Z. Umul, "Modified diffraction theory of Kirchhoff," *J. Opt. Soc. Am.*, vol. 25, no. 8, pp. 1850–1860, August 2008.

Appendix A

Uniform Contribution of End-Points

The following derivation is based on the derivation detailed in [30]. Consider the general case of a Fourier integral given by

$$I = \int_{\alpha_e}^{\infty} f(\alpha) e^{jkg(\alpha)} d\alpha \tag{A.1}$$

Introducing two arbitrary functions h and G that will be defined in the derivations, Eq.(A.1) can be written as

$$I = \int_{\alpha_e}^{\infty} G(\alpha) h(\alpha) e^{jkg(\alpha)} d\alpha$$

for $G(\alpha) = \frac{f(\alpha)}{h(\alpha)}$.

To separate the contribution of the edge point from the one of the stationary phase point (if there is one), we express the integral in the following way:

$$I = \int_{\alpha_e}^{\infty} \left[G(\alpha) - G(\alpha_e)\right] h(\alpha) e^{jkg(\alpha)} d\alpha + G(\alpha_e) \int_{\alpha_e}^{\infty} h(\alpha) e^{jkg(\alpha)} d\alpha = I_1 + I_2.$$

We express first I_2. By introducing the following detour parameter

$$t = \epsilon \sqrt{k \left| g(\alpha) - g(\alpha^*) \right|},$$

where $\epsilon = \pm 1 \, if \, (\alpha - \alpha^*) \gtrless 0$, I_2 becomes:

$$I_2 = e^{jkg(\alpha_s)} G(\alpha_e) \int_{\alpha_e}^{\infty} \frac{2th(\alpha)}{kg'(\alpha)} e^{jt^2} dt. \tag{A.2}$$

The amplitude function of the integral in Eq.(A.2) must be equal to unity in order to obtain a Fresnel integral. As a result the value of $h(\alpha)$ can be evaluated as

$$h(\alpha) = k \frac{g'(\alpha)}{2t},$$

and I_2 can be represented by a Fresnel function

$$I_2 = e^{jkg(\alpha_s)} G(\alpha_e) \sqrt{\pi} e^{j\frac{\pi}{4}} F[t_e],$$

where $F[x] = \frac{e^{-j\frac{\pi}{4}}}{\sqrt{\pi}} \int_x^{\infty} e^{jt^2} dt$.

The edge point contribution of I_1 is zero because of the term $G(\alpha) - G(\alpha_e)$. We express the stationary phase point contribution as

$$I_1 = e^{jkg(\alpha)} \left[G(\alpha^*) - G(\alpha_e) \right] \sqrt{\pi} e^{j\frac{\pi}{4}} U(-t_e),$$

where $U(x)$ is the unit step function and $h(\alpha_s) = \sqrt{\frac{kg''(\alpha^*)}{2}}$.

Considering the following property of F

$$F[x] = U(-x) + sign(x) F[|x|],$$

we can summarize the asymptotic expansion of Eq.(A.1) as

$$I = \sqrt{\pi} e^{j\frac{\pi}{4}} e^{jkg(\alpha_s)} \left\{ G(\alpha^*) U(-t_e) + G(\alpha_e) sign(t_e) F[|t_e|] \right\}. \tag{A.3}$$

If α_e is also a stationary phase point ($g'(\alpha_e) = g'(\alpha^*) = 0$) Then the previous derivation holds, I_1 is zero and since $F[0] = \frac{1}{2}$,

$$I = I_2 = \frac{\sqrt{\pi}}{2} e^{j\frac{\pi}{4}} e^{jkg(\alpha^*)} G(\alpha^*).$$

Appendix B

Comparison Between the Taylor Transformation and the Generalized Prandtl-Glauert Transformation

B.1 Taylor Transformation

B.1.1 Derivation

At low background flow Mach numbers M_0 ($M_0^2 << 1$), it can be shown that the acoustic velocity potential ϕ is solution of the following perturbed equation [13]

$$\frac{1}{c_0^2}\frac{\partial^2\phi}{\partial t^2} + \frac{2M_0}{c_0}\nabla\hat{\Phi}.\nabla\frac{\partial\phi}{\partial t} - \nabla^2\phi = 0, \tag{B.1}$$

where $\hat{\Phi}$ is the velocity potential of the background flow, c_0 is the speed of sound. It can be noted that taking $M_0 = 1$ transforms the previous equation back to the classical Helmoltz equation.

The goal is to relate ϕ and the acoustic velocity potential without background flow. To do so, Taylor[13] introduced the following transformation

$$(X, Y, Z, T) = (x, y, z, t + \frac{M_0}{c_0}\hat{\Phi}). \tag{B.2}$$

In the transformed domain, we call $\tilde{\phi}$ the acoustic potential so that $\phi(x,y,z,t) = \tilde{\phi}(X,Y,Z,T)$ and ∇_X the gradient:

$$\nabla = \nabla_X + \frac{M_0}{c_0}\nabla\hat{\Phi}\frac{\partial}{\partial T}.$$

It follows that $\tilde{\phi}$ follows the Helmoltz's equation without background flow.

If harmonic time depence is assumed for the acoustic velocity potential in both domains, it is given as

$$\phi(\boldsymbol{x},t) = \phi_0 e^{-i\omega t}$$
$$\tilde{\phi}(\boldsymbol{X},T) = \tilde{\phi}_0 e^{-i\omega T},$$

where ω is the pulsation. The relation of interest is deduced after substituting the transformatiom into the previous relation:

$$\phi_0(\boldsymbol{x},t) = \tilde{\phi}_0(\boldsymbol{X},T)e^{-i\frac{M_0\omega}{c_0}\hat{\Phi}}. \tag{B.3}$$

B.1.2 Application to Insertion Loss Computations

The acoustic pressure can be deduced from the the acoustic potential using

$$p(\boldsymbol{x},t) = -\rho_0 c_0(\frac{1}{c_0}\frac{\partial}{\partial t} + M_0\nabla\hat{\Phi}.\nabla)\phi.$$

By linearity, the acoustic pressure follows the same equation as the acoustic velocity potential (see Eq.(B.1)):

$$\frac{1}{c_0^2}\frac{\partial^2 p}{\partial t^2} + \frac{2M_0}{c_0}\nabla\hat{\Phi}.\nabla\frac{\partial p}{\partial t} - \nabla^2 p = 0,$$

and in the transformed domain (assuming harmonic time dependence):

$$\nabla_X^2\tilde{p} + k^2\tilde{p} = 0,$$

where $k = \frac{\omega}{c_0}$ is the wavenumber.

The pressure is known in the transformed domain since it is domain where the computation is carried. It can be written as

$$\tilde{p_0}(\boldsymbol{X}) = i\rho_0\omega\tilde{\phi_0},$$

from which we can deduce the actual potential

$$\phi_0(\boldsymbol{x}, t) = -\frac{i}{\rho_0\omega}\tilde{p_0}e^{-i\frac{M_0\omega}{c_0}\hat{\Phi}},$$

and the actual acoustic pressure

$$p_0(\boldsymbol{x}) = \left[\tilde{p_0} + \rho_0 c_0 M_0 \left(\frac{i}{\rho_0\omega}\nabla\hat{\Phi}.\nabla\tilde{p_0} - \frac{M_0}{c_0\rho_0}\tilde{p_0}\right)\right] e^{-i\frac{M_0\omega}{c_0}\hat{\Phi}}. \tag{B.4}$$

$\tilde{p_0}$ is identified in the previous formula as the result of a diffraction computation in order to compute the insertion loss.

A choice is to be made regarding $\hat{\Phi}$. Eventhough in the near field $\hat{\Phi}$ is not uniform and its actual distribution results from the Poisson equation $\nabla^2\hat{\Phi} = 0$, it will be identified with its far-field value given as

$$\nabla\hat{\Phi} \simeq \vec{e_x},\ \hat{\Phi} \simeq x.$$

This choice is made such that the transformation captures bulk effects. Further, this is compatible with the DIM assumption that the aircraft is flat.

This simplifies the insertion loss computation and the only remaining impediment is to to compute the derivative of the transmited pressure:

$$p_0(\boldsymbol{x}) = \left[\tilde{p_0}(1 - M_0^2) + i\frac{M_0 c_0}{\omega}\frac{\partial\tilde{p_0}}{\partial x}\right] e^{-i\frac{M_0\omega}{c_0}x} \simeq \left[\tilde{p_0} + i\frac{M_0 c_0}{\omega}\frac{\partial\tilde{p_0}}{\partial x}\right] e^{-i\frac{M\omega}{c_0}x} + \mathcal{O}_0(M_0). \tag{B.5}$$

B.2 Quantitative Comparison

The case of a monopole acoustic source in a uniform background flow is considered. Successively the Taylor transformation and the generalized Prandtl-Glauert approach [15][16] are applied. In this case, the second one is shown to be of higher order than the previous one.

B.2.1 Taylor Transformation

In the transformed domain, the source description can be written as

$$p_{M=0}^{Taylor} = A\frac{e^{ikr}}{r},$$

where r is the distance between the observer and the source and A the source strength. The acoustic pressure in the original domain can be written as

$$p_{M_0>0}^{Taylor} = A\left[\frac{e^{ikr}}{r} + i\frac{M_0 c_0}{\omega}\frac{\partial}{\partial x}\left(\frac{e^{ikr}}{r}\right)\right]e^{-i\frac{M_0\omega}{c_0}x} \tag{B.6}$$

by applying the inverse transformation (see B.5). Substituting $r = \sqrt{x^2+y^2}$ and $\frac{\partial}{\partial x}r = \frac{x}{r}$ in the previous equation, $p_{M_0>0}^{Taylor}$ becomes

$$p_{M_0>0}^{Taylor} = A\frac{e^{ikr}}{r}\left[1 + i\frac{M_0}{k}\frac{x}{r}\left(ik - \frac{1}{r}\right)\right]e^{-iM_0kx}. \tag{B.7}$$

B.2.2 Generalized Prandtl-Glauert Approach

In the transformed domain i.e at a shifted source frequency and a modified coordinate system, the source description writes

$$p_{M_0=0}^{PG} = A\frac{e^{i\kappa r_1}}{r_1},$$

where r_1 is the distance between the observer and the source, A is the source strentgh and κ is the modified wave number. Since $\vec{M_0} = M_0\vec{e_x}$, the inverse of the transfor-

mation matrix B_0 and the modified coordinate system can be expressed as

$$B_0^{-1} = I + \frac{1-\beta_0}{\beta_0 M_0^2}\vec{M_0}\vec{M_0}^T \tag{B.8}$$

$$\begin{pmatrix} x_1 \\ y_1 \\ z_1 \end{pmatrix} = \vec{\xi} = B_0^{-1}\vec{x} = (I + \frac{1-\beta_0}{\beta_0}\begin{pmatrix} 1 & 0 & 0 \\ 0 & 0 & 0 \\ 0 & 0 & 0 \end{pmatrix})\vec{x} = \begin{pmatrix} (1+\frac{1-\beta_0}{\beta_0})x \\ y \\ z \end{pmatrix}. \tag{B.9}$$

The acoustic pressure in the original domain can be deduced after making use the inverse transformation 2.33

$$p^{PG}_{M_0>0}(\vec{\xi}) = \frac{A}{\beta_0}(\frac{e^{i\kappa r_1}}{r_1} + i\frac{M_0}{\kappa}\frac{\partial}{\partial x_1}\frac{e^{i\kappa r_1}}{r_1})e^{-i\kappa\vec{M_0}.\vec{\xi}} \tag{B.10}$$

$$= \frac{A}{\beta_0}\frac{e^{i\kappa r_1}}{r_1}(1 + i\frac{M_0}{\kappa}\frac{x_1}{r_1}\left(i\kappa - \frac{1}{r_1}\right))e^{-i\kappa M_0 x_1}. \tag{B.11}$$

B.2.3 Comparison

It is recognized that expressions in Eq.(B.11) and (B.7) depend on different powers of M_0. The expression obtained using the generalized Prandtl-Glauert approach depends on M_0^2 through the modified forward velocity β_0. On the other hand, the expression obtained using the Taylor transformation depends only on the first power of M_0. The idea is to expand the expression obtained with the generalized Prandtl-Glauert approach using a Taylor expansion and recognize in it the expression obtained with the Taylor transformation.

The following second order expansions are considered to derive the expansion of

Eq.(B.11),

$$
\begin{aligned}
\beta_0 &= \sqrt{1-M_0^2} = 1 - \frac{M_0^2}{2} + o_0(M_0^2) \\
x_1 &= \left(1 + \frac{1-\beta_0}{\beta_0}\right) x = \left(1 + \frac{M_0^2}{2}(1+\frac{M_0^2}{2}) + o_0(M_0^2)\right) x \\
&= \left(1 + \frac{M_0^2}{2}\right) x + o_0(M_0^2) \\
r_1 &= \sqrt{x_1^2 + {y_1}^2} = \sqrt{x^2 + y^2 + M_0^2 x^2 + o_0(M_0^2)} = r\sqrt{1 + M_0^2 \frac{x^2}{r^2} + o_0(M_0^2)} \\
&= r\left(1 + \frac{M_0^2}{2}(\frac{x}{r})^2\right) + o_0(M_0^2),\ (x \neq 0) \\
\frac{x_1}{r_1} &= \frac{x}{r}\left[1 + \frac{M_0^2}{2}(1 - (\frac{x}{r})^2)\right] + o_0(M_0^2) \\
\kappa &= \frac{k}{\beta} = k\left(1 + \frac{M_0^2}{2}\right) + o_0(M_0^2) \\
e^{-i\kappa M_0 x_1} &= e^{-ik\left(1+\frac{M_0^2}{2}\right)M_0\left(1+\frac{M_0^2}{2}\right)x + o_0(M_0^2)} = e^{-ikM_0 x} + o_0(M_0^2) \\
\frac{e^{i\kappa r_1}}{r_1} &= \frac{e^{ik\left(1+\frac{M_0^2}{2}\right)r\left(1+\frac{M_0^2}{2}(\frac{x}{r})^2\right)}}{r}(1 - \frac{M_0^2}{2}(\frac{x}{r})^2) + o_0(M_0^2) \\
&= \frac{e^{ikr}}{r} e^{ikr\frac{M_0^2}{2}(1+(\frac{x}{r})^2)}(1 - \frac{M_0^2}{2}(\frac{x}{r})^2) + o_0(M_0^2) \\
&= \frac{e^{ikr}}{r}\left(1 + ikr\frac{M_0^2}{2}(1+(\frac{x}{r})^2)\right)\left(1 - \frac{M_0^2}{2}(\frac{x}{r})^2\right) + o_0(M_0^2) \\
&= \frac{e^{ikr}}{r}\left(1 + \frac{M_0^2}{2}\left[ikr(1+(\frac{x}{r})^2) - (\frac{x}{r})^2\right]\right) + o_0(M_0^2). \qquad \text{(B.12)}
\end{aligned}
$$

Substituting the previous derivations into the different terms of Eq.(B.11), the following asymptotic expansions can be deduced and will be made of in the following step.

$$\begin{aligned}
\frac{A}{\beta_0}\frac{e^{i\kappa r_1}}{r_1} &= A\frac{e^{ikr}}{r}\left(1+\frac{M_0^2}{2}\left[ikr(1+(\frac{x}{r})^2)-(\frac{x}{r})^2+1\right]\right)+o_0(M_0^2)\\
i\frac{M_0}{\kappa}\frac{x_1}{r_1} &= \frac{iM_0}{k}\frac{x}{r}+o_0(M_0^2)\\
\left(i\kappa-\frac{1}{r_1}\right) &= \left(ik(1+\frac{M_0^2}{2})-\frac{1}{r}(1-iM_0^2(\frac{x}{r})^2)\right)+o_0(M_0^2)\\
&= \left(ik-\frac{1}{r}\right)+\frac{M_0^2}{2}\left\{ik+\frac{x^2}{r^3}\right\}+o_0(M_0^2). \qquad \text{(B.13)}
\end{aligned}$$

The final expansion can be deduced from the previous expansions and is given as

$$p^{PG}_{M_0>0} = A\frac{e^{ikr}}{r}\left(1+i\frac{M_0x}{kr}(ik-\frac{1}{r})+\frac{M_0^2}{2}\left[ikr(1+(\frac{x}{r})^2+1-(\frac{x}{r})^2\right]\right)e^{-ikM_0x}+o_0(M_0^2),$$

and which can also be written as

$$p^{PG}_{M_0>0} = p^{Taylor}_{M_0>0}+A\frac{e^{ikr}}{r}\frac{M_0^2}{2}\left\{ikr\left[1+(\frac{x}{r})^2\right]+1-(\frac{x}{r})^2\right\}e^{-ikM_0x}+o_0(M_0^2) \qquad \text{(B.14)}$$

by recognizing and substituting $p^{Taylor}_{M_0>0}$.

To simplify Eq.(B.14), the case $x = r$ is considered. This correponds to observer located on the x-axis. In that case, the result is simply

$$p^{PG}_{M_0>0} - p^{Taylor}_{M_0>0} \sim iA\frac{e^{ikr}}{r}M_0^2kre^{-ikM_0x},$$

or in a more compact way

$$\frac{p^{PG}_{M_0>0} - p^{Taylor}_{M_0>0}}{p^{Taylor}_{M_0>0}} \sim ikxM_0^2. \qquad \text{(B.15)}$$

Appendix C

Derivation of Stationary Phase Point Location

The objective is to derive an expression for the stationary phase point location to be implemented in the diffraction integral method (see Chapter 4).

It can be deduced geometrically from the definitions of δ_S, δ_P, s_S and s_P introduced in Figure 4-2 in Chapter 4 that

$$r(s) = \sqrt{\delta_s^2 + (s - s_S)^2} \tag{C.1}$$

$$\rho(s) = \sqrt{\delta_P^2 + (s - s_P)^2}. \tag{C.2}$$

The phase function $g(s) = r(s) + \rho(s)$ can be re-written in terms of the previous quantities as

$$g(s) = \sqrt{\delta_s^2 + (s - s_S)^2} + \sqrt{\delta_P^2 + (s - s_P)^2}. \tag{C.3}$$

A first step is to derive the first derivative of g in order to find the stationary phase point,

$$\frac{dg}{ds} = \frac{(s - s_S)}{\rho(s)} + \frac{(s - s_P)}{r(s)} = -\cos\theta_0 + \cos\beta \tag{C.4}$$

by defining the angles θ_0 and β according to Figure 4-2. From the same Figure, it is obvious that

$$\begin{cases} \cos\theta_o = \frac{s-s_S}{\rho(s)}, & \sin\theta_0 = \frac{\delta_S}{\rho(s)} \\ \cos\beta = -\frac{s-s_P}{r(s)}, & \sin\beta = \frac{\delta_P}{r(s)} \end{cases}. \tag{C.5}$$

Therefore substituting the previous trigonometric relations into Eq.(C.4) yields the following characterization of the stationary phase point

$$\cos\theta_0^* = \cos\beta^* \Longrightarrow \theta_0^* = \beta^*.$$

In other terms, $\tan\theta_0^* = \tan\beta^*$, which implies that

$$\frac{\delta_S}{s^* - s_S} = \frac{\delta_P}{s_P - s^*} \Longrightarrow s^* = \frac{\delta_S s_P + \delta_P s_S}{\delta_P + \delta_S}. \tag{C.6}$$

Making use of the notations introduced by Lummer (see Eq.(4.1)), the geometric quantities used in Eq.(C.6) can be expressed as

$$\begin{cases} \delta_S = \sqrt{w^2}, & \delta_P = \sqrt{z^2} \\ s_S = -\vec{a}\cdot\vec{e} = -\alpha, & s_P = -\vec{b}\cdot\vec{e} = -\beta \end{cases}. \tag{C.7}$$

Appendix D

Code Description

The diffraction integral method was implemented as five main Matlab® functions:

- CalculateShielding.m
- create_u0.m
- FindOutline.m
- LSfit.m
- u0.m

The file package 'Diffraction Integral Method v2.00' contains two main folders 'Main' and 'Examples'.

The first one named 'Main' contains all the functions required to use the code.

The second one named 'Examples' contains two subfolders. Each subfolder corresponds to a different example of how to use the code.

The present document describes the functions and script contained in the 'Main' folder. More details about the 'Examples' folder are given in the User Guide.

D.1 Diffraction Integral Method

The capabilities of the diffraction integral method can be summarized as represented in Figure D.1. Following the nomenclature in ANOPP, the code can be divided into

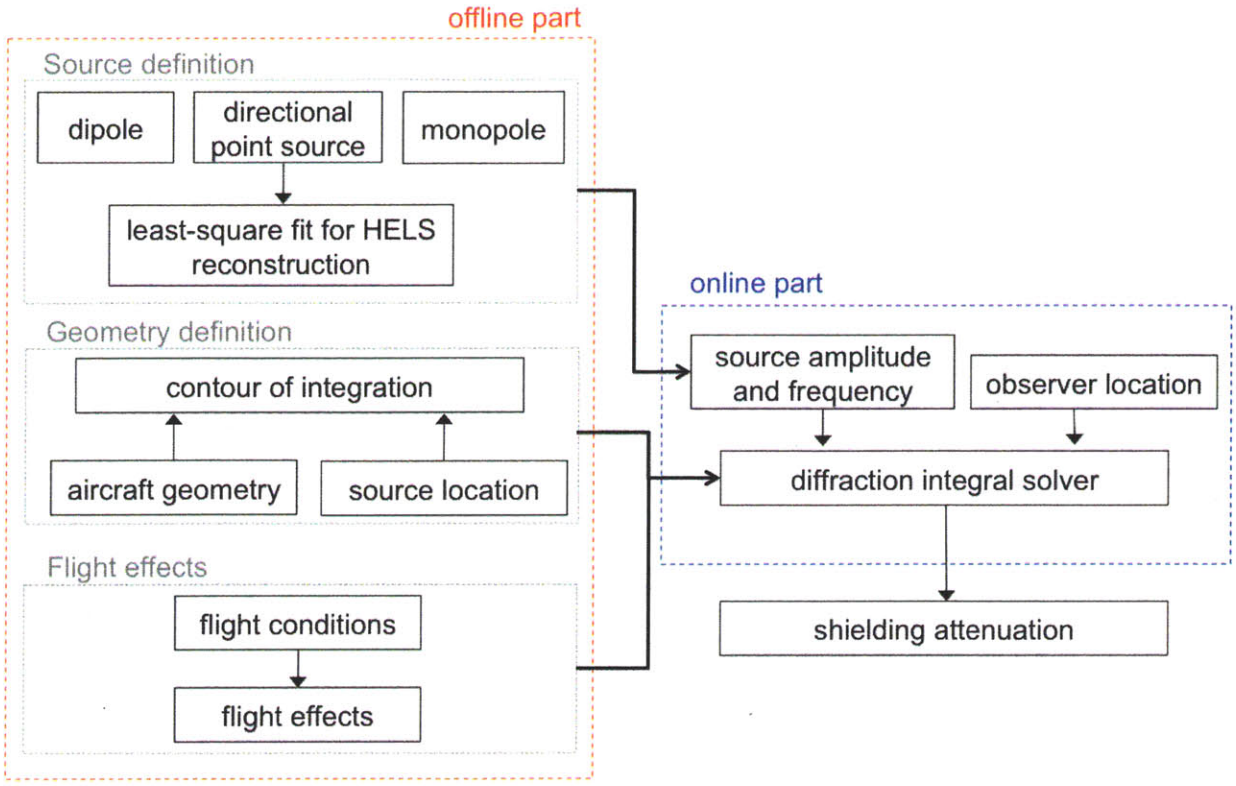

Figure D-1: Diffraction Integral Method v2.00.

two parts: the 'offline part' and the 'online part'.

The offline part determines the flying conditions, the noise source model and the object outline for the contour integration. This can be a separate calculation from the ANOPP noise estimation and is run only once for each aircraft geometry and noise source model.

The online part evaluates the incident source pressure field and the diffraction integral to obtain the noise attenuation due to shielding for each observer location each of frequency in the 1/3-octave band. This would take the place of ANOPP's Wing module, which employs the barrier shielding method, and is run as part of ANOPP's noise estimation.

Both parts have been coded in Matlab® to demonstrate and validate the algorithm.

For more clarity, a flowchart of how the information is exchanged between the

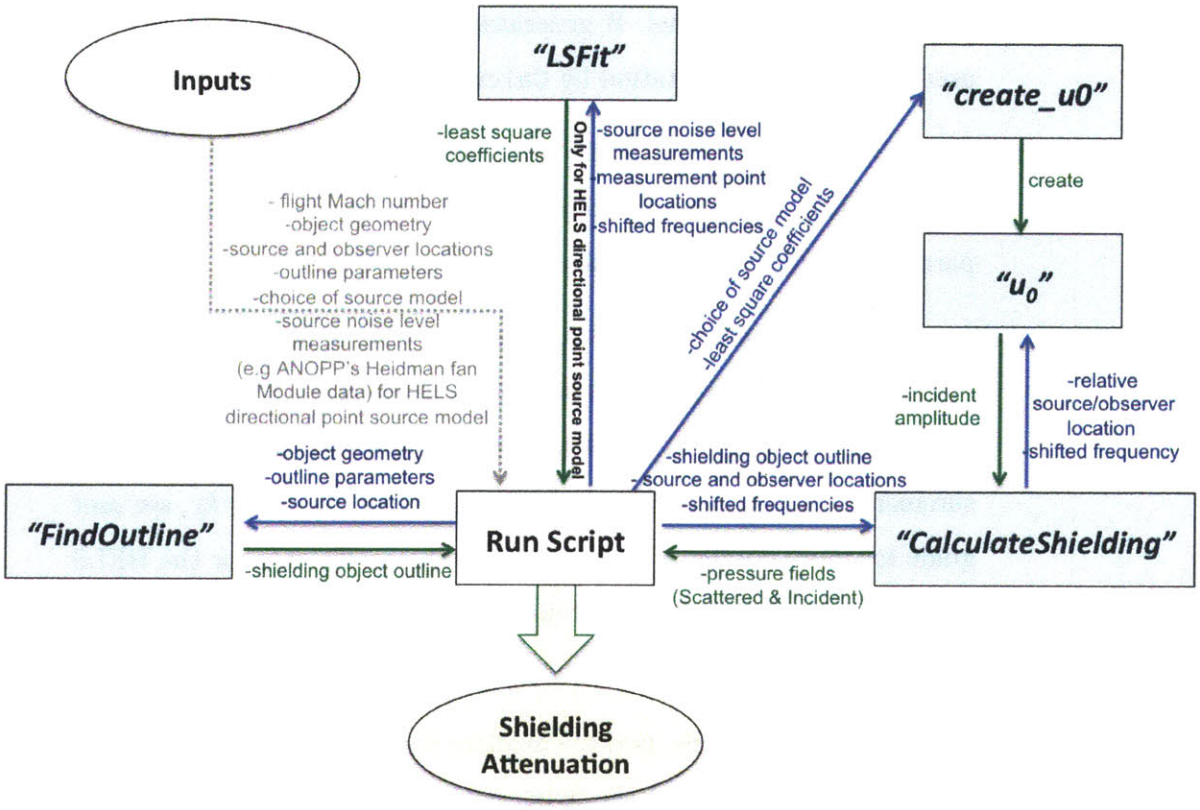

Figure D-2: Code flow chart.

different functions and RunScript is represented in Figure D-2.

D.2 File Structure

The 'Main' folder contains thirteen files:

`CalculateShielding.m` is the function for the "online part" of the diffraction integral method. The inputs are the contour of integration, source location, observer locations, and the frequencies. The outputs are the total transmitted pressure field and the incident pressure field at those observer locations and frequencies.

`create_u0.m` is a function of the 'offline part' of the diffraction integral method. The inputs are the choice of source model and least square coefficients which will be used only if the user selects the HELS direc-

tional point source model. It generates the function `u0.m` that will be used during the computation by `CalculateShielding.m`.

`FindOutline.m` is a function of the "offline part" of the diffraction integral method. The inputs are the object geometry, source location, outline parameters and outputs the shielding object outline.

`LSFit.m` is a function within the "offline part" of the diffraction integral method. The inputs are fan noise levels measurements at discretized frequencies, the frequencies of interest and the locations of the measurements (in terms of polar angles and reduced frequency kr, see user guide for more details). The ouputs are the coefficients for the HELS reconstruction method. This function is run if the user chooses the HELS directional point source model.

`RunScript.m` is the run file used to calculate noise attenuation. It is modified by the user to input the flying conditions, geometry (object and source location), source model, observer locations and outline parameters (see next section). If the HELS directional point source model is chosen, then source noise level measurements and data relative to the measurement points are also required as inputs. It then calls the functions `create_0.m` `FindOutline`.m, transforms the spatial domain for flight effects integration, and calls `CalculateShielding.m` before applying the inverse tranformation in order to create a contour plot of noise attenuation.

`u0.m` is a file generated by `create_u0.m`. user-defined function of the "offline part" of the diffraction integral method. This file is used by `CalculateShielding.m` to evaluate the incident pressure field at each one of the dopler shifted 1/3-octave band frequencies. The inputs are distances between the source and the observers, cosines of the polar angles defined by the angles between the forward direction vector and the vectors pointing from the source to the observers, the frequency of

interest and its corresponding component number in the overall vector of shifted 1/3-octave band frequencies.

`GUI.(m & fig)`, `GUI_directionalpointsource.(m & fig)`, `GUI_objectorientation.(m & fig)`, `gtl_logo.jpg` are files relative to the graphical user interface. They assist the user in inputting the same data as in RunScript.

The 'Examples' folder contains two folders 'N2A' and 'N2B' containing the same files as in 'Main' but with an already configured RunScript, a fan noise level measurements data file 'ANOPP_FanModule_Measurements.mat' and geometry data files '`Geometry N2B.mat`' and '`Geometry N2A.mat`':

`Geometry N2B.mat` is the Matlab® data file containing the coordinates of the N2B geometry. The x, y, and z coordinates of the N2B airfoil sections are stored in the matrices N2B.x, N2B.y, and N2B.z, respectively.

`Geometry N2A.mat` is the Matlab® data file containing the coordinates of the N2A geometry. It contains the x, y, and z coordinates of the N2A airfoil and tails (left and right) sections, stored in the matrices N2A.x, N2A.y, N2A.z, tailL.x, tailL.y, tailL.z and tailR.x, tailR.y, tailR.z respectively.

`ANOPP FanModule Measurements.mat` is a Matlab® data file containing a matrix named 'I_measurements' of fan noise level measurements at 17 evenly distributed polar angles from 10 to 170 rad at kr = 1000. This file has been generated using the ANOPP's Heidman Fan Module.

D.3 Inputs to Main Functions

There are five main functions used to predict noise attenuation due to shielding, `FindOutline`, `CalculateShielding`, `LSFit`, `create_u0` and `u0`. The inputs to the functions are described below.

D.3.1 Find Outline

The syntax for this function is

outline = `FindOutline`(density, minAngle, source, obj, orientation)

- density specifies the grid density on the spherical surface for the projection of the object in terms of the number of grid points per degree longitude or latitude. The function projects the shielding object onto a sphere centered at the source and finds the outermost outline of the projection. Higher density grid produces more accurate results at a cost of longer computational time. However, computational time may also become extremely low to resolve parts of the object if the grid density is too low. There should be enough resolution to distinguish grid points inside the projected outline, on the projected outline, and outside the projected outline for all parts of the object. The optimal value is obtained when no difference in the noise attenuation pattern is observed when the density is increased. Density must be an integer value of at least 1 point per degree.

- minAngle is the minimum angle between the direction vectors of two consecutive outline segments. The function removes points between two outline segments when the two segments change in direction by less than minAngle degrees. Increasing minAngle reduces accuracy on the outline definition,

- source is a 3 $\times$ 1 vector containing the x, y, and z coordinates in meters of the noise source location.

- obj is a structure of three M $\times$ N matrices, obj.x, obj.y, and obj.z, containing the x, y, and z coordinates in meters, respectively, of the 3-D shielding object. The object is described by N planar cross-sections with M points per each cross-section. Each cross-section is a closed contour (e.g. airfoils for wing, circles for tube and wing fuselage).

- orientation specifies the orientation of the planar cross-sections used to define the shielding object. It can have one of three possible values:

'x' refers to cross-sections that are in planes normal to the x-axis. The cross-sections are defined by the columns of obj.y and obj.z. Columns of identical values in obj.x specify the x locations of the cross-sections.

Example: tube and wing fuselage sections are of the 'x' type.

'y' refers to cross-sections that are in planes normal to the y-axis. The cross-sections are defined by the columns of obj.x and obj.z. Columns of identical values in obj.y specify the y locations of the cross-sections.

Example: wing sections are of the 'y' type.

'z' refers to cross-sections that are in planes normal to the z-axis. The cross-sections are defined by the columns of obj.x and obj.y. Columns of identical values in obj.z specify the z locations of the cross-sections.

Example: vertical tail sections are of the 'z' type,

If the object consists of more than one component (e.g. tube and wing fuselage, wing, tail), the coordinates of each component and the orientation of the cross-sections of each component may be entered separately. There is no limit, aside from computational time, on the number of components allowed. The function finds the outermost outline for all components combined. The syntax in this case is

outline = `FindOutline`(density, minAngle, source, obj1, orientation1, obj2, orientation2, obj3, orientation3, ...)

D.3.2 Calculate Shielding

The syntax for this function is

[pScattered, pIncident] = `CalculateShielding`(outline, source, observer, f, ds)

- outline: Structure of three 1 × P vectors containing the x, y, and z coordinates in meters of the P points that define the outermost outline of the object (outline.x,

outline.y, and outline.z). The diffraction integral is a contour integral around the outline, which divides the illuminated side and the shadow side of the shielding object.

- source: 3 × 1 vector containing the x, y, and z coordinates in meters of the noise source location.

- observer: Structure of three 1 × Q vectors containing the x, y, and z coordinates in meters of the Q observer locations (observer.x, observer.y, and observer.z). The noise attenuation is calculated at each of the observer points.

- f: R × 1 vector specifying the R frequencies in Hz at which the computation is carried. To compute an OASPL pattern including flight effects, f would be a vector of shifted 1/3-octave band frequencies and R would be equal to 24. If the flight effects are turned off then f would be a vector of original 1/3 octave band frequencies.

- ds: length in meters of the discretized outline segments. The discretization is necessary to determine if an observer lies inside or outside the shadow region. Smal values of ds result in more accuracy determining so but longer computational time. Note that the discretization has no bearing on the numerical integration; it is only for determining if thc observer is inside or outside the shadow.

D.3.3 LSFit

The syntax for this function is

coefficients = `LSFit`(I_measurements, f, kr, polar_angles)

- I_measurements: T × R matrix containing source noise level measurements in dB at T polar angles defined by the angles between the forward direction vector the vectors pointing from the source to the observers for each one of the R frequencies. Measurements are taken at a given kr and for a zero flying Mach number.

- f: R $\times$ 1 vector specifying the R frequencies in Hz at which the computation is carried. To compute an OASPL pattern including flight effects, f would be a vector of shifted 1/3-octave band frequencies and R would be equal to 24. If the flight effects are turned off then f would be a vector of original 1/3 octave band frequencies.

- kr: scalar specifying the value of the measurements' reduced frequency.

- polar_angles is a 1 $\times$ T vector line specifying the T measurement polar angles in radians.

D.3.4 create_u0

The syntax for this function is

`create_u0`(source_flag, coefficients)

- source_flag: structure of three booleans 'source_flag.monopole', 'source_flag.dipole', 'source_flag.HELS' used to define which source model is to be used in the computation.

- coefficients: F $\times$ R matrix containing the F required coefficients for each of the R frequencies for the HELS directional point source model. To compute OASPL patterns using 17 measurement points at each frequency, F = 16 ($floor(\sqrt{17})^2$), and R = 24 (number of shifted or original 1/3-octave band frequencies).

D.3.5 u0

The syntax for this function is

amplitude = u0(k, rho, costheta, fn)

- k: scalar specifying the source wavenumber in m^{-1}.

- rho: 1 $\times$ Q line vector containing the distances in meters between the source and the observers or between the source and the outline points.

- costheta is a 1 × Q line vector containing the cosines of the polar angles between the inlet vector (pointing in the forward direction) and the vectors defined by source and the observers or by the source and the outline points.

- fn: component number in the overall vector of shifted 1/3-octave band frequencies corresponding to the value of 'k'.

D.4 Outputs of Main Functions

The outputs of the five main functions `FindOutline`, `CalculateShielding`, `LSFit`, `create_u0` and `u0`, are described below.

D.4.1 Find Outline

The syntax for this function is

outline = `FindOutline`(density, minAngle, source, obj, orientation)

- outline: Structure of three 1 × P vectors containing the x, y, and z coordinates in meters of the P points that define the object outline (outline.x, outline.y and outline.z). If the function is unable to find a single outline, then outline will contain more than one element. In this case, outline(i).x, outline(i).y, and outline(i).z contain the coordinates of the ith outline.

D.4.2 Calculate Shielding

The syntax for this function is

[pScattered, pIncident]= `CalculateShielding`(outline, source, observer, f, ds)

- pScattered and pIncident: two R × Q matrices containing the total transmitted and incident pressure fields respectively (in Pa) at the Q observer locations and for each of the R frequencies.

D.4.3 LSFit

The syntax for this function is

coefficients = `LSFit`(fan_noise_measurements, f, kr, polar_angles)

- coefficients: F × R matrix containing the F required coefficients for each of the R frequencies for the HELS directional point source model. To compute OASPL patterns using 17 measurement points at each frequency, F = 16 ($floor(\sqrt{17})^2$), and R = 24 (number of shifted or original 1/3-octave band frequencies).

D.4.4 u0

The syntax for this function is

amplitude = `u0`(k, rho, costheta, fn)

- amplitude: 1 × Q line vector containing the evaluation of the incident pressure field in Pa at Q locations (either observers locations or outline points).

D.5 RunScript

The script '`RunScript.m`'is made of five parts:

- User Inputs.
- Find object outline.
- Generate observers, create u0.
- Domain transformation, Noise scattering computation and inverse transformation.
- Generate figure of the insertion loss.

The inputs and how to enter them are described in the User Guide.

The code calls FindOutline to generate the shielding object outline. The next step and if the flag relative to flight effects is set on true, is to use the transformation detailed in Ref.[15, 16]. The computation is then carried out in the transformed domain. The solution is transposed in the original domain using the inverse transformation.

The last step is to plot a contour of the insertion loss.

Appendix E

User Guide

The present document describes how to use the version 2 of the diffraction integral method.

A brief description of what is in each chapter follows:

- Section 1, describes the structure of the main folder 'Diffraction Integral Method v2.00'.
- Section 2, describes alternatives to starting and running the DIM code.
- Section 3, describes how to specify forward flight conditions.
- Section 4, describes how to specify the source location.
- Section 5, describes how to select one of the available source models.
- Section 6, describes how to input shielding objects.
- Section 7, describes the shielding object's outline parameters and what they do.
- Section 8, describes how to specify the observers' locations.
- Section 9, describes how to save the OASPL pattern.
- Section 9, describes two examples.

E.1 Structure of the Main Folder

The main folder contains two subfolders.

The first one named 'Main' contains all the functions required to use the code.

The second one named 'Examples' contains two subfolders. Each subfolder corresponds to a different example of how to use the code.

E.2 Starting and Running the DIM Code

The DIM code was implemented as five Matlab® functions.

There are two alternative ways of starting and runnin the code.

The first one is to type 'GUI' in the matlab command window after selecting the 'Main Functions' folder as the working folder. A graphical user interface will then be launched helping the user inputing information.

The second one is to open the Matlab® script called 'RunScript' (in the 'Main Functions' folder). The user can then manually update the code to input and select the same information as if he would have used the graphical user interface.

To reduce computational time, it is advized to use the second option.

The following sections describe how to input and select information for the code. For more clarity, both ways of running the code will be described in each section.

E.3 Specifying Forward Flight Conditions

Flight effects can either be turned on or off. If the user chooses to account for them then the flying Mach number has to be specified.

This can be done by

GUI: Checking or Unchecking the 'Account for flight effects' box and filling accordingly the 'Flying Mach Number' field in the 'Flight Conditions' panel.

RunScript: Setting the flight effects flag (variable 'flight_effects_flag' in the script) to true or false accordingly at line 18 and updating the value of the Mach number

(variable 'M') at line 21.

E.4 Defining the Source Location

The source location is to be specified in the same coordinate system as the shielding objects (see Section 6). All dimensions are in meter.

GUI: The user can simply update the fields x, y and z in the 'Point source coordinates' panel.

RunScript: The user can update the values of the variable named 'source' in line 24.

E.5 Selecting a Source Model

The noise source is assumed to be compact and located at a user defined point (see Section 4).

Three noise source models are available in the current version of the code:

- Monopole
- Dipole
- HELS directional point source

The dipole's axis in the corresponding source model is aligned with the mean flow direction (x-direction).

To select one model the user can:

GUI: check the corresponding radio-button in the 'Source Model' panel.

RunScript: set the corresponding flag to true and the others to false in the list of models starting at line 27.

The dipole's axis in the corresponding source model is aligned with the mean flow direction (x-direction).

The HELS directional point source is a model that accurately reconstructs a pressure field anywhere in the space given a set of measurement points. More details can be found in Ref. [33, 34].

The HELS directional point source model requires calibratin so futher information is required by the user. This is:

1. A set of source noise level measurements (in dB) taken at rest (static case) and recorded at:

   (a) 1/3-octave band frequencies if the flight effects are turned off (see section 3) or at shifted 1/3-octave band frequencies if the flight effects are turned on. The relation between shifted and non-shifted frequencies can be described as follows:

   $$\{f_1, f_2, ..f_{24}\}^{shifted}_{1/3octave-band} = \frac{1}{\sqrt{1-M^2}}\{f_1^0, f_2^0, ..f_{24}^0\}_{1/3octave-band}$$

   , with M the flying mach number input in section 3.

   (b) 17 polar angles from 10 to 170 degrees around the object. A polar angle is defined as the angle between the vector pointing from the source to the observer and the forward direction vector (see Figure 1b).

2. The value of the reduced frequency kr at which the measurements have been taken. Here $k = \frac{2\pi f}{c}$ with c being the speed of sound and r the distance between the source and measurement location (in meter). Note that its value is the same for all frequencies so that for each of them, the acoustic radius of the measurement is different.

The data described in 1. is entered as a 17x24 matrix contained in a matlab data file (.mat).

The user can input the required data by:

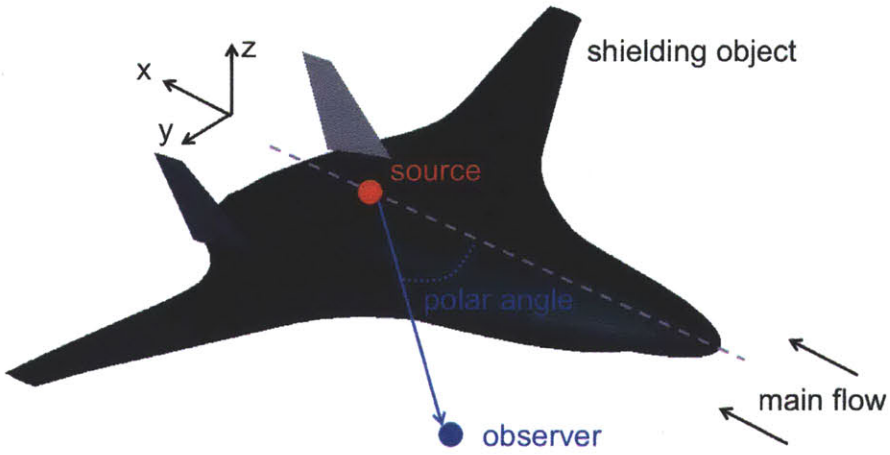

Figure E-1: Polar angle definition.

GUI: updating the field relative to the reduced frequency value *kr* and browsing the 17x24 matrix through the pop-up window.

RunScript: updating the 'filename' and 'pathname' variables (lines 34-35) to indicate the location of the 17x24 matrix and the 'kr' variable (line 36).

E.6 Inputting Shielding Objects

An object is defined as a structure of three M × N matrices, obj.x, obj.y, and obj.z, containing the x, y, and z coordinates in meters, respectively, that define the 3-D shielding object. The object is described by N planar cross-sections, with M points use to define each cross-section. Each cross-section is a closed contour (e.g. airfoils for wing, circles for tube fuselage).

For each object, the user needs to specify the orientation of the planar cross-sections used to define the shielding object. It can have one of three possible values:

- 'x' means cross-sections are in planes normal to the x-axis. The cross-sections are defined by the columns of obj.y and obj.z. Columns of identical values in obj.x specify the x locations of the cross-sections.

Shielding object example: fuselage for a tube and wing configuration.

- 'y' means cross-sections are in planes normal to the y-axis. The cross-sections are defined by the columns of obj.x and obj.z. Columns of identical values in obj.y specify the y locations of the cross-sections.

  Shielding object example: wing.

- 'z' means cross-sections are in planes normal to the z-axis. The cross-sections are defined by the columns of obj.x and obj.y. Columns of identical values in obj.z specify the z locations of the cross-sections.

  Shielding object example: vertical tail.

All the components (e.g wings, tail, fuselage) of the final shielding object are to be saved in a single Matlab® data file.

The object and the orientations of its componenets can be input by:

GUI: Pressing the 'Browse' button down in the 'Diffracting object selection' panel and then specifying the orientation of each component in the pop up window.

RunScript: Specifying the complete pathname of the object data file in line 39 and then updating line 56 by entering the object names and orientations (strings).

E.7 Specifying Shieding Object Outline Parameters

Three parameters relative to the outline are to be specified by the user. A description of them follows:

density specifies the level of accuracy wanted during the search for the shielding object oultine. It is an integer of minimum value 1. High density results in long computational time but very accuratly resolved outlines. The optimal value is the minimal value for which no change in the noise attenuation pattern is observed when increasing this parameter.

minAngle is the minimum angle between the vectors of two consecutive outline segments. Its a strictly positive real number. High density results in too many points used to define the outline. The function removes points between two outline segments when the two segments change in direction by less than minAngle degrees.

ds specifies the length in meters of the discretized outline segments. Its a strictly positive real number. Small value of ds results in more accuracy but longer computational time (during the noise scattering computation).

The user can input these parameters by updating

GUI: the corresponding fields in the 'Outline parameters' panel.

RunScript: the corresponding variables line 42, 43 and 44.

Examples of values for different configurations are given in section 9.

E.8 Specifying the Observer Locations

The observer locations can be defined as lying on a plane below the aircraft (constant z) or on a hemisphere (constant r). All dimensions are in meter.

The user can select a plane or a hemisphere and input the bounds and number of points in the x and y directions or for the θ and ϕ angles (see Figure E-2) by

GUI: checking the corresponding radio-button and updating the fields accordingly in the 'Observer locations' pannel.

RunScript: setting the corresponding flag to true and the other to false (lines 47, 48) and update the following variables accordingly.

E.9 Saving OASPL Pattern

The OASPL pattern obtained after running the code is a matrix of containing the OASPL local value at each observer location.

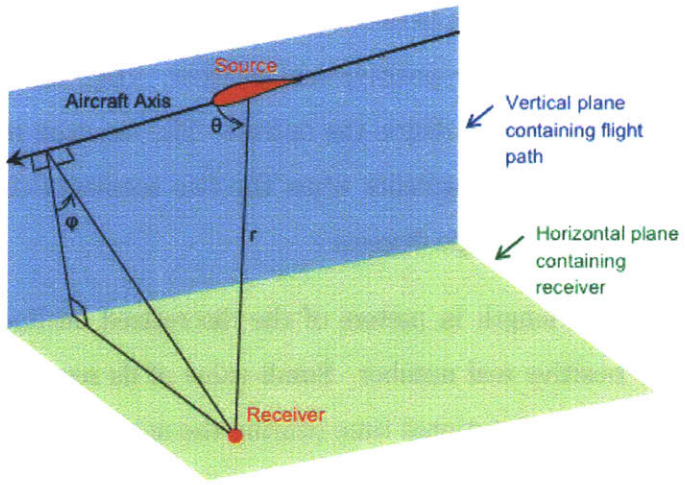

Figure E-2: Spherical coordinates.

To save it, the user can:

GUI: click on the 'save OASPL pattern' button that shows up when the computation is over and indicate the name and directory of the data file that will contain the pattern.

RunScript: save the variable named 'OASPL' in the workspace.

E.10 Examples

In the subfolder 'Examples', the user will find two subfolders named 'N2A' and 'N2B' corresponding to two different Hybrid Wing Body geometries.

Each one of these folders contains the main functions, a geometry file containing the object and a file containing fan noise level measurements ('ANOPP_FanModule_Measurements').

The Matlab® scripts RunScriptN2A.m and RunScriptN2B.m are versions of the general RunScript with updated values. On both of these, the user can modify the flags to understand how the code works.

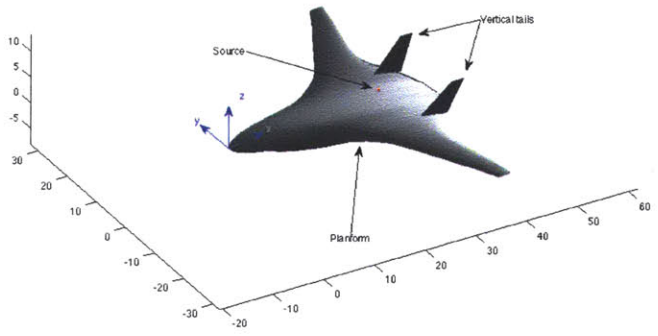

Figure E-3: N2A geometry.

E.10.1 N2A Example

In this example the shielding object is a blended wing body aircraft with two vertical tails (a left and a right one). The origin of the coordinates system is located at the leading edge of the aircraft (see Figure E-3).

The source is located where podded engines would be located i.e on top of the planform. The object has three components 'planform', 'left_tail' and 'right_tail' with 'y', 'z' and 'z' orientations respectively.

The user can then modify the source definition and the observer locations. See Figure E-4 and E-5 for screen captures of the inputs and results.

E.10.2 N2B Example

In this example the shielding object is a blended wing body aircraft without vertical tails. The origin of the coordinates system is located at the leading edge of the aircraft (see Figure E-6).

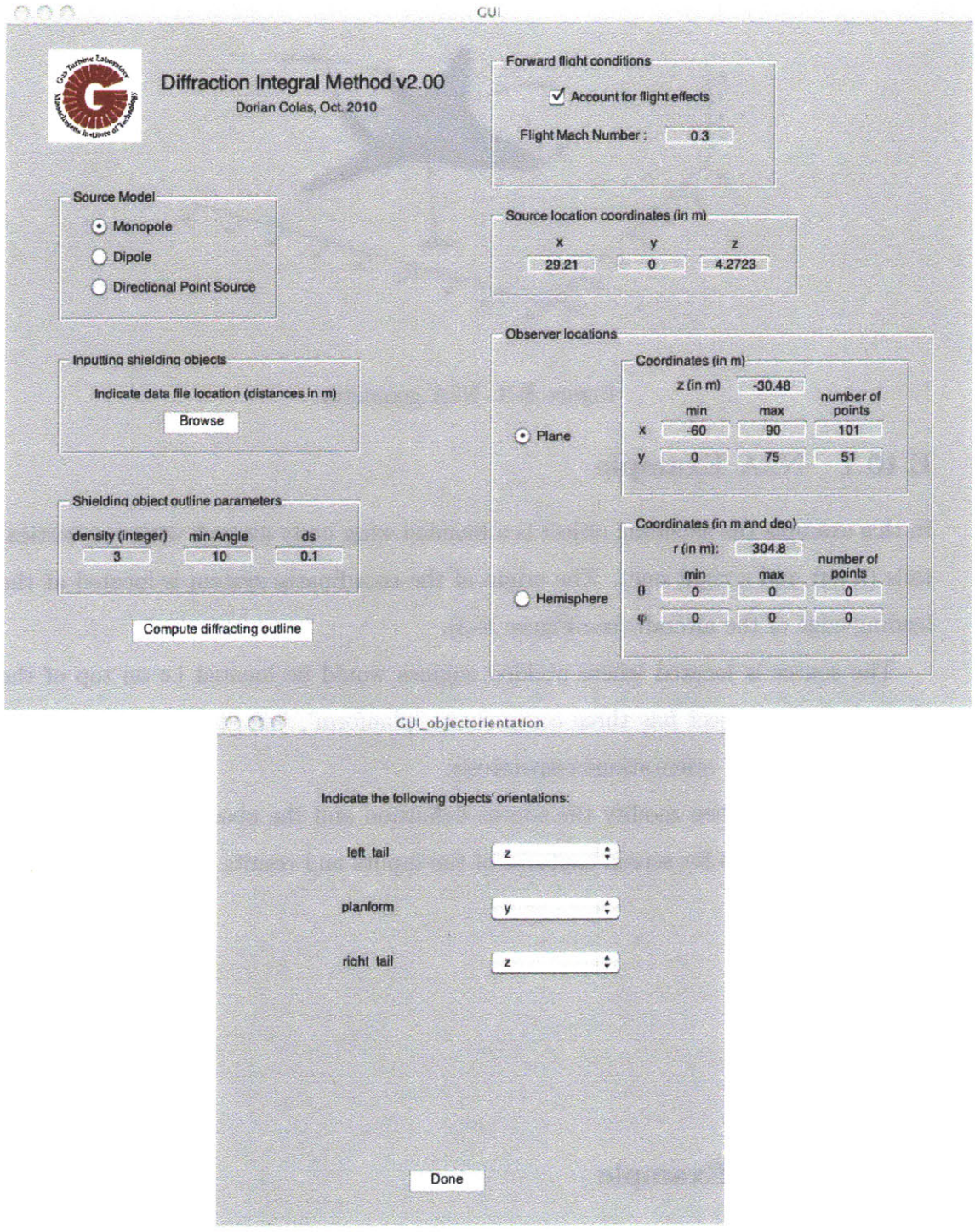

Figure E-4: Screen captures, N2A example, inputs.

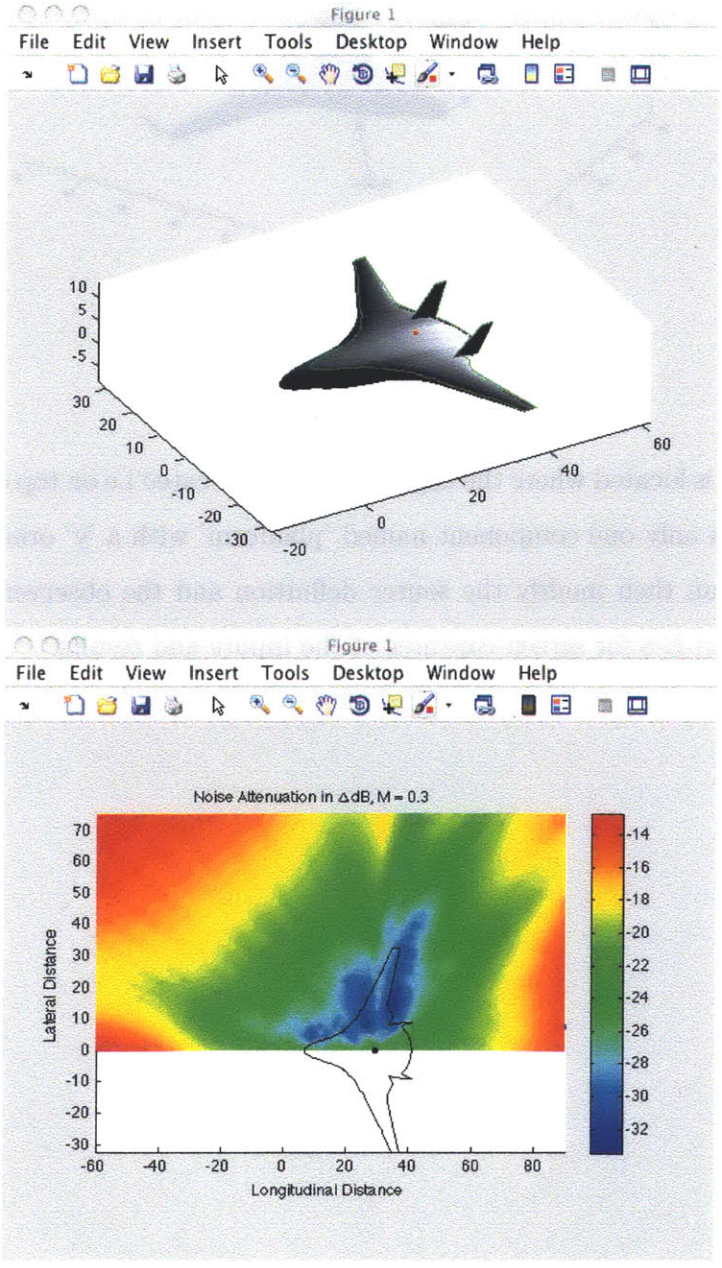

Figure E-5: Screen captures, N2A example, outputs.

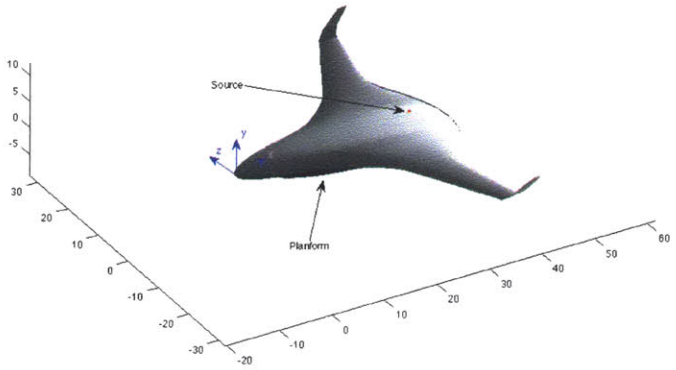

Figure E-6: N2B geometry.

The source is located where the engines would be located i.e on top of the planform. The object has only one component named 'planform' with a 'y' orientation.

The user can then modify the source definition and the observer locations. See Figures E-7 and E-8 for screen captures of the inputs and results.

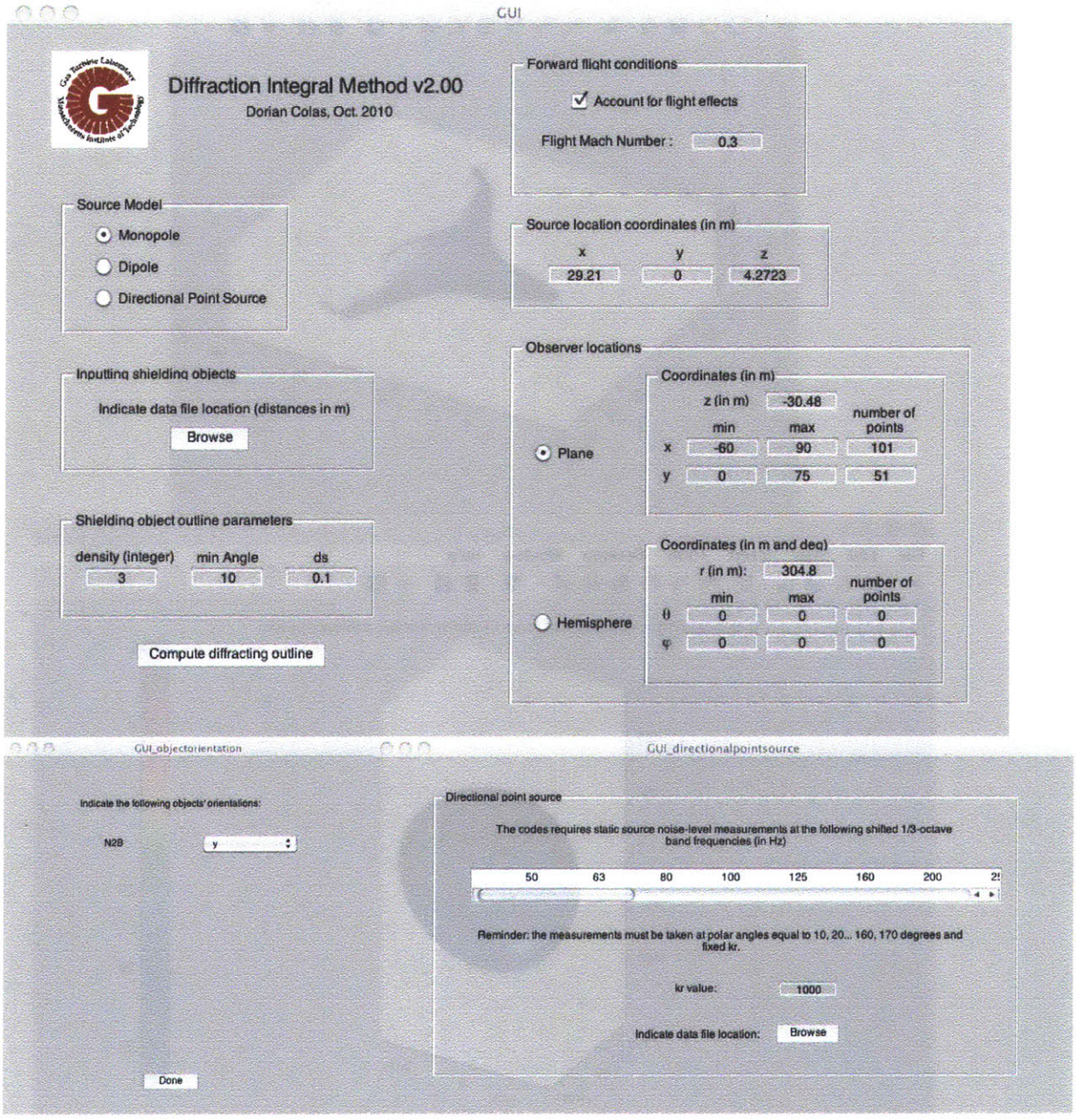

Figure E-7: Screen captures, N2B example, inputs.

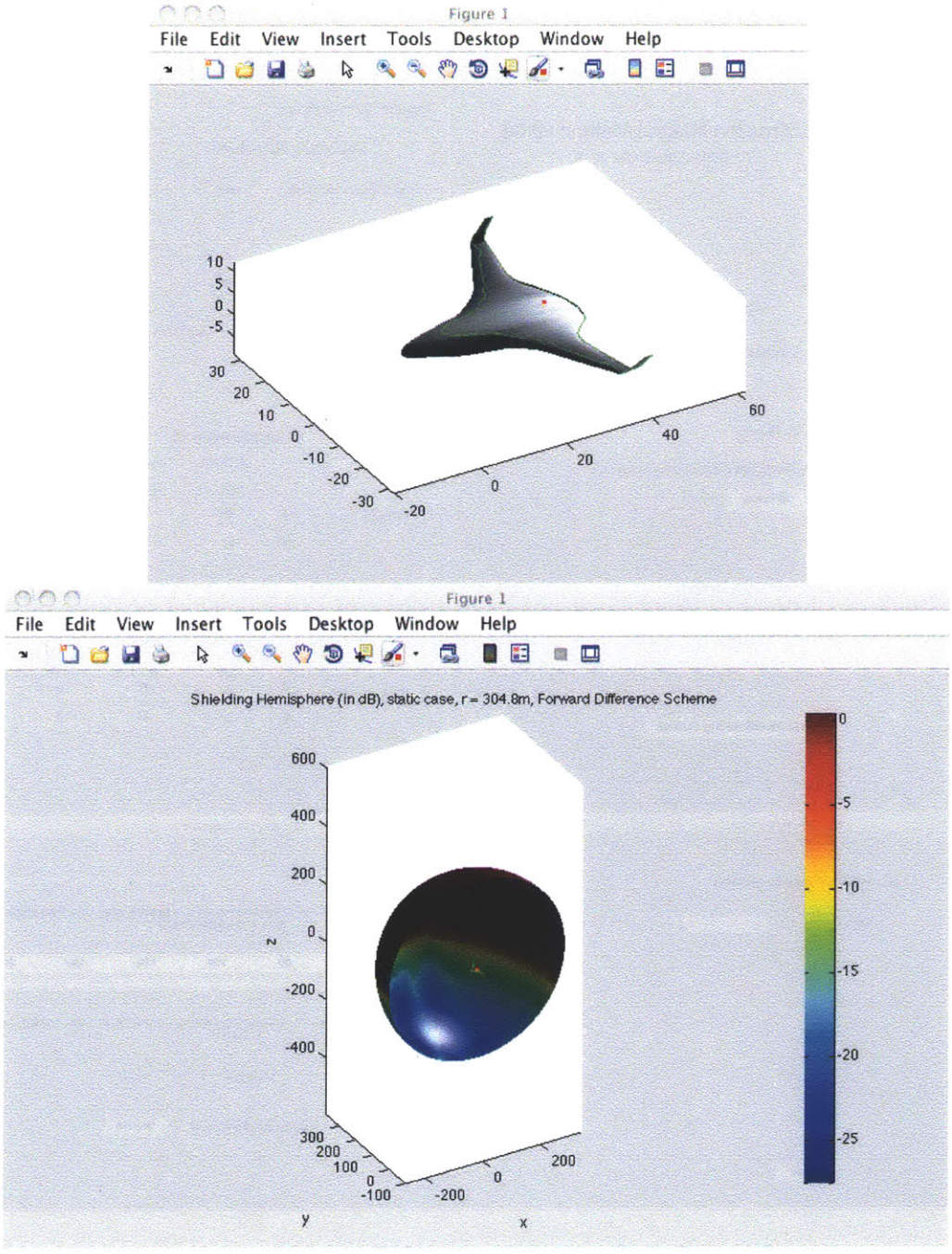

Figure E-8: Screen captures, N2B example, outputs.

Appendix F

Algorithmic Logic

The present document details the algorithmic logic of the Diffraction Integral Method v2.00 (DIM v2.00).

The structure of the DIM v2.00 is detailed in 'Diffraction Integral Method v2.00: Code description'. It is summarized in the flowchart shown in Figure F-1.

To make it easier to read, the indices associated with the discretized outline points, observer locations and frequencies are the same throughout the document and are recaped in Table F.1. This is also graphically represented in Figure F-2.

F.1 RunScript

F.1.1 Inputs

- Flight effects flag and flying Mach number M
- Source location (x_{source}, y_{source}, z_{source})
- Choice of source description (monopole, dipole, HELS directional point source)

Quantity	Notation	Index
Outline point	$\vec{\rho_i}$	i
Observer point	$\vec{R_j}$	j
Frequency,wavenumber	f_n, k_n	n

Table F.1: Indices convention.

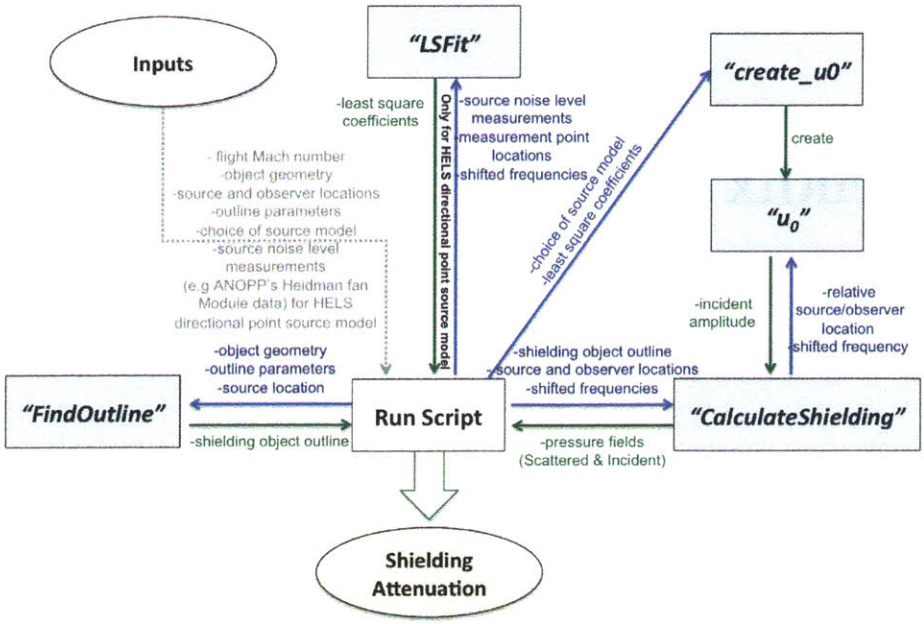

Figure F-1: DIM v2.00: Code Flowchart.

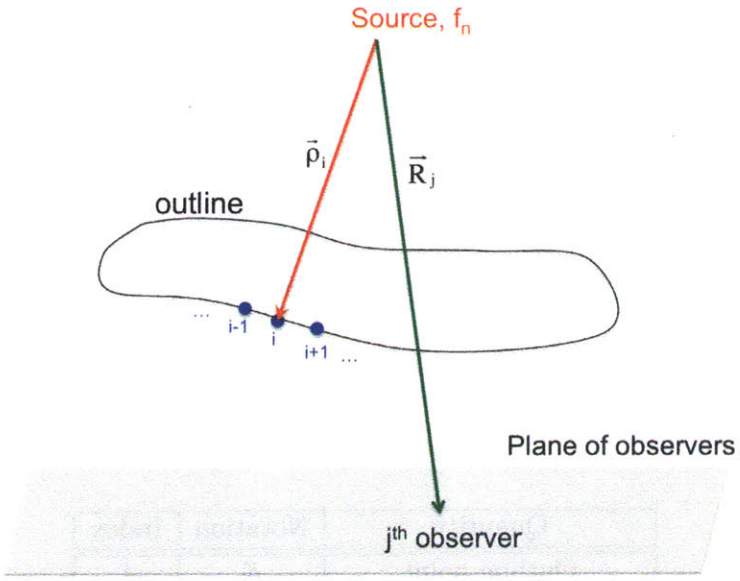

Figure F-2: Indices on problem geometry.

- If flag(HELS directional point source)==true
  - source noise measurement data (see 'LSFit' inputs for more details)
- Diffracting object defined in the same coordinate system as the source
- Outline discretization parameters (density, minAngle, outline_ds)
- Surface of observer locations (z-plane or hemisphere)
  - For a constant-z plane (defined in the same system as the source location and the shielding object):
    * Starting and ending coordinates (x_0, y_0) and (x_1, y_1) respectively
    * Number of points along each axis
    * Altitude z
  - For a hemisphere around the source
    * Starting and ending azymuthal and longitudinal angles (ϕ_0, ϕ_1), (θ_0, θ_1) respectively.
    * Number of points along the azymuthal and longitudinal directions (n_θ, n_ϕ)
    * Radius r_0

N.B: The cartesian and spherical coordinate systems are defined in Figure F.1.1.

F.1.2 Outputs

- $\{SPL_{n,j}\}_{n,j}$ Ensemble of noise attenuation patters for each frequency f_n and at each observer location $\vec{R_j}$
- $\{OASPL_j\}_j$: Ensemble of Overall noise attenuation pattern at each observer location $\vec{R_j}$

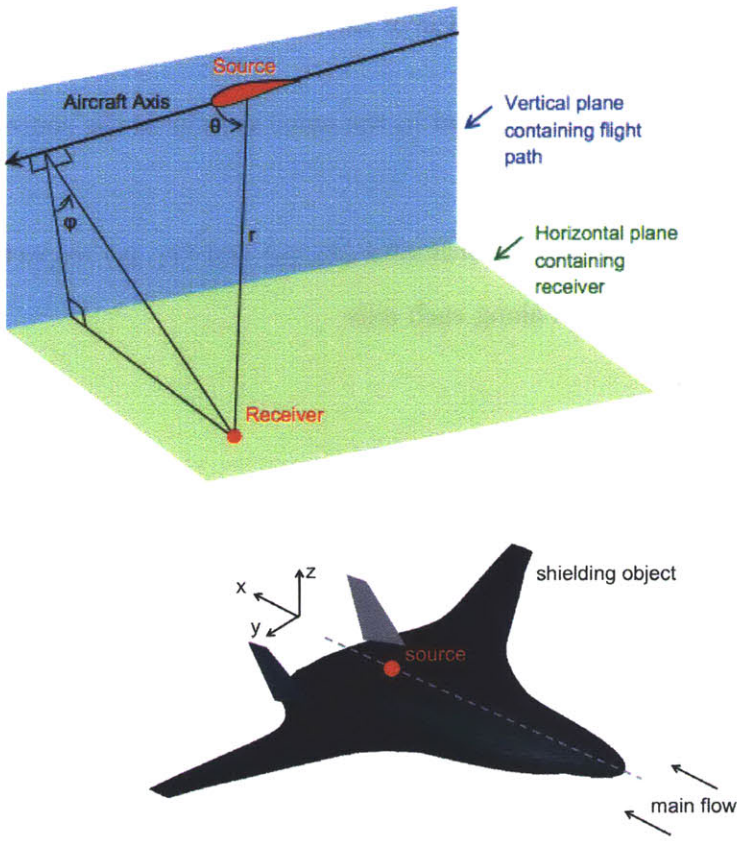

Figure F-3: Coordinate systems (top: spherical, bottom: cartesian).

F.1.3 Code Logic

- Call 'FindOutline' and store object outline for specified density, minAngle, source location.
- Store observers.

N.B: at this stage, the source does not have to be on the origin of the coordinate system.

- Store vector of 1/3-Octave band frequencies $\{f_n\}_n$:

$$\{f_n\}_n = (50, 63, 80, 100, 125, 160, 200, 250, 315, 400, 500, 630, 800, 1000, 1250, ... \\ ..., 1600, 2000, 2500, 3150, 4000, 5000, 6300, 8000, 10000)^\top$$

- If flag(flight effects) == true, compute and store
  - $\beta = \sqrt{1 - M^2}$
  - Dopler shifted ensemble of frequencies: $\{\tilde{f}_n\}_n = \frac{\{f_n\}_n}{\beta}$
  - Associated ensemble of shifted wavenumbers: $\{\kappa_n\}_n = \frac{2\pi\{\tilde{f}_n\}_n}{c}$ (c: speed of sound)
- Else, store: $\{\tilde{f}_n\}_n = \{f_n\}_n$
- If flag(directional point source)==true
  - Call 'LSFit' and get $\{C_{J\times 1}\}_n$ for each n component of $\{\tilde{f}_n\}_n$
- Call 'create_u0' to create source amplitude file 'u0'
- If flag(flight effects) == true
  - Apply Prandtl-Glauert's approach:

* Dilate x-coordinate of outline points, observers and source locations by dividing by β:

$$\tilde{x} = \frac{x}{\beta}$$

- Call 'CalculateShielding' to compute incident and scattered pressure fieds at each observer $\vec{R_j}$ and for each n frequency ($\{p^{n,j}_{incident}\}_{n,j}$, $\{p^{n,j}_{object}\}_{n,j}$: respectively). The geometry and frequencies to be passed in as inputs are the modified ones/shifted ones.

- Apply inverse transformation to get fields at the specified flying Mach number ($\{p^{M>0,n,j}_{incident}\}_{n,j}$, $\{p^{M>0,n,j}_{object}\}_{n,j}$) for each n frequency and each observer location

  * For all observers and frequencies, compute the $\tilde{x}$-derivative of $p^{M>0,n,j}_{incident}$, $p^{M>0,n,j}_{object}$ using a 1st order finite difference scheme:

$$\frac{\partial p}{\partial \tilde{x}} = \frac{p(\tilde{x} + \Delta\tilde{x}) - p(\tilde{x})}{\Delta\tilde{x}}$$

  NB: In the case where observers are lying on plane of constant z coordinate no extra computation is required to compute the above derivative. On the contrary, in the case of a hemisphere an extra computation is required. The only difference with the previous computation is that the x-coordinate of the observers must be shifted of $\Delta\tilde{x}$. A good choice of $\Delta\tilde{x}$ is

$$\Delta\tilde{x} = \frac{r_0}{\beta}\frac{\theta_1 - \theta_0}{n_\theta}$$

  * Translate modified coordinate system so that the source is located at the origin

$$\begin{cases} \tilde{x} & = \tilde{x} - \frac{x_{source}}{\beta} \\ \tilde{y} & = \tilde{y} - y_{source} \\ \tilde{z} & = \tilde{z} - z_{source} \end{cases}$$

  * For all observers and frequencies

· Compute

$$\begin{cases} p_{incident}^{M>0,n,j} &= \left(p_{incident}^{n,j} + \frac{iM}{\kappa_n} \frac{\partial p_{incident}^{n,j}}{\partial \tilde{x}} \right) e^{-iM\kappa_n \tilde{x}_j} \\ p_{object}^{M>0,n,j} &= \left(p_{scattered}^{n,j} + \frac{iM}{\kappa_n} \frac{\partial p_{object}^{n,j}}{\partial \tilde{x}} \right) e^{-iM\kappa_n \tilde{x}_j} \end{cases}$$

· Deduce attenuation at each frequency and observer location

$$SPL_{n,j} = 20 \log_{10} \frac{p_{object}^{M>0,n,j}}{p_{incident}^{M>0,n,j}}$$

– For all observer locations, compute overall attenuation ($OASPL_j$):

$$OASPL_j = 10 \log_{10} \sum_{n=1}^{24} \left(\frac{p_{object}^{M>0,n,j}}{p_{incident}^{M>0,n,j}} \right)^2$$

- Else (i.e flag(flight effects) == false)

– Call 'CalculateShielding' to compute incident and scattered pressure fieds at each observer $\vec{R}_j$ and for each n frequency ($\{p_{incident}^{n,j}\}_{n,j}$, $\{p_{object}^{n,j}\}_{n,j}$: respectively).

– For all observers and frequencies

* Compute attenuation for each n frequency

$$SPL_{n,j} = 20 \log_{10} \frac{p_{object}^{n,j}}{p_{incident}^{n,j}}$$

– For all observer locations, compute overall attenuation ($OASPL_j$):

$$OASPL_j = 10 \log_{10} \sum_{n=1}^{24} \left(\frac{p_{object}^{n,j}}{p_{incident}^{n,j}} \right)^2$$

F.2 FindOutline

F.2.1 Inputs

- Density
- minAngle
- Source location (x_{source}, y_{source}, z_{source})
- Shielding object
- Orientation of shielding object's cross sections

F.2.2 Outputs

- $\{\vec{\rho_i}\}_i$: Ensemble of discretized outline points forming a closed counter-clockwise oriented contour

F.2.3 Code Logic

This part of the DIM v2.00 has not evolved since the DIM V1.00 (see [3]).

F.3 LSFit

F.3.1 Inputs

- Ensemble of source noise measurement levels (in dB) '$\{I^n_{measurements}\}_n$' at each frequency $\tilde{f}_n$ (shifted or unshifted 1/3 octave band frequencies depending on flag(flight_effects))

N.B: Those measurements are taken at a constant reduced frequency value kr i.e taken on a circle around the source. The radius of the circle depends on the wavenumber k_n or the frequency f_n. In addition, kr is the same between frequencies (reason why there is no 'n' index). It is preferably high (100-1000) to ensure that the measurement is taken in the far field.

- Reduced frequency kr value
- Frequencies $\{\tilde{f}_n\}_n$
- Polar angles $\{\theta_j\}_j$ (defined as in Figure F.1.1)
- Number of measurement points n_θ

N.B: Using 19 points of measurements equally spaced ($\{\theta_j\}_j = \{0..10..20...180\}$ deg) will give a well behaved and accurate source description in the near field without prohibitively increasing the computational cost.

F.3.2 Outputs

- Coefficients $\{C^n_{J\times 1}\}_n$ for each frequency f_n (see below)

F.3.3 Code Logic

- For each frequency$\tilde{f}_n$
  - For each measurement point , store the corresponding pressure amplitude:

$$p_{n,j} = p_{ref} 10^{\frac{I^{n,j}_{measurements}}{20}}$$

    with $p_{ref} = 10^{-12} Pa$

  N.B: for each frequency, $\{p_{n,j}\}_j$ is a $n_\theta \times 1$ vector.

  - wavenumber:

$$k_i = \frac{2\pi}{c}\tilde{f}_i$$

    with $c = 340 m.s^{-1}$

  - Acoustic radii (distance between source and measurement points)

$$r_n = \frac{kr}{k_n}$$

- Compute maximum degree of the Legendre polynomials in the spheroidal functions expansion N

$$N = floor(\sqrt{n_\theta}) - 1$$

- Compute number of term in the expansion J

$$J = (N+1)^2$$

- Construct and store a matrix of indices called '$Tree$'
  - for ν from 0 to N by 1
    - for l from $-\nu$ to ν by 1
      - Compute γ: $\gamma = \nu^2 + \nu + l + 1$
      - $\begin{cases} Tree(\gamma, 1) & = \nu \\ Tree(\gamma, 2) & = l \end{cases}$

- Construct spheroidal function defined as $\Psi_\gamma(kr, \cos\theta) = P^{Tree(\gamma,2)}_{Tree(\gamma,1)}(\cos\theta) h_{Tree(\gamma,1)}(kr)$
  - $P^{Tree(j,2)}_{Tree(j,1)}$ or P^l_ν is the associated Legendre function and can be expressed analytically (see Figure F-4)
  - $h_{Tree(j,1)}$ or h_ν is the spherical Hankel function of order ν and can be expressed analytically (see Figure F-4)

- Construct matrix $\Psi_{M\times J}$
  - for j from 0 to M
    - for γ from 0 to J
      - Compute: $\Psi_{M\times J}(j, \gamma) = \Psi_\gamma(kr, \cos\theta_j)$

- For each frequency, compute and return vector of coefficients $\{C^n_{J\times 1}\}_n$

$$\{C^n_{J\times 1}\}_n = \left([\Psi]^T_{M\times J}\Psi_{M\times J}\right)^{-1}[\Psi]^T_{M\times J}\{p_{n,j}\}_n$$

N.B: $\left([\Psi]^T_{M\times J}\Psi_{M\times J}\right)^{-1}[\Psi]^T_{M\times J}$ is the pseudo-inverse of $\Psi_{M\times J}$

F.4 create_u0

F.4.1 Inputs

- Source flags: flag(monopole), flag(HELS directional point source), flag(dipole)
- Coefficients $\{C^n_{J\times 1}\}_n$ from LSFit. If flag(HELS directional point source)==false, then one can simply input 0 for this argument

F.4.2 Outputs

- File 'u0' to be used by 'CalculateShielding' during a computation. This file describes the amplitude of the incident source. 'u0' has four inputs:
  - k_n : wavenumber corresponding to the frequency at which we want to evaluate the source field
  - n: corresponding component number of the frequency in the overall vector of shifted or original 1/3-Octave band frequencies. *Example:* for f=50Hz, $n = 1$, $k_1 = .92m^{-1}$, (50Hz is the first 1/3-Octave band frequency).
  - $|\vec{R_j}| = R_j$: distance between the source and a considered observer. This could also be ρ_i because the source will be evaluated at both outline points (noted as $\vec{\rho_i}$) and far field observers (noted as $\vec{R_j}$)
  - $\cos\theta_j$: cosine of polar angle between the source and the observer (defined as in Figure F.1.1)

F.4.3 Code logic

- If flag(monopole)==true

$$u_0(k_n, R_j, \cos\theta_j, n) = \frac{1}{R_j}$$

$$
\begin{aligned}
P_0^0(x) &= 1 \\
P_1^{-1}(x) &= -\frac{1}{2}P_1^1(x) \\
P_1^0(x) &= x \\
P_1^1(x) &= -(1-x^2)^{1/2} \\
P_2^{-2}(x) &= \frac{1}{24}P_2^2(x) \\
P_2^{-1}(x) &= -\frac{1}{6}P_2^1(x) \\
P_2^0(x) &= \frac{1}{2}(3x^2-1) \\
P_2^1(x) &= -3x(1-x^2)^{1/2} \\
P_2^2(x) &= 3(1-x^2) \\
P_3^{-3}(x) &= \frac{-1}{720}P_3^3(x) \\
P_3^{-2}(x) &= \frac{1}{120}P_3^2(x) \\
P_3^{-1}(x) &= \frac{-1}{12}P_3^1(x) \\
P_3^0(x) &= \frac{1}{2}(5x^3-3x) \\
P_3^1(x) &= -\frac{3}{2}(5x^2-1)(1-x^2)^{1/2} \\
P_3^2(x) &= 15x(1-x^2) \\
P_3^3(x) &= -15(1-x^2)^{3/2}
\end{aligned}
$$

a) First associated Legendre functions

$$
\begin{aligned}
h_0^{(1)}(z) &= -ie^{iz}\frac{1}{z} \\
h_1^{(1)}(z) &= -e^{iz}\frac{z+i}{z} \\
h_2^{(1)}(z) &= ie^{iz}\frac{z^2+3iz-3}{z^3} \\
h_3^{(1)}(z) &= e^{iz}\frac{z^3+6iz^2-15z-15i}{z^4}
\end{aligned}
$$

b) First spherical Hankel functions

Figure F-4: Analytical expressions [5] of the first a) associated Legendre functions and b) spherical Hankel functions.

- If flag(dipole)==true

$$u_0(k_n, R_j, \cos\theta_j, n) = \frac{\cos\theta_j}{R_j^2}(1 - ik_nR_j)$$

- If flag(HELS directional point source)==true

  - Recover N (maximum degree of the associated Legendre function in the expansion) from J:

$$N = sqrt(J) - 1$$

  - Construct the same matrix of indices $'Tree'$ as in LSFit:

    * for ν from 0 to N by 1 and for l from $-\nu$ to ν by 1

      · Compute γ: $\gamma = \nu^2 + \nu + l + 1$

      · Compute and store $'Tree'$:

$$\begin{cases} Tree(\gamma, 1) & = \nu \\ Tree(\gamma, 2) & = l \end{cases}$$

  - Construct spheroidal function without phase contribution:

$$\Phi_\gamma(k_nR_j, \cos\theta_j) = \frac{\Psi_j(k_nR_j, \cos\theta_j)}{e^{ikR_j}} = P^{Tree(\gamma,2)}_{Tree(\gamma,1)}(\cos\theta_j)\frac{h_{Tree(\gamma,1)}(k_nR_j)}{e^{ik_nR_j}}$$

  - Constructing source amplitude:

$$u_0(k_n, R_j, \cos\theta_j, n) = \sum_{\gamma=1}^{J}\{C^n_{J\times 1}\}^\gamma_n\Phi_\gamma(k_nR_j, \cos\theta_j)$$

    where $\{C^n_{J\times 1}\}^\gamma_n$ is the γ^{th}component of $\{C^n_{J\times 1}\}_n$.

F.5 u0

F.5.1 Inputs

- k_n : wavenumber corresponding to the frequency n
- n: corresponding component number of the frequency in the overall vector of shifted or original 1/3 octave band frequencies
- R_j: distance between the source and the observer
- $\cos\theta_j$: cosine of the polar angle between the source and the observer (defined as in Figure F.1.1)

F.5.2 Outputs

- $u_0(k_n, R_j, \cos\theta_j, n)$: Amplitude value of the incident field at a given observer location and for a specified frequency.

F.6 Code Logic

The code is written by 'create_u0'. It contains all the quantities to evaluate the source.

N.B: to gain speed, one can enclose an already computed matrix of indices $'Tree'$.

F.7 CalculateShielding

F.7.1 Inputs

- $\mathcal{L} = \{\vec{\rho_i}\}_i$: Ensemble of outline point coordinates
- Source coordinates (x_{source}, y_{source}, z_{source})
- $\mathcal{O} = \left\{\vec{R_j}\right\}_j$: Ensemble of observer coordinates
- $\{\tilde{f_n}\}_n$: Frequencies

F.7.2 Outputs

- $\{p^{n,j}_{object}\}_{n,j}$: Ensemble of total scattered pressure field for all observers $\vec{R}_j$ and at each frequency n
- $\{p^{n,j}_{incident}\}_{n,j}$: Ensemble of incident field evaluated for all observers $\vec{R}_j$ and at each frequency n

F.7.3 Code logic

- Translate ensemble of outline and observers so that the source is at the origin.

$$\begin{cases} \vec{\rho}_i & = \vec{\rho}_i - (x_{source}, y_{source}, z_{source}) \\ \vec{R}_j & = \vec{R}_j - (x_{source}, y_{source}, z_{source}) \end{cases}$$

- Make sure outline is a closed contour (i.e end == start).
- By calling 'CheckShadow'
  - Check if each observer $\vec{R}_j$ is in the shadow and store the associated values of the function χ_j (1 if in the lite region, 0 otherwise).
  - Check the outline is counter-clockwise oriented as viewed from the source and if not update the outline.
- For all observers $\vec{R}_j$
  - Call 'PrepareIntegral' to compute and store geometric parameters for integral computation performed later with the 'Integrate' function
  - Compute $\cos\theta_j$:

$$\cos\theta_j = -\hat{x}.\vec{R}_j$$

    $\hat{x}$ being the unit base vector in the x-direction (see figure F.1.1).
  - For all frequencies in $\{f_n\}_n$:
    * wavenumber k_n : $k_n = \frac{2\pi}{c} f_n$

* Call 'Integrate': compute and store result ($p^{n,j}_{integral}$)

- For all frequencies f_n

  - For all observers $\vec{R}_j$

    * Call 'u0': compute incident field $p^{n,j}_{incident}$
    * Multiply $p^{n,j}_{incident}$ by $e^{jk_nR_j}$ (phase part).
    * Compute diffracted field through the corresponding aperture:

$$p^{n,j}_{aperture} = p^{n,j}_{integral} + \chi_j p^{n,j}_{incident}$$

    * Make use of Babinet's principle to compute field diffracted by the shielding object

$$p^{n,j}_{object} = p^{n,j}_{incident} - p^{n,j}_{aperture}$$

- Return $\{p^{n,j}_{incident}\}_{n,j}$ and $\{p^{n,j}_{object}\}_{n,j}$.

F.7.4 Subfunction: CheckShadow

F.7.4.1 Inputs

- $\mathcal{L} = \{\vec{\rho}_i\}_i$: Outline point coordinates
- $\mathcal{O} = \left\{\vec{R}_j\right\}_j$: Observer point coordinates
- *ds*: length of discretized outline segments

F.7.4.2 Outputs

- $\{\chi_j\}_j$: Values of χ at observer locations
- $\mathcal{L} = \{\vec{\rho}_i\}_i$: Couter-clockwise oriented outline

F.7.4.3 Code logic

- Discretize outline using the 'Discretize' function (subfunction of 'FindOutline'),
- Call 'Project': Project outline points $\{\vec{\rho_i}\}_i$ onto a paraboloid that lies under the source and opens upward or a plane, then store the x and y coordinates of the projection $\{x_i^{projected}\}_i, \{y_i^{projected}\}_i$.
- Project observers $\left\{\vec{R_j}\right\}_j$ the same way.
- Check if the projected observer point is inside the projected outline. This can be done by considering the 2-D projected space (stored x and y coordinates from second and third step). The first step is to shoot lines passing through the observer point that do not pass through one of the vertices of the polygon and intersect it with all sides. Then if the number of intersections is even, the point is inside the polygon, and if it is odd the point is outisde.
- Make sure the outline $\mathcal{L}$ is counter-clockwise. One can use $\{x_i^{projected}\}_i, \{y_i^{projected}\}_i$ from second step to compute the sign of the total polygon area given by

$$A = \frac{1}{2}\sum_i x_i^{projected} y_{i+1}^{projected} - x_{i+1}^{projected} y_i^{projected}$$

  . If A is positive (N: number of points), then the polygon is order counter-clockwise.
- If not counter-clockwise-oriented then inverse orientation and return a new outline $\mathcal{L} = \{\vec{\rho_i}\}_i$.

F.7.5 Subfunction: Project

F.7.5.1 Inputs

- $\{x_i\}_i, \{y_i\}_i, \{z_i\}_i$: Point coordinates

F.7.5.2 Outputs

- $\{x_i^{projected}\}_i, \{y_i^{projected}\}_i$: Projected points into a 2D projected space

F.7.5.3 Code logic

- Compute and return 2D projected point locations onto an upward paraboloid of the form $z = x^2 + y^2 - 1$ (with source at the origin):
  - Compute s_i for each set of (x_i, y_i), compute

$$s_i = x_i^2 + y_i^2$$

  - Check if s_i is not zero (irrelevant if zero)
  - Find t_i:

$$t_i = \frac{1}{2s}(z_i + \sqrt{z_i^2 + 4s})$$

  - Return projected points 2-D coordinates

$$\begin{cases} x_i^{projected} & = t_i x_i \\ y_i^{projected} & = t_i y_i \end{cases}$$

F.7.6 Subfunction: PrepareIntegral

F.7.6.1 Inputs

- $\mathcal{L} = \{\vec{\rho_i}\}_i$: Outline points (defined with source at origin)
- $\vec{R_j}$: Specified observer location (defined with source at origin)

F.7.6.2 Outputs

- $\{parameters_{i,j}\}_{i,j}$: List of parameters listed below for each outline point at specified observer location

F.7.6.3 Code Logic

- For all outline point $\vec{\rho_i}$, compute and return following parameters in $\{parameters_{i,j}\}_{i,j}$

  - N : number of outline points (without couting the first one twice)

  - L_i: length of outline segment:

$$L_i = \sqrt{(\vec{\rho_{i+1}} - \vec{\rho_i})^2}$$

  - s_i: curvilinear absissa associated with the i^{th} outline point (i starting at 1)

$$s_i = \sum_{j=1}^{i-1} L_j,$$

    with

$$s_1 = 0.$$

  - $\vec{e_i}$: unit directional vector of i^{th}outline segment:

$$\vec{e_i} = (\vec{\rho_{i+1}} - \vec{\rho_i})/L_i$$

  - $\vec{y_{0_i}}$: arbitrary starting point of the i^{th} edge, given by

$$\vec{y_{0_i}} = \vec{\rho_i} - s_i\vec{e_i}$$

  - $$\begin{cases} \vec{a_i} = \vec{y_{0_i}}, & \vec{b_i} = \vec{y_{0_i}} - \vec{R_j} \\ a_{-x,i} = \vec{a_i}.(-\hat{x}), & e_{-x,i} = \vec{e_i}.(-\hat{x}) \\ a_i^2 = \vec{a_i}.\vec{a_i}, & b_i^2 = \vec{b_i}.\vec{b_i} \\ \alpha_i = \vec{a_i}.\vec{e_i}, & \beta_i = \vec{b_i}.\vec{e_i} \\ \gamma_i = \vec{a_i}.\vec{b_i}. \end{cases}$$

$$
-\begin{cases}
\vec{u_i} = \vec{a_i} \times \vec{b_i}, & \vec{v_i} = \vec{e_i} \times (\vec{a_i} - \vec{b_i}) \\
u_i^2 = \vec{u_i}.\vec{u_i}, & v_i^2 = \vec{v_i}.\vec{v_i} \\
uv_i = \vec{u_i}.\vec{v_i}, & ue_i = \vec{u_i}.\vec{e_i} \\
\vec{w_i} = \vec{a_i} \times \vec{e_i}, & \vec{z_i} = \vec{v_i} + \vec{w_i} \\
\delta_{s,i}^2 = \vec{w_i}.\vec{w_i}, & \delta_{p,i}^2 = \vec{z_i}.\vec{z_i}.
\end{cases}
$$

F.7.7 Subfunction: Integrate

F.7.7.1 Inputs

- $\{parameters_{i,j}\}_{i,j}$: Parameters computed using the 'PrepareIntegral' function
- k_n: wavenumber
- n: corresponding component number of the wavenumber k_n in the overall vector of frequencies (1/3-Octave band).
- $R_j = \left|\vec{R_j}\right|$: distance between the source and the observer

F.7.7.2 Outputs

- $p_{integral}^{n,j}$: transmitted pressure through at specified observer location for a given source frequency f_n.

F.7.7.3 Code Logic

- For all outline linear edges ($i = 1..N$, with N: number of distinct outline points stored in $\{parameters_{i,j}\}_{i,j}$):
  - Compute

$$A_i = \frac{ue_i}{4\pi}$$

- Compute beginning and end curvilinear abscissa

$$\begin{cases} s_{a,i} = & s_i \\ s_{b,i} = & s_{i+1} \end{cases}$$

- Find stationary phase point $s_{s,i}$ by computing
  - $\delta_{s,i} = \sqrt{\delta_{s,i}^2}$
  - $\delta_{p,i} = \sqrt{\delta_{p,i}^2}$
  - $s_{s,i} = -\frac{\delta_{s,i}\beta_i + \delta_{p,i}\alpha_i}{\delta_{s,i} + \delta_{p,i}}$
- Compute the stationary phase point contribution $I_{s,i}$ by computing:
  - $\rho_{s,i} = \sqrt{a_i^2 + 2\alpha_i s_{s,i} + (s_{s,i})^2}$
  - $\cos\theta_{s,i} = \frac{a_{-x,i} + s_{s,i} e_{-x,i}}{\rho_{s,i}}$
  - $r_{s,i} = \sqrt{b_i^2 + 2\beta_i s_{s,i} + (s_{s,i})^2}$
  - $\chi_{s,i} = \sqrt{k_n |\rho_{s,i} + r_{s,i} - R_j|}$
  - $Fresnel_{s,i} = \begin{cases} \frac{1}{1 - exp(exp(-i\pi/4) 2\sqrt{\pi}\chi_{s,i})} + \frac{exp(i[\chi_{s,i}^2 + \frac{\pi}{4}])}{2\sqrt{\pi}\chi_{s,i}} & \chi_{s,i} \neq 0 \\ \frac{1}{2} & \chi_{s,i} = 0 \end{cases}$
  - $\vec{\rho_{s,i}}.\vec{r_{s,i}} = \gamma_i + (\alpha_i + \beta_i) s_{s,i} + (s_{s,i})^2$
  - $f_{s,i} = u0(k_n, \rho_{s,i}, \cos\theta_{s,i}, n) \frac{A_i}{r_{s,i}(\rho_{s,i} r_{s,i} + \vec{\rho_{s,i}}.\vec{r_{s,i}})}$
  - $g_i'' = \frac{1}{\rho_{s,i}} + \frac{1}{r_{s,i}} - \frac{(\alpha_i + s_{s,i})^2}{(\rho_{s,i})^3} - \frac{(\beta_i + s_{s,i})^2}{(r_{s,i})^3}$
  - $h_{s,i} = \sqrt{k_n \frac{g_i''}{2}}$
  - $G_{s,i} = \frac{f_{s,i}}{h_{s,i}}$
  - $I_{s,i} = 2\pi\chi_{s,i} Fresnel_{s,i} G_{s,i}$
- Compute starting point $(s_{a,i})$ contribution $I_{a,i}$:
  - $\rho_{a,i} = \sqrt{a_i^2 + 2\alpha_i s_{a,i} + (s_{a,i})^2}$
  - $\cos\theta_{a,i} = \frac{a_{-x,i} + s_{a,i} e_{-x,i}}{\rho_{a,i}}$
  - $r_{a,i} = \sqrt{b_i^2 + 2\beta_i s_{a,i} + (s_{a,i})^2}$
  - $\chi_{a,i} = \sqrt{k_n |\rho_{a,i} + r_{a,i} - \rho_{s,i} - r_{s,i}|}$

* $Fresnel_{a,i} = \begin{cases} \frac{1}{1-exp(exp(-i\pi/4)2\sqrt{\pi}\chi_{a,i})} + \frac{exp(i[\chi_{a,i}^2+\frac{\pi}{4}])}{2\sqrt{\pi}\chi_{a,i}} & \chi_{a,i} \neq 0 \\ \frac{1}{2} & \chi_{a,i} = 0 \end{cases}$
* $\vec{\rho_{a,i}}.\vec{r_{a,i}} = \gamma_i + (\alpha_i + \beta_i)s_{a,i} + (s_{a,i})^2$
* $f_{a,i} = u0(k_n, \rho_{a,i}, \cos\theta_{a,i}, n)\frac{A_i}{r_{a,i}(\rho_{a,i}r_{a,i}+\vec{\rho_{a,i}}.\vec{r_{a,i}})}$
* $g'_{a,i} = \frac{\alpha_i+s_{a,i}}{\rho_{a,i}} + \frac{\beta_i+s_{a,i}}{r_{a,i}}$
* $h_{a,i} = \frac{k_n g'_{a,i}}{2\chi_{a,i}}$
* $G_{a,i,1} = \frac{f_{a,i}}{h_{a,i}}(1 - (s_{s,i} == s_{a,i}))$ or $G_{a,i,1} = 0$ if non defined.
* $G_{a,2,i} = \frac{f_{s,i}}{h_{s,i}}(s_{s,i} == s_{a,i})$
* $G_{a,i} = G_{a,i,1} + G_{a,i,2}$
* $I_{a,i} = G_{a,i}Fresnel_{a,i}$

– Repeat previous step for ending point (replacing $s_{a,i}$ by $s_{b,i}$) to get $I_{b,i}$.

– Check if the stationary phase point lies within the segment $[s_{a,i}, s_{b,i}]$ (but does not coincidates with the bounds):

$$indicator_{s,i} = (s_{s,i} > s_{a,i}).(s_{s,i} < s_{b,i})$$

– Deduce uniform contributions of the end points and stationary phase point for the i^{th} edge

* $I_{end\,points,i} = 2\pi|\chi_{s,i}|Fresnel_{s,i}(I_{a,i} - I_{b,i})$
* $I_{s,i} = indicator_{s,i}.I_{s,i}$

- Sum the contribution of each edge to get the amplitude part of the final integral

$$integral_j = \sum_{i=1}^{N-1}(I_{end\,points,i} + I_{s,i})$$

- Multiply by phase factor to obtain transmitted pressure

$$p_{integral}^{n,j} = exp(ik_n R_j)integral_j$$